TWO–PHOTON–ABSORPTION IN SEMICONDUCTOR MICRO–CAVITIES

by

Torsten Krug

A thesis submitted for a degree of

Doctor of Philosophy
in the University of Dublin

under the supervision of

Prof. John F. Donegan

School of Physics
Trinity College Dublin
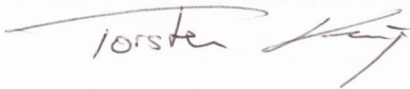
September 2005
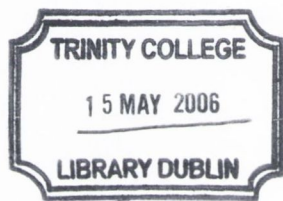
This thesis has not been submitted as an exercise for a degree at any other university. The work described herein is entirely my own, with the exception of the assistance mentioned in the acknowledgements and the collaborative work noted in the publications.

I hereby agree that the Library may lend or copy the thesis upon request.

Torsten Krug

Acknowledgement

Publications and Presentation

"Two-Photon Absorption photocurrent enhancement in a bulk AlGaAs semiconductor microcavity", T.Krug, H.Folliot, M.Lynch, A.L.Bradley, J.F.Donegan, L.P.Barry, J.S.Roberts and G.Hill, presented at Euroconference on Quantum Optoelectronics for NanoTechnology: Ultrafast Processes in Solid State Nanostructures, Les Houches, April 2002

"Two-photon absorption enhancement in AlGaAs microcavities", T.Krug, M. Lynch, A.L.Bradley, J.F.Donegan, H.Folliot, L.P.Barry, J.S.Roberts and G.Hill, presented at 26th International Conference on the Physics of Semiconductors, Edinburgh, July 2002

"Two-photon absorption enhancement in a III-V semiconductor microcavity", T.Krug, H.Folliot, M.Lynch, A.L.Bradley, J.F.Donegan, L.P.Barry, J.S.Roberts and G.Hill, presented at SPIE Opto Ireland: Optoelectronic and Photonic Devices, Galway, September 2002

"Design and fabrication of highly efficient non-linear optical devices for implementing high-speed optical processing", L.P.Barry, T.Krug, H.Folliot, M.Lynch, A.L.Bradley, P.Maguire, J.F.Donegan, J.S.Roberts and G.Hill, presented at 28th European Conference on Optical Communication (ECOC 2002), Copenhagen, Denmark, September 8-12, 2002

"*Design of micro-cavity semiconductor devices for highly efficient optical switching and sampling applications*", L.P.Barry, P.Maguire, T.Krug, H.Folliot, M.Lynch, A.L.Bradley, J.F.Donegan, J.S.Roberts and G.Hill, presented at Laser and Electro-Optics Society (LEOS 2002), 15th Annual Meeting of the IEEE, Volume 2, pages 839–840, November 10-14, 2002

"*Two-photon-induced photoconductivity enhancement in semiconductor microcavities: A theoretical investigation*", H.Folliot, M.Lynch, A.L.Bradley, L.P.Barry, T.Krug, L.A.Dunbar, J.Hegarty and J.F.Donegan, J. Opt. Soc. Am. B., Vol.19, No.10, October 2002

"*Optical autocorrelation using two-photon absorption in semiconductor microcavities*", M.Lynch, T.Krug, H.Folliot, A.L.Bradley, L.P.Barry and J.F.Donegan, presented at Semiconductor and Integrated Optoelectronics (SIOE 2003), Cardiff, Wales, April 14-16, 2003

"*A novel approach towards two-photon absorption based detectors*", T.Krug, H.Folliot, M.Lynch, A.L.Bradley, L.P.Barry, J.F.Donegan, J.S.Roberts and G.Hill, presented at Conference on Laser and Electro Optics/Quantum Electronics and Laser Science Conference (CLEO/QELS 2003), Paper CTUG5 Technical Proceedings, Baltimore, Maryland, USA, June 1-6, 2003

"*Two-photon absorption in microcavities for optical autocorrelation and sampling*", T.Krug, H.Folliot, M.Lynch, A.L.Bradley, L.P.Barry, J.F.Donegan, J.S. Roberts and G.Hill, presented at CLEO/Europe EQEC Conference, Paper CE5-4-Thu Technical Proceedings, Munich, Germany, June 23-27, 2003

"High-sensitivity two-photon absorption microcavity autocorrelator", T.Krug, M.Lynch, A.L.Bradley, J.F.Donegan, L.P.Barry, H.Folliot, J.S.Roberts and G.Hill, Photonics Technology Letters, IEEE, Volume 16, Issue 6, June 2004, pages 1543–1545

"Two-photon absorption based microcavity detector", T.Krug, M.Lynch, A.L. Bradley, J.F.Donegan, H.Folliot, L.P.Barry, J.S.Roberts and G.Hill, presented at Emerging Technologies in Optical Sciences (ETOS 2004), Cork, Ireland, July 26-29, 2004

"Simulation of a high-speed demultiplexer based on two-photon absorption in semiconductor devices", P.Maguire, L.P.Barry, T.Krug, M.Lynch, A.L.Bradley, J.F.Donegan and H.Folliot, Optics Communications 249, pages 415-420, 2005

"All-optical sampling utilising two-photon absorption in semiconductor microcavity", P.Maguire, L.P.Barry, T.Krug, M.Lynch, A.L.Bradley, J.F.Donegan and H.Folliot, Electronic Letters, Vol.41, No.8, pages 489-490, April 2005

"Resonance tuning of two-photon absorption microcavities for wavelength-selective pulse monitoring", T.Krug, W.H.Guo, J.O'Dowd, M.Lynch, A.L.Bradley, J.F.Donegan, L.Barry, P.Maguire, H.Folliot, submitted to PTL

"Effect of cavity lifetime on two-photon absorption in a planar microcavity", W.H.Guo, T.Krug, J.O'Dowd, M.Lynch, A.L.Bradley, J.F.Donegan, submitted to Optics Letters

"All-optical sampling based on two-photon absorption in a semiconductor micro-cavity for high-speed OTDM", P.Maguire, L.P.Barry, T.Krug, M.Lynch, A.L.Bradley, J.F.Donegan and H.Folliot, presented at Opto Ireland (SPIE Europe), Dublin, Ireland, April 4-6, 2005

"Two-photon absorption microcavity detector for femtosecond and picosecond pulses", T.Krug, M.Lynch, A.L.Bradley, J.F.Donegan, P.Maguire, L.P.Barry and H.Folliot, presented at Opto Ireland (SPIE Europe), Dublin, Ireland, April 4-6, 2005

"Beam propagation analysis in two-photon absorption microcavity devices", T.Krug, M.Lynch, A.L.Bradley, J.F.Donegan and H.Folliot, presented at Opto Ireland (SPIE Europe), Dublin, Ireland, April 4-6, 2005

"Highly-efficient optical sampling of a 100 Gbit/s OTDM data signal via two-photon absorption in a semiconductor microcavity", P.Maguire, L.P.Barry, T.Krug, J.O'Dowd, M.Lynch, A.L.Bradley, J.F.Donegan and H.Folliot, We3.5.4, presented at 31st European Conference on Optical Communication (ECOC), Glasgow, Scotland, September 25-29, 2005

Abstract

In this thesis a study of two-photon absorption photoconductivity in semicon-
ductor microcavities is presented. It can be shown that a 10,000-fold enhance-
ment of the non-linear two-photon absorption response can be obtained with the
microcavity structure. In this thesis the detail of the design and performance
(dynamic range, speed, bandwidth) of such devices will be discussed. Two ex-
amples are studied, an $AlGaAs/GaAs$ microcavity working at 890 nm and a
$GaAs/AlAs$ structure working at 1.55 μm. These devices can potentially be used
for low intensity, fast autocorrelation and demultiplexing applications in optical-
communication networks.

Contents

1 Introduction and Thesis Overview

This chapter opens with a discussion of recent developments in optical communications. The need for further development continues, especially in the area of all-optical signal processing and signal monitoring. Two-photon absorption microcavities have been proposed as devices suitable for performing these functions.

1.1 Integrated Optics

The dramatic improvement of transmission quality in optical fibers, coupled with equally important developments in the area of light sources and detectors, has brought about a phenomenal growth in the optical communication industry during the past two decades. It seems clear that "optical bandwidth" will always exceed "electrical bandwidth", with the latter presently falling off, for practical purposes, in the region of a few Gbit/s, while optical fiber offers a spectral bandwidth for thousands of Gbit/s. To meet the growing demand for data traffic, new technologies have to be developed. Certainly, the most well developed is Dense Wavelength Division Multiplexing (DWDM)[1]. Other technologies include Optical Time Division Multiplexing (OTDM)[2], Frequency Division Multiplexing (FDM)[3] and Code Division Multiplexing (CDM)[4]. From the beginning of the 21st century it has been possible with DWDM systems to transmit between 32 and 160 times 10 Gbit/s over very large distances [5]. This is equal to a total capacity of up to 1.6 Tbit/s. And at the laboratory research stage it is currently possible to transmit 10 Tbit/s. Even higher bandwidth can be achieved with 160 Gbit/s channel systems [6]. Currently 40 Gbit/s systems have just reached a stage where they are commercially available. Preliminary estimations predict the introduction of 160 Gb/s systems in optical networks within the next 10 years. Since the beginning of telecommunications the need to expand the capacity of the communication channels has been present. The purpose of that is to allow the use of one channel by multiple users, to allow a better management and monitoring of the resources and simply boost the transmission capacity of the channels.

As mentioned before, the solution was to use wavelength multiplexing at the optical level. The basic idea is to use different optical carriers or colours to transmit different signals along the same fiber. The bottleneck in these systems is however still the use of electrical technology for multiplexing and demultiplexing, signal amplification, transponders and regenerators. The last three applications are commonly known as the 3R regeneration of the optical signal (re-shaping, re-timing, re-amplification) [7]. In order to monitor or analyse the signals they still have to be demultiplexed, electrically regenerated and then multiplexed again. Optical switching units in DWDM links such as optical cross connects and optical add-drop multiplexers are of growing interest for transparent networks. At the moment optical traffic is connected with the help of distribution panels and large electrical cross-connects [3], but within a few years it will be necessary to switch, at least part of the exploding data traffic, using quickly reconfigurable optical cross connects. In the long term the idea is to do all this work on an optical level and create all-optical networks [8].

1.2   Semiconductor Optical Switches

One of the main advantages cited for optical signal processing is the capability of all–optical devices to switch in a time much shorter than that achieved by electronic devices [3, 9]. In order to implement these devices, however, optical materials with suitable properties are required. Much current research is aimed at developing optical materials for these applications. Ideally such materials should have (i) a large non-linearity with an ultra-short response time, and (ii) an absence of slow non-linear effects such as carrier generation and thermal effects. Although much current work centers on organic materials [10, 11], it would be very attractive to utilize semiconductor materials because of their compatibility with electronic components and their potential applicability for optoelectronic integrated circuits.

The development of innovative devices that are capable of carrying out two of

the most significant optical signal processing tasks, the monitoring of network performance and the demultiplexing of data is vital if future network design and operation are to meet the growing demands. In order to carry out these functions at the very-high data rates (>100 Gb/s per channel) anticipated in future networks, it is evident that nonlinear optical effects, which are present in optical fibres, semiconductor devices and optical crystals, can be employed, as these occur on time scales in the order of a few-femtoseconds (10^{-15} s).

1.3   Optical Sampling Oscilloscope

The standard method used to characterise and monitor optical communications systems involves the use of a fast photodetector in conjunction with a high-speed sampling oscilloscope. The opto-electronic conversion process in the photodetector places a limit on the overall bandwidth of the measurement available due to the speed limitations of current integrated electronic circuit design. At present this limits the maximum data rate of a single channel that can be accurately analysed to around 40 Gb/s [12, 13]. As the individual data rates are expected to exceed 100 Gb/s by 2010, it is imperative to develop a new optical sampling technique which can accurately characterize and monitor performance in future ultra-high speed networks [14, 15]. Such technology will become essential to both network designers and network operators for system development and testing.

1.4   Optical Demultiplexer

As the capacity of optical communication systems is constantly increased, there will come a point where it will be necessary to increase both the number of wavelength channels transmitted and the data rate carried per wavelength channel. This will involve using Optical Time Division Multiplexing (OTDM), where data is multiplexed in the time domain, to obtain very high data rates per wavelength

channel. The receiver in such a hybrid WDM/OTDM system will have to first filter the aggregate signal to isolate the single wavelength channel of interest and then perform demultiplexing of the resulting high-speed OTDM signal to acquire a number of lower data rate electronic channels. The development of a demultiplexing device, that is capable of simultaneous filtering and detection, will be vital in future photonic communications systems [16].

1.5   Optical Time Division Multiplexing

Due to the continued growth of the Internet and the introduction of new broadband services such as video-on-demand and mobile telephony, there will be a need to better exploit the enormous bandwidth that optical fibre provides in the network. The conventional method employed by many network providers is to use optical multiplexing techniques to increase the number of carriers per optical fibre. The most common variant, Wavelength Division Multiplexing (WDM), divides up the optical spectrum into a large number of non-overlapping wavelength bands and transmits each individual data-channel using a different wavelength over a single fibre. To increase capacity in WDM networks, new transmitter/receiver pairing (operating at a different wavelength) can be added, but this is expensive. An alternative is to increase the data rate transmitted per channel, but this is limited by the speed of electronics in current integrated circuits. Another option is to multiplex in the time domain instead of the wavelength domain.

Optical Time Division Multiplexing (OTDM) [17] uses short optical pulses to represent data and multiplexes in the time domain by allocating each channel specific bit slots in the overall multiplexed signal. To increase the overall capacity, shorter optical pulses can be used. However as the capacity approaches 1 Tbit/s, the duration of the optical pulses used will have to be less than 1 ps. The generation of such short temporal pulsewidths can be complicated [18], and in addition it will become increasingly difficult to compensate for the dispersion encountered as these optical pulses travel through the fibre due to their broad

7

spectral width [19].

An alternative technique, that pushes neither WDM nor OTDM to its limits, is to combine the two systems, to form a hybrid WDM/OTDM approach [20]. This approach uses OTDM to enhance the bandwidth of a number of WDM wavelength channels by putting OTDM coding on top of the data of the channels provided by WDM. This results in a smaller number of channels operating at much higher data rates, and may overcome some of the problems associated with pushing WDM and OTDM to the higher data rates.

Figure (1) shows a layout for a hybrid WDM/OTDM network. It comprises of 4 bit-interleaved OTDM multiplexed systems [21], each operating at a different wavelength ($\lambda 1$, $\lambda 2$, $\lambda 3$, $\lambda 4$). A bit-interleaved OTDM system uses a train of ultra-short optical pulses to represent the data in a single channel. To produce the OTDM signal, a single pulse train is split into N copies by a passive coupler, where N corresponds to the number of channels in the system (N = 4 in the example shown). Each pulse train is then subsequently encoded with data from an electrical source in an electro-optic modulator. The modulated pulse trains then pass through a fixed fibre delay length, which essentially assigns each data channel to a specific bit slot in the overall multiplexed signal. The multiplexer (MUX), a passive optical coupler, then combines the individual channels into a single OTDM data signal. The individual OTDM signals, each operating at an aggregate data rate of 160 Gb/s, are combined together in another passive optical coupler to form the 640 Gb/s hybrid data signal.

In order to operate at such high data rates, future photonic networks will have to carry out signal processing tasks, such as data switching and performance monitoring, in the optical domain. There is considerable interest in the development of new all-optical techniques to carry out performance monitoring (sampling) and data switching (demultiplexing) within the network [22].

In order to successfully operate at data rates in excess of 100 Gb/s per channel, networks will require a sensitive and ultrafast technique for precise optical
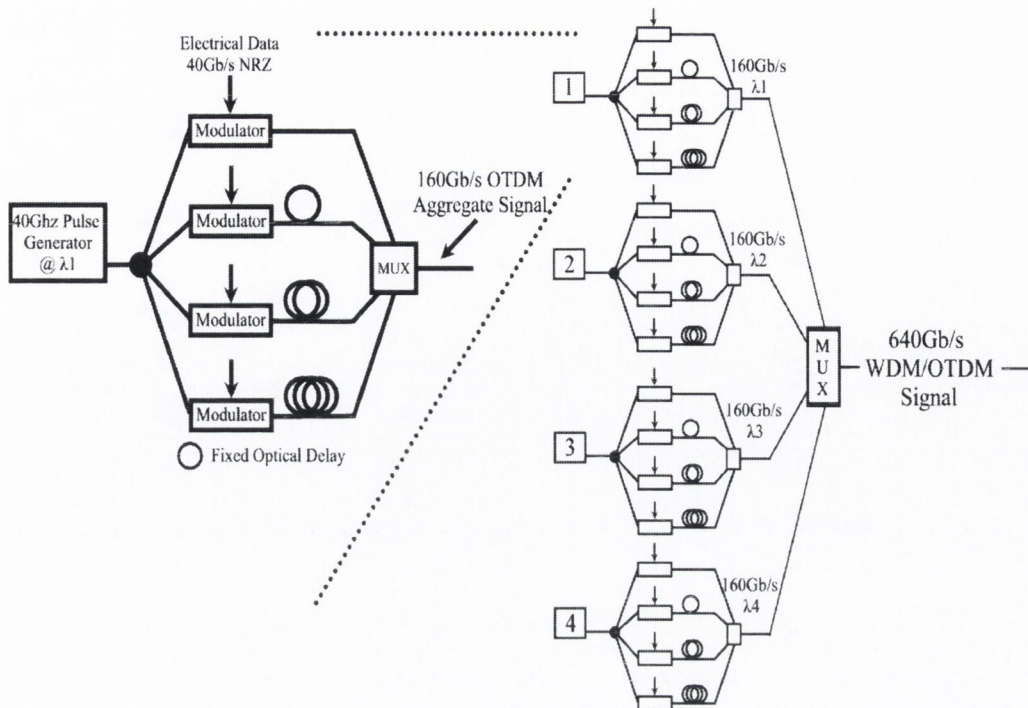
Figure 1: *Schematic of a hybrid WDM/OTDM multiplexing scheme. The inlet shows a detailed schematic of one of the 4 bit-interleaved OTDM subsystems.*

signal monitoring [23]. The standard way of characterising high-speed optical signals utilises a fast photodetector in conjunction with a high-speed sampling oscilloscope. However current electronic monitoring techniques are limited to bandwidths of approximately 80 GHz [12] due to difficulties associated with the design of high-speed electronic components [13]. These are just capable of accurately measuring data rates of 40 Gb/s. Therefore, electrical sampling schemes are unable to accurately characterise high-speed data pulses used to represent data. Critical information such as pulse duration, pulse separation and pulse rise-time, which are crucial for the optimisation of the networks performance, are distorted. As a result the use of non-linear optical effects for use in optical sampling oscilloscopes (OSO) [24] for performance monitoring of high-speed signals seems essential.

1.6 Non–Linear Optical Effects

Non-linear optical effects, as mentioned above, which are present in optical fibres, semiconductor devices and optical crystals, occur on time scales in the order of a few femto-seconds (10^{-15}s), and are therefore ideal for performance monitoring and high-speed optical demultiplexing of data. A number of industry leaders in the manufacture of optical oscilloscopes [25, 26] are investigating the use of Second Harmonic Generation (SHG), an ultrafast optical nonlinearity, for sampling at higher data rates. This involves combining a high-power optical pulse train to the data signal being analysed and generating the mixing product of both signals in the optical crystal. The energy of the mixing product pulse represents the amplitude of the data signal that can be detected by a slow photodetector. This technology is used in two commercially available OSOs from Agilent (86119A) and ANDO (AQ7750). Unfortunately there are a number of disadvantages in using the SHG process. These include:

- Very high optical intensities are required for the sampling pulse due to poor efficiency of the SHG process

- Stability problems associated with the use of free-space optics

- Need for phase matching at different wavelengths

A number of different research institutes and companies, such as Heinrich-Hertz-Institut, Germany [27], Princeton University, USA [28] and the NEC Corporation, Japan [29], are actively involved in the development of optical switches using different optical nonlinearities, such as the nonlinear change in the refractive index of fibre or semiconductors waveguides. However, as with the development of the OSO, there are a number of technical problems that are restricting progress, including the need for high optical intensities, limited wavelength range and polarisation problems. As a result it is necessary to consider utilising different nonlinearities for developing all-optical processing elements.

10

One such nonlinearity is Two-Photon Absorption (TPA) in semiconductors. TPA is a nonlinear optical-to-electrical conversion process where two photons are absorbed in the generation of a single electron-hole pair. It occurs when a photon of energy $h\nu$ is incident on the active area of a semiconductor device with a band gap $E_g \geq h\nu$ but less than $2h\nu$. Under these conditions, incident photons do not possess sufficient energy to produce an electron-hole pair. However an electron-hole pair can be produced by the instantaneous absorption of two photons, where the summation of the individual photon energies is greater than the band gap. The generated photocurrent is proportional to the square of the intensity, and it is this nonlinear response, combined with its ultra-fast response time of the order of 10^{-14} s at 1550 nm, that enables the use of TPA for high-speed optical demultiplexing and monitoring.

The main efficiency problem associated with TPA has been overcome by incorporating a Fabry-Perot micro-cavity into the design of the semiconductor device [30, 31]. Characterisation of these semiconductor devices and experimental results, which are presented in this work, have shown enhancement of over four orders of magnitude in the TPA photocurrent by using a micro-cavity structure. This allows for operation using optical intensities typically found in an optical communication network. Given the increased nonlinear efficiency of TPA (due to the micro-cavity design), and the fact that the TPA process is ultra-fast, it is highly opportune to develop optical demultiplexers and sampling oscilloscopes using this novel and innovative technology for use in future high-speed optical networks.

The sampling process utilises optical sampling pulses to monitor optical pulses from a single channel in the hybrid data signal via the TPA effect in the semiconductor. Figure (2) shows how the sampling of a hybrid system consisting of four different wavelength channels (red, green, blue, yellow) works. The hybrid signal first passes through a passive optical coupler that splits off 10% of the hybrid signal and combines it with a high-power sampling pulse train. The sampling pulse, which is at a sub-harmonic of the repetition rate of the individual

11

OTDM channels, passes through a variable optical delay, which ensures that the sampling pulses arrive at the TPA detector at a time corresponding to the bit slot of the signal to be monitored. As there are four different wavelengths in the hybrid signal, the sampling pulse is scanned across each of the four (red, green, blue, yellow) signal pulses in the bit slot of interest. The sampling delay is provided by generating the sampling pulse at a frequency slightly detuned from a sub-harmonic of the high-speed bit-rate.
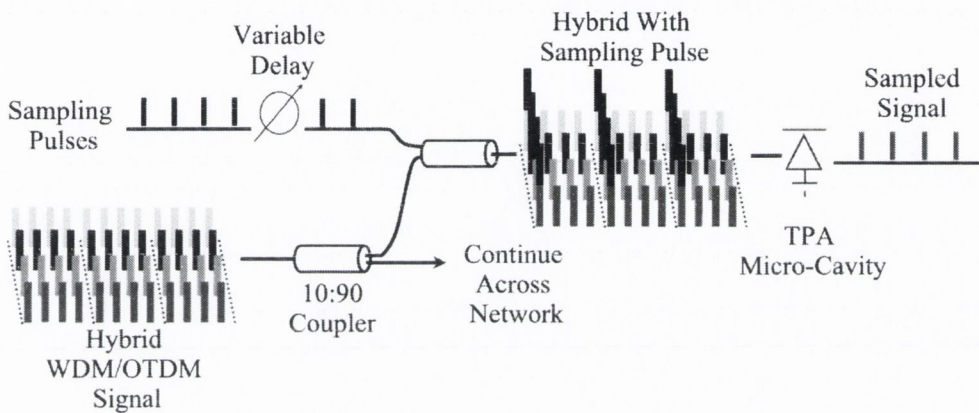
Figure 2: *Schematic of possible sampling set-up in hybrid WDM/OTDM network with TPA microcavity detector.*

The TPA microcavity then carries out simultaneous filtering and detection of the signal pulse train, with the electrical TPA signal generated by the device measured as a function of the sampling delay. This results in an intensity cross correlation between the data signal and the sampling pulse. In Figure (2), the resonance of the micro-cavity has been set to the red wavelength channel and this is the only one that experiences any enhancement as all other channels are outside the region of interest. The resulting TPA signal can then be displayed on a low-speed electrical oscilloscope. For practical implementation, the sampling pulse usually has a shorter duration and higher optical intensity when compared to the signal pulse, and the measured signal represents the signal pulse waveform

12

on a constant background. Experimental work carried out suggests that, with the current microcavity device, it is possible to successfully sample a data pulse with duration less than 2 ps at data rates in excess of 160 Gb/s and with optical peak intensity less than 8 mW [32, 33].

Optical demultiplexing using the TPA micro-cavity would be very similar to the sampling described. The major difference would be that the control pulse would be at the repetition rate of the individual OTDM channels in the multiplex and would therefore not be scanned across the signal pulse. There would be a delay dependent response from the signal and control pulses in the detector. Due to TPA nonlinear quadratic response, there would be a strong contrast between the electrical TPA signal generated when the control pulse and data pulse overlaps in the detector and when the adjacent channels arrive independently. As before, the TPA micro-cavity performs simultaneous filtering and detection of the signal. The constant background signal due to the control pulses can be conveniently subtracted electrically resulting in a high contrast demultiplexed signal.

1.7 Thesis Overview

The research described in this thesis is a continuation of the collaborative work between the School of Physics in Trinity College Dublin, the Research Institute for Networks and Communications Engineering at Dublin City University and the Laboratoire de Physique des Solides, INSA in Rennes. To build upon the original work done in our group the aim was (i) to investigate the two-photon absorption microcavity devices operating at 1.55 μm, (ii) to investigate alignment tolerance aspects of the device structure, (iii) to measure the sensitivity of the device as a detector and (iv) integrating the device into a two-photon absorption autocorrelator. Aspects of the two-photon absorption microcavity device which had previously not been investigated include its efficiency and the ability to tune the resonance wavelength when illuminated with an off-normal incident beam. The work carried out and described in subsequent chapters is summarized below.

Chapter 2 contains a discussion of the theory of Two-Photon Absorption (TPA). A basic introduction is given as well as an explanation of TPA in semiconductors. This chapter also gives an analytical expression for the calculation of the TPA photocurrent in a microcavity device.

Chapter 3 deals with an explanation of the Transfer Matrix Method (TMM), by which a complete model of the microcavity device can be achieved. Parts of the model are outlined with some simple examples of their implementation. The mechanism of absorption enhancement in a microcavity is described and an analytic expression for the enhancement factor for single and two-photon absorption is given.

Chapter 4 provides information on the device simulation. The chapter begins with an explanation of the microcavity structure. This leads to an investigation of the refractive index of the semiconductor material used in the device. Here, two different models are presented for the calculation of the refractive index. Numerical results are presented for the refractive indices and the finesse of the cavity.

Finally, different optical characterizations of microcavities are investigated, including the microcavity mode, microcavity resonance, finite reflection angle and penetration depth into the Bragg mirrors.

Chapter 5 is concerned with preliminary experimental and numerical results using a proof-of-concept device working at 890 nm. This chapter contains a description of the experimental setup used and gives a full device characterization.

Chapter 6 contains the investigations into the two-photon absorption microcavity devices working at 1.55 μm. In Section 6.2 experimental and numerical results are presented on the sensitivity of a TPA autocorrelator.

In Chapter 7 the case of off-axis operation is explained and analysed in Section 7.1 using different models. The implementation of the wavelength tunability in a TPA autocorrelator is also proposed in Section 7.1. Experimental results that support the numerical results are presented. In Section 7.2 depth-of-focus measurements using the TPA device are presented. To prove the suitability of the TPA microcavity for sonogram applications initial measurement in spectral pulse slicing have been carried out and are presented in Section 7.3.

In Chapter 8 the main results and conclusions of this thesis are summarized. Based on these results and conclusions ongoing research will be discussed and a guideline for potential future work in this area is suggested.

2 Two–Photon–Absorption

2.1 Introduction

Recently, Two–Photon–Absorption (TPA) in semiconductor devices has become an attractive, inexpensive and convenient way to perform autocorrelation measurements of picosecond and sub–picosecond laser pulses. Since the first demonstration of autocorrelation using this technique [34], many commercially available devices in different materials have been examined. This work has resulted in high sensitivity characterization of short optical pulses using TPA based autocorrelators [35 − 51]

In addition to autocorrelation, more recent work has demonstrated the possibility of using the ultra-fast TPA nonlinearity for carrying out high speed operations such as optical demultiplexing and sampling for use in ultra-high capacity optical-time-division-multiplexed (OTDM) systems [52]. This work used commercial 1.3 μm laser diodes for TPA of 1.55 μm signals [53, 54, 55], and showed that this technique is promising for developing high speed components for future Tbit/s optical systems.

However, TPA devices still require high optical input intensities in order to get a significant level of photocurrent and to exceed the dominant, residual linear absorption. One way of increasing the TPA sensitivity is of course to use longer active lengths but this is at the expense of speed which could prevent its use in OTDM systems [38]. Another approach that has been proposed [56] is to use a semiconductor microcavity where the length enhancement can be achieved artificially by the use of a Fabry-Pérot cavity.

2.2 Two-Photon Processes

The first discussion of two-quantum processes in the interaction between electro-magnetic radiation and atoms appeared in an initial report by Göppert-Mayer

16

[57] in 1929 and in a later article [58] in 1931 that summarized the results of her doctoral dissertation. In these studies, the interaction of the atom and the field were treated fully quantum mechanically using second–order perturbation theory.

The concept of two–photon processes was used soon afterwards to explain the decay rate of metastable atomic states via two-photon spontaneous emission [59]. The probability of such spontaneous two-photon transitions was found to be much smaller than those of allowed one-photon transitions by a factor of the order of $1/137 \, (1/137 \, Z)^2$ where $1/137$ is an approximation for the fine structure constant and Z is the atomic number [60]. Observation of TPA and stimulated emission processes however required the invention of the laser, which could produce intensities high enough to increase the two-photon transition probability to detectable levels.

Of all the two-photon processes, absorption has found the widest range of applications so far. Applications include precision measurement of physical constants [61], a new type of high-resolution microscopy that has revolutionized the study of living organisms in three spatial dimensions [62] and telecommunication systems applications [44]. It was first observed experimentally by Kaiser and Garrett in 1961 [63] soon after the development of the laser in 1960 [64]. In this experiment red light from a ruby laser ($\lambda = 694$ nm) was passed through an Erbium doped Calcium Fluoride ($CaF_2 : Er^{2+}$) crystal and blue fluorescent light ($\lambda = 425$ nm) was observed from the crystal. The explanation of the generation of the blue fluorescence was given as follows: the Er^{2+} ion is excited from the ground $4f$ state to the broad $5d$ excited state via two-photon absorption, which subsequently relaxes to the bottom of the $5d$ band and then decays to the ground state via one-photon spontaneous emission of a blue fluorescent photon. Supporting the assumption of TPA was the observation that the intensity of the fluorescent light scales quadratically with the intensity of the ruby laser beam. It has also been shown that the blue light could not be due to phase-matching processes of second–harmonic generation, which was reported a short time before this exper-

17

iment was carried out [65], because the Erbium doped Calcium Fluoride crystal possesses a center of inversion and therefore second–harmonic generation should be forbidden.

There have been many subsequent observations of two-photon absorption in many different materials and for a wide range of applications such as biological materials [10, 11] and laser spectroscopy [66].

2.3 TPA and Nonlinear Optics

Two-photon absorption results in a transition of electrons that arises from the addition of the energy, momentum and the angular momentum of two photons. Thus TPA is a non-linear optical-to-electrical conversion process. When the transition considered is from the valence band to the conduction band of a semiconductor, the energy sum must be $> E_g$, where E_g is the semiconductor bandgap. For degenerate TPA the two photons have the same energy $h\nu$, we thus have $2h\nu > E_g$. Here h is the Planck constant and ν is the light frequency. In this work only degenerate or quasi degenerate TPA will be considered, using just one light source, at either around 900 nm or 1.55 μm.

TPA in bulk [34], and Quantum Well (QW) [42] semiconductors have both been experimentally and theoretically extensively studied. This includes TPA coefficient measurements at different excitation energies. However since high power and large wavelength tunability are needed there is little data for the TPA coefficients available in comparison with Single Photon Absorption (SPA) in semiconductors. Moreover, theoretical predictions are more complicated, since TPA in direct bandgap semiconductors involves mixing between bands, so a large number of band or non-parabolic terms in addition to excitonic effects are needed to accurately calculate TPA coefficients [67]. Typically the experimental TPA coefficients for the considered wavelength regime are given within a factor of two accuracy. This is often due to many factors such as simplifications in calculations, using different models or difficulties in fully characterizing the pulses

18

in TPA experiments (duration, spatial fluctuations, coupling efficiency ...) [68]. Comparison between bulk and QW semiconductor structures is rather difficult [69], and the use of either will depend on the anisotropy, speed, material growth quality and TPA enhancement considerations. The TPA enhancement for a bulk microcavity structure will be discussed later (in Section (3.7)).

One method of measuring TPA in semiconductors is to measure the attenuation of the beam or pulse propagating through a two-photon absorbing medium. If the pulse irradiance is I, then the pulse is attenuated according to the expression

$$\frac{dI}{dz} = -\alpha I - \beta I^2. \tag{1}$$

Here α is the single-photon absorption coefficient and β is the two-photon absorption coefficient. If the thickness of material considered is much greater than the wavelength of the light used for the measurement, internal reflections and interference can be neglected. Neglecting the multiple reflections within the medium, the transmitted irradiance is given by the expression

$$I(r, L, t) = \frac{(1 - R)^2 \, I(r, 0, t) \, e^{-\alpha L}}{1 + \beta \, (1 - R) \, I(r, 0, t)(1 - e^{-\alpha L})/\alpha}. \tag{2}$$

Here L is the thickness and R is the reflectivity of the medium. The TPA coefficient β is related to the two-photon transition rate per unit volume $W^{(2)}$ by the expression

$$\beta = \frac{2\hbar\omega W^{(2)}}{I^2}. \tag{3}$$

Here ω is the angular frequency of the incident light. A short description of the two–photon transition rate $W^{(2)}$ will be given in Section (2.4). An alternative formulation of the TPA problem is to start with Maxwell's wave equation and treat TPA as a nonlinear source polarization. For a monochromatic beam the

electric field amplitude $\vec{E}(\vec{r}, \omega)$ is determined by the solution to Maxwell's wave equation given by

$$\nabla \times \nabla \times \vec{E}(\vec{r}, \omega) = -\frac{\vec{\epsilon}}{c^2} \frac{\partial^2 \vec{E}}{\partial t^2} - \mu_0 \frac{\partial^2 \vec{P}}{\partial t^2}. \tag{4}$$

Here $\vec{\epsilon}$ is the linear dielectric tensor, c the vacuum speed of light, $\vec{r}$ the position vector along the light propagation axis and $\vec{P}$ is the nonlinear source dipole moment per unit volume [35].

2.4 TPA in III-V Semiconductors

In semiconductors it is possible to have two-photon absorption from a single light pulse with frequency ν if twice the photon energy, $2h\nu$, exceeds the semiconductor energy gap E_g, Figure (3). The number of two-photon transitions per unit volume per unit time $W^{(2)}$ is given by second-order perturbation theory as [35]:

$$W^{(2)} = \frac{(2\pi)^3}{n^2 c^2 \hbar^2} \left(\frac{I}{\hbar}\right)^2 \sum_f |M_{fg}|^2 \delta(\omega_{fg} - 2\omega) \tag{5}$$

where

$$M_{fg} = \frac{e^2}{m^2 \omega^2} \sum_i \frac{\vec{p}_{fi} \cdot \hat{a} \ \vec{p}_{ig} \cdot \hat{a}}{\omega_{ig} - \omega} \tag{6}$$

From Equation (6) and (7) it is clear that the TPA transition rate depends on the square of the light intensity. Here n is the index of refraction of the semiconductor, c is the vacuum speed of light, m is the electron mass, e is the electron charge, $\hbar$ is the Planck's constant divided by 2π, and I is the power per unit area of the laser radiation. The summations are extended over all final states (or bands) denoted by the index f and all intermediate states denoted by the index i. The ground state is denoted by the subscript g, and the transition rate should be averaged over this index if there is more than one possible initial state. The unit vector $\hat{a}$ is directed along the electric field of the laser, and $\vec{p}_{fi}$ and $\vec{p}_{ig}$ are matrix elements of the momentum operator between the final state and the intermediate

20

state and the intermediate state and the ground state respectively. The angular frequencies ω_{fg} and ω_{ig} correspond to the angular frequency differences between the final state in the conduction band and the ground state in the valence band, respectively. These differences, in general, depend on the wave vector $\vec{k}$. If the transition rate is now expressed in terms of the peak electric field amplitude E instead of the irradiance I, the transition rate per unit volume becomes

$$W^{(2)} = \frac{2\pi}{\hbar} \left(\frac{eE}{2m\omega} \right)^4 \times \sum_f \left| \sum_i \frac{\vec{p}_{fi} \cdot \hat{a} \, \vec{p}_{ig} \cdot \hat{a}}{\hbar\omega_{ig} - \hbar\omega} \right|^2 \delta(\hbar\omega_{fg} - 2\hbar\omega). \qquad (7)$$

In addition to the perturbation theory calculation of $W^{(2)}$ that involves matrix elements between the initial and final unperturbed states, it is also possible to calculate the transition rate by a method that includes the effect of the electromagnetic field on the Bloch wave functions at the beginning of the calculation [70].

2.5 TPA in Bulk Semiconductors

For simplicity the following consideration is only done for two bands, the valence band and the conduction band as shown in Figure (3)

Valence band: p orbitals (odd symmetry) at the Brillouin zone centre

Conduction band: s orbitals (even symmetry) at the Brillouin zone centre

The transition element S_{fi} represents the number of possible transitions from the initial state i to the final state f in a semiconductor bandstructure [71]. The transition element S_{fi} can be described as

$$S_{fi} = \sum_t \frac{\langle f | \vec{e} \cdot p | t \rangle \langle t | \vec{e} \cdot p | i \rangle}{E_t - E_i - \hbar\omega} \qquad (8)$$

where p is the momentum operator (changes symmetry) and $\vec{e}$ is the light polarisation vector. The TPA absorption depends on the mixing coefficient of interband matrix elements. Thus at $k = 0$ the TPA coefficient is zero because there is no

21
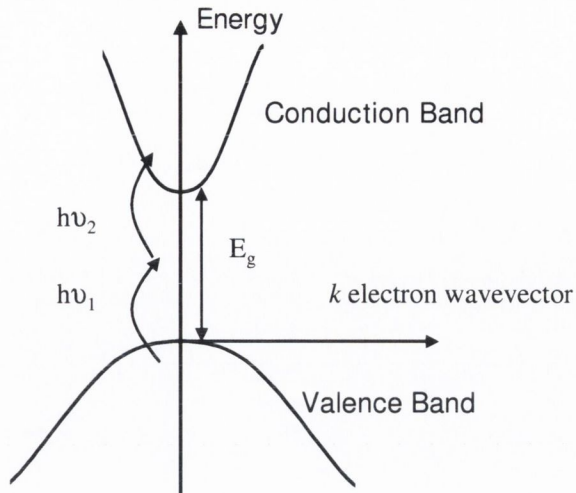
Figure 3: *TPA band structure.*

mixing between the bands. Only with increasing electron wavevector the TPA process also increases. This simple model does not take excitonic effects or non-parabolic bands into account.

The use of quantum wells (QW) in the active region of the TPA devices will give only a small enhancement of the two-photon absorption coefficient due to the symmetry selection rules and the use of TE modes only, with a beam at normal incidence in a vertical cavity [40, 41, 46, 72, 73].

2.6 Two–Photon Absorption Photocurrent

If both coefficients, α for single-photon absorption and β for two-photon absorption, are considered the differential equations for intensity propagation $I(z)$ in a semiconductor along the z-axis is

$$\frac{dI(z)}{dz} = -\alpha I(z) - \beta I(z)^2 \qquad (9)$$

Solving for $I(z)$ gives [74]

$$I(z) = I_0 \frac{e^{-\alpha z}}{1 + (\beta I_0/\alpha)(1 - e^{-\alpha z})} \qquad (10)$$

Now the single-photon absorption and two-photon absorption contributions to the total absorption can be found to be

$$I_{abs}^{SPA} = I_0 \left(1 - \frac{e^{-\alpha L}}{C}\right) \frac{\alpha L}{\alpha L + lnC} \qquad (11)$$

and

$$I_{abs}^{TPA} = I_0 \left(1 - \frac{e^{-\alpha L}}{C}\right) \frac{lnC}{\alpha L + lnC} \qquad (12)$$

with

$$C = 1 + (\beta I_0/\alpha)(1 - e^{-\alpha L}), \qquad (13)$$

where L is the length of the semiconductor along the z-axis. It is now assumed that all the photon energy is used in creating electron-hole pairs within the semiconductor, the quantum efficiency of the photoconductivity is therefore 100%. The resulting photocurrent J is then given by the following expression

$$J = \frac{eA}{h\,\nu} \left(I_{abs}^{SPA} + \frac{1}{2} I_{abs}^{TPA}\right), \qquad (14)$$

23

where A is the illuminated area on the device (semiconductor). Thus, the two-photon absorption response is limited by the single-photon absorption at low intensities and by the total absorption in the semiconductor on the high-intensity side:

$$\frac{\alpha}{\beta} \leq I \leq \frac{1}{\beta L} \tag{15}$$

Here I indicates the light intensity for the dynamic range shown in Figure (4).
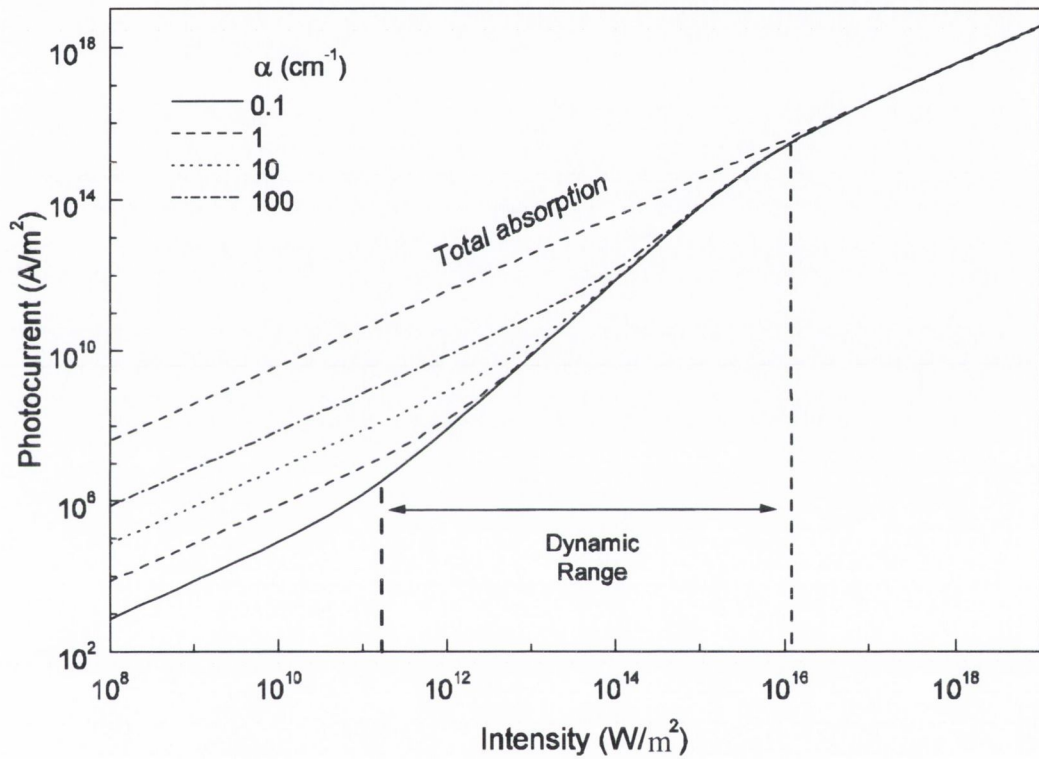
Figure 4: *Photocurrent versus intensity for a L=1 μm semiconductor, $\beta = 0.02$ cm/MW and various values of single-photon absorption α. The dynamic range is shown for the $\alpha = 0.1$ cm^{-1} curve. The linear response in the high excitation regime is due to absorption saturation, e.g. every photon pair is absorbed and the response is therefore no longer quadratic.*

3   Transfer Matrix Method

3.1   Introduction

The aim of this chapter is to provide a background to the theoretical method used to characterize the optical properties of the microcavity structure. Since a typical dielectric cavity consists of perhaps over 50 different layers, it is no longer possible to express the local electro-magnetic field in the cavity analytically as a function of the incident field. The standard technique is to use matrices to relate the electric and magnetic fields on one side of a dielectric boundary to the same quantities on the other side. The standard method of matrices can be used to calculate the reflectivity and transmission of the microcavity as well as the field intensity throughout the structure [75, 76, 77, 78, 79]. The matrices are based on a scalar plane-wave solution to Maxwell's equations that relate the incident and outgoing electric field when at an interface. This chapter will be organized along the following lines: Section (3.2) gives the electric field wave equation. Sections (3.3) and (3.4) show the implementation of the transfer matrix method. In Sections (3.5) and (3.6) the Fabry-Pérot resonator and the distributed Bragg reflector are discussed respectively. With that background Section (3.7) gives a description of the absorption enhancement obtained using a microcavity structure.

3.2   Electric Field

In this chapter a structure made of a stack of different semiconductor layers of given thicknesses and infinite lateral extension is considered. The whole structure is therefore planar and translation invariant along the plane. The axis perpendicular to the plane is labelled as the z axis. The layers are assumed to be made of homogeneous materials with uniform, frequency independent dielectric constants which can differ from layer to layer. Assuming a monochromatic electro-magnetic

25

field $\vec{E}$ at frequency ω, in the absence of charge or current density ($\rho = 0, j = 0$), the Maxwell equation for the electric field may be written as [79]

$$\nabla^2 \vec{E}(\vec{r}, z) + \frac{\omega^2}{c^2} \epsilon(z) \vec{E}(\vec{r}, z) = 0, \qquad (16)$$

where $\vec{r}$ is the position vector in the plane and $\epsilon(z)$ is the dielectric constant profile. According to the assumptions made earlier, the function $\epsilon(z)$ is piecewise constant. In addition, it is assumed to vary only within a finite z interval, which means that the thickness of our multilayer structure is finite. Because of the inplane translational invariance, the solutions of Equation (16) are plane waves along the in-plane direction. For each given in-plane wave vector $\vec{k}_{||}$ and polarisation the electro-magnetic field can be written as

$$\vec{E}_{\vec{k}_{||}}(\vec{r}, z) = \vec{\epsilon}_{\vec{k}_{||}} U_{\vec{k},\omega}(z) e^{i \vec{k}_{||} \cdot \vec{r}}, \qquad (17)$$

where $\vec{\epsilon}_{\vec{k}_{||}}$ is the polarization vector. Resubstituting into Equation (16) gives a one dimensional homogeneous second order differential equation for the mode function $U_{\vec{k}_{||},\omega}(z)$:

$$\frac{d^2 U_{\vec{k}_{||},\omega}(z)}{dz^2} + (\epsilon(z) - k_{||}^2) U_{\vec{k}_{||},\omega}(z) = 0. \qquad (18)$$

This equation may be separately solved for each homogeneous layer. For a layer with dielectric constant ϵ the mode function $U_{\vec{k}_{||},\omega}(z)$ can be expressed as

$$U_{\vec{k}_{||},\omega}(z) = E_l(\vec{k}_{||}) e^{-i k_z z} + E_r(\vec{k}_{||}) e^{i k_z z}, \qquad (19)$$

where

$$k_z = \sqrt{\frac{\omega^2}{c^2}\epsilon - k_{||}^2}. \qquad (20)$$

26

The solution (Equation (19)) represents two monochromatic waves travelling in opposite directions. The first term in Equation (19) describes a plane wave travelling in the negative z-direction, the second term describes a wave propagating in positive z-direction. It turns out from Equation (20) that propagating waves exist only for $(\omega^2/c^2)\epsilon > k_{||}^2$, otherwise the solution is an evanescent wave along $\vec{z}$. The quantities E_l and E_r are complex coefficients which can be determined by imposing Maxwells boundary conditions at each interface between two layers. The electric field and its derivative with respect to z has to be continuous at each layer interface. This task is very simple within the transfer matrix approach.

3.3 Transfer Matrices

In relation to the one dimensional consideration in Equation (18), it is possible to define for each position z in space a two dimensional vector, with components given by the two coefficients given in Equation (19), as

$$\begin{bmatrix} E_r \\ E_l \end{bmatrix} \tag{21}$$

We drop the $\vec{k}_{||}$-dependence of the E_l and E_r coefficients, since the problem is distinguished in $\vec{k}_{||}$-space. For an arbitrary structure, one can write the field in the form of Equation (19) for two points z_1 and z_2 at the two boundaries of the structure, as illustrated in Figure (5). Maxwell boundary conditions across the structure will result in a linear relationship between the coefficients in z_1 and z_2, which leads to the following notation

$$\begin{bmatrix} E_r^{(2)} \\ E_l^{(2)} \end{bmatrix} = \begin{bmatrix} M_{11} & M_{12} \\ M_{21} & M_{22} \end{bmatrix} \begin{bmatrix} E_r^{(1)} \\ E_l^{(2)} \end{bmatrix} \tag{22}$$

The matrix M is the transfer matrix of the structure under consideration. The most important property of transfer matrices is also a very intuitive one: single matrices can be composed to obtain transfer matrices of larger structures. This means that, given N structures characterised by the matrices $M_1, M_2 \ldots M_{N-1}$
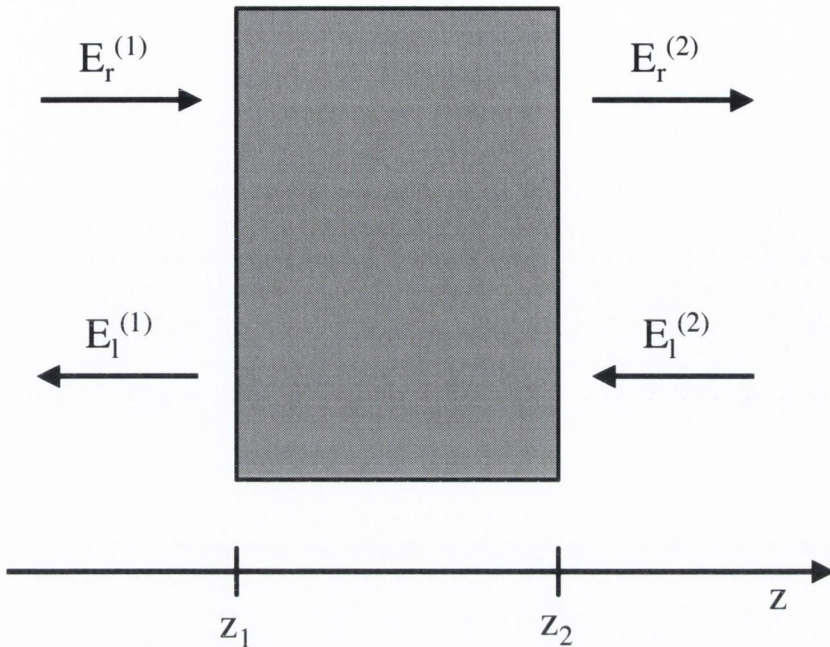
Figure 5: *Fields propagating on the two sides of a planar structure. E_r is the complex coefficient for the field of a plane wave travelling in the right direction and E_l is the complex coefficient of a plane wave travelling in the opposite direction.*

and M_N, following each other in the spatial order from left to right, the transfer matrix of the overall structure is simply $M = M_N M_{N-1} ... M_2 M_1$. It is this property that makes transfer matrices so powerful. In fact, starting with matrices for the simplest elements, namely a homogeneous layer of given thickness and a simple interface, one can simply build up the matrix for the wave propagation for arbitrarily complex planar structures.

It is straight-forward to show that the transfer matrix corresponding to the propagation from z_1 to z_2 in a homogeneous medium is given by

$$M_{hom} = \begin{bmatrix} e^{ik_z(z_2-z_1)} & 0 \\ 0 & e^{-ik_z(z_2-z_1)} \end{bmatrix}. \tag{23}$$

28

The transfer matrix for an interface at position z_0 between two dielectric layers is defined as the matrix which relates the vectors of type Equation (21) on the two sides of the interface. It is different for the two different polarisations TE (transverse electric) and TM (transverse magnetic) [79]. The transfer matrix for an interface and for TE polarisation is given by

$$M_{TE} = \begin{bmatrix} \frac{k_z^{(2)} + k_z^{(1)}}{2k_z^{(2)}} & \frac{k_z^{(2)} - k_z^{(1)}}{2k_z^{(2)}} \\ \frac{k_z^{(2)} - k_z^{(1)}}{2k_z^{(2)}} & \frac{k_z^{(2)} + k_z^{(1)}}{2k_z^{(2)}} \end{bmatrix}, \tag{24}$$

while that for TM polarization may be written

$$M_{TM} = \begin{bmatrix} \frac{n_2^2 k_z^{(1)} + n_1^2 k_z^{(2)}}{2n_1 n_2 k_z^{(2)}} & \frac{n_2^2 k_z^{(1)} - n_1^2 k_z^{(2)}}{2n_1 n_2 k_z^{(2)}} \\ \frac{n_2^2 k_z^{(1)} - n_1^2 k_z^{(2)}}{2n_1 n_2 k_z^{(2)}} & \frac{n_2^2 k_z^{(1)} + n_1^2 k_z^{(2)}}{2n_1 n_2 k_z^{(2)}} \end{bmatrix} \tag{25}$$

Here

$$k_z^{(j)} = \sqrt{\frac{\omega^2}{c^2} \epsilon_j - k_{||}^2}, \tag{26}$$

where $j = 1,2$ indicate the left and right side material respectively, and $n_j = \sqrt{\epsilon_j}$.

3.4 Time and Space Inversion

Due to the nature of Maxwell's equations the Maxwell boundary conditions must be invariant under time reversal. This means that the complex coefficients of the transfer matrix do not change if the time evolution is reversed, always providing the use of the convention that the first component of the 2-D vector is the right-propagating wave (in positive z-direction). It is easy to verify that the time reversal operator $\hat{T}$ acts as

$$\hat{T}_z \begin{bmatrix} E_r \\ E_l \end{bmatrix} = \begin{bmatrix} E_l^* \\ E_r^* \end{bmatrix}. \tag{27}$$

29

The time reversal invariance allows the four elements of a general transfer matrix to the complex reflection and transmission coefficients of the corresponding structure to be related. Consider the situation in which a wave with amplitude 1 is coming from the left, a wave of amplitude r is reflected in the opposite direction and a wave of amplitude t is transmitted through the right boundary of the structure in direction of original wave propagation (Figure(6)).
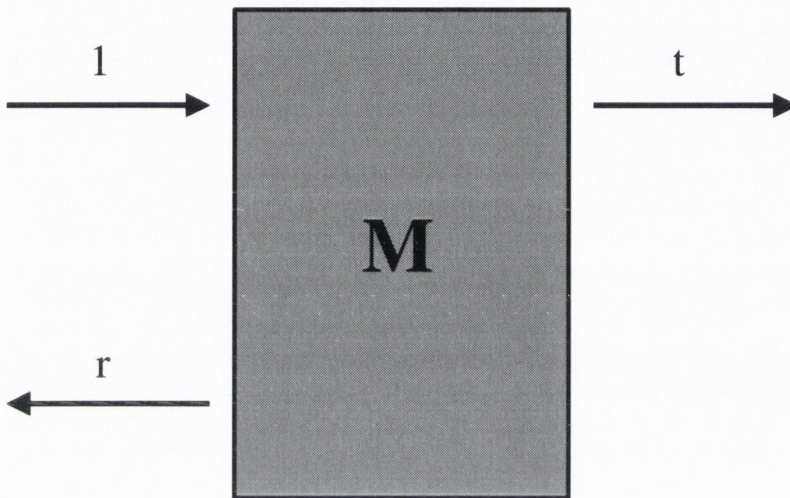
Figure 6: *Reflectance and transmission. The amplitude of the incident plane wave on the structure M is 1. The structure M is not absorbing and therefore $r + t = 1$.*

The structure M is not absorbing. Then

$$\begin{bmatrix} t \\ 0 \end{bmatrix} = \begin{bmatrix} M_{11} & M_{12} \\ M_{21} & M_{22} \end{bmatrix} \begin{bmatrix} 1 \\ r \end{bmatrix} \tag{28}$$

which gives

$$r = -\frac{M_{21}}{M_{22}} \quad , \quad t = \frac{det(M)}{M_{22}}. \tag{29}$$

Another step is needed which consists in finding the determinant of the transfer matrix. To do this, the reflectance $R = |r|^2$ and the transmittance $T = |t|^2/\alpha_{12}$ are defined, where

$$\alpha_{12} = \frac{Re(k_{1z})}{Re(k_{2z})} \tag{30}$$

for TE polarization and

$$\alpha_{12} = \frac{Re(k_{1z})}{Re(k_{2z})} \frac{n_2^2}{n_1^2} \tag{31}$$

for TM polarization. Here, n_1, n_2 are the refractive indices of the left and right side materials respectively. Then, by using the relation $R + T = 1$ together with Equation (29), very simple algebra gives the following result

$$det(M) = \alpha_{12}. \tag{32}$$

Another important symmetry operation is the space inversion along the z direction. Of course, in general a planar multi-layered structure is not invariant under such symmetry operation. However, the space inversion operator is going to be used when describing the Fabry-Pérot resonator. By applying the inversion of the z coordinate on the electric field the obvious result can be obtained that the left and right travelling waves are simply exchanged,

$$\hat{P}_z \begin{bmatrix} E_r \\ E_l \end{bmatrix} = \begin{bmatrix} E_l \\ E_r \end{bmatrix}. \tag{33}$$

31

3.5 The Fabry-Pérot Resonator

This section will describe the properties of a simple light confining device: the Fabry-Pérot resonator. The Fabry-Pérot resonator to be considered is a planar structure consisting of two parallel mirrors. The mirrors can be of any kind of material, so in the following analysis the general case will be considered with two mirrors described by their reflection and transmission coefficients, r and t. The detailed multiple pass interference description of the Fabry-Pérot resonator can be found in many textbooks [79, 80, 81]. The Fabry-Pérot resonator is illustrated in Figure (7).
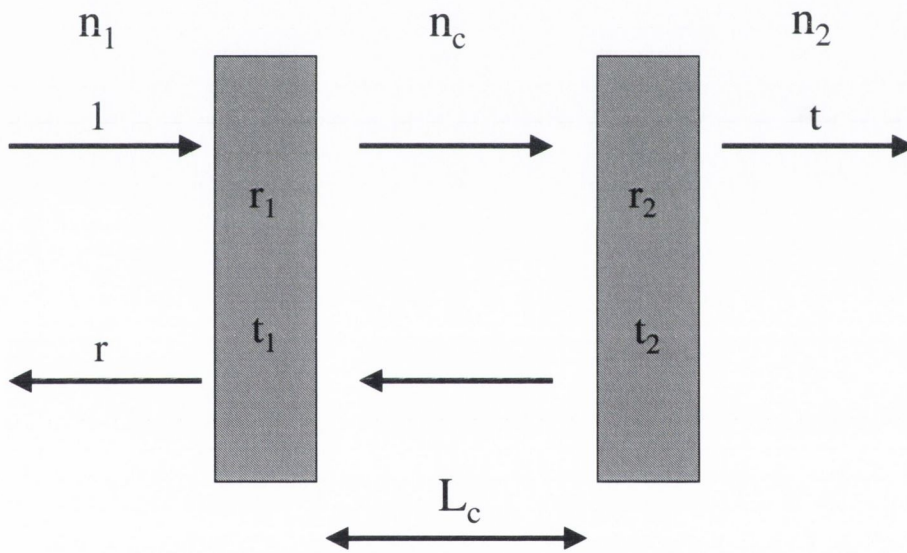
Figure 7: *Schematic of a Fabry-Pérot resonator. L_c is the width of the spacer between the two parallel mirrors. n_1 and n_2 are the refractive indices outside the Fabry-Pérot resonator.*

The central part between the two mirrors has a refractive index n_c and is called the spacer or active region. For the moment, there is no assumption being made

about the thickness L_c of the active region. The refractive indices for the left and right materials are n_1 and n_2 respectively. As illustrated in Figure (7), a plane wave of unit amplitude will be considered incoming from the left of the structure and consequently defining the reflection and transmission coefficients r and t of the whole structure. In the most general case, the two mirrors are different and their reflection and transmission coefficients are denoted by r_1, t_1 and r_2, t_2 respectively. It is important to mention that these coefficients are defined, for each mirror, for light incoming from the spacer region. $t_{1,2}^*$ and $r_{1,2}^*$ are the reflection and transmission coefficients defined for a left propagating wave.

Now the transfer matrix of the whole structure will be determined. This is simply obtained by applying the algebra defined in the previous section. In particular, three transfer matrices have to be created corresponding to the left mirror, the spacer and the right mirror, called M_1, M_S and M_2 respectively. They are given by

$$M_1 = \alpha_{1c}^2 \begin{bmatrix} \frac{1}{t_1^*} & \frac{r_1}{t_1} \\ \frac{r_1^*}{t_1^*} & \frac{1}{t_1} \end{bmatrix}, \tag{34}$$

$$M_S = \begin{bmatrix} e^{ik_z L_c} & 0 \\ 0 & e^{-ik_z L_c} \end{bmatrix}, \tag{35}$$

$$M_2 = \frac{1}{\alpha_{2c}^2} \begin{bmatrix} \frac{1}{t_2^*} & -\frac{r_2^*}{t_2^*} \\ -\frac{r_2}{t_2} & \frac{1}{t_2} \end{bmatrix}. \tag{36}$$

A few important remarks follow. The Matrix M_2 is defined by applying the time reversal invariance, $\hat{T}_z$ (Equation (27)), because r_2 and t_2 are defined for light coming from the left in our convention. On the other hand, matrix M_1 derives from the space inversion invariance $\hat{P}_z$, since r_1 and t_1 are defined for light coming from the right of the mirror.

The transfer matrix for the Fabry-Pèrot structure is $M_{FP} = M_2 \cdot M_S \cdot M_1$

$$M_{FP} = \frac{\alpha_{1c}^2}{\alpha_{2c}^2} \left[\begin{array}{cc} \dfrac{e^{ik_z L_c} - r_1^* r_2^* e^{-ik_z L_c}}{t_1^* t_2^*} & \dfrac{r_1 e^{ik_z L_c} - r_2^* e^{-ik_z L_c}}{t_1 t_2^*} \\ \dfrac{r_1^* e^{-ik_z L_c} - r_2 e^{ik_z L_c}}{t_1^* t_2} & \dfrac{e^{-ik_z L_c} - r_1 r_2 e^{ik_z L_c}}{t_1 t_2} \end{array} \right]. \tag{37}$$

The two diagonal elements in M_{FP} are conjugate to each other, the two off-diagonal elements are also conjugate to each other.

Using Equation (29) it is straightforward to state the transmission and reflection coefficient of the Fabry-Pérot resonator, which are given by

$$t_{FP} = \frac{1}{[M_{FP}]_{22}}, \tag{38}$$

$$r_{FP} = t_{FP} [M_{FP}]_{12} \tag{39}$$

These expressions are the most general ones for a Fabry-Pèrot resonator, once the properties of the mirrors are known. In general, the reflection and transmission coefficients of the two mirrors are complex quantities that depend on the in–plane wavevectors and the frequency of the light. One particular case is going to be considered in the following section, the distributed Bragg reflector.

3.6 Distributed Bragg Reflector

So far in this chapter the properties of a simplified Fabry-Pèrot structure with mirrors of equal reflectance and transmission, having frequency independent reflection coefficients, have been described. Semiconductor microcavities are essentially Fabry-Pèrot resonators with a more complex mirror structure. The mirrors, called Distributed Bragg Reflectors (DBRs) [82, 83], are stacks of semiconductor layers with two alternating refraction indices, as shown in Figure (8).
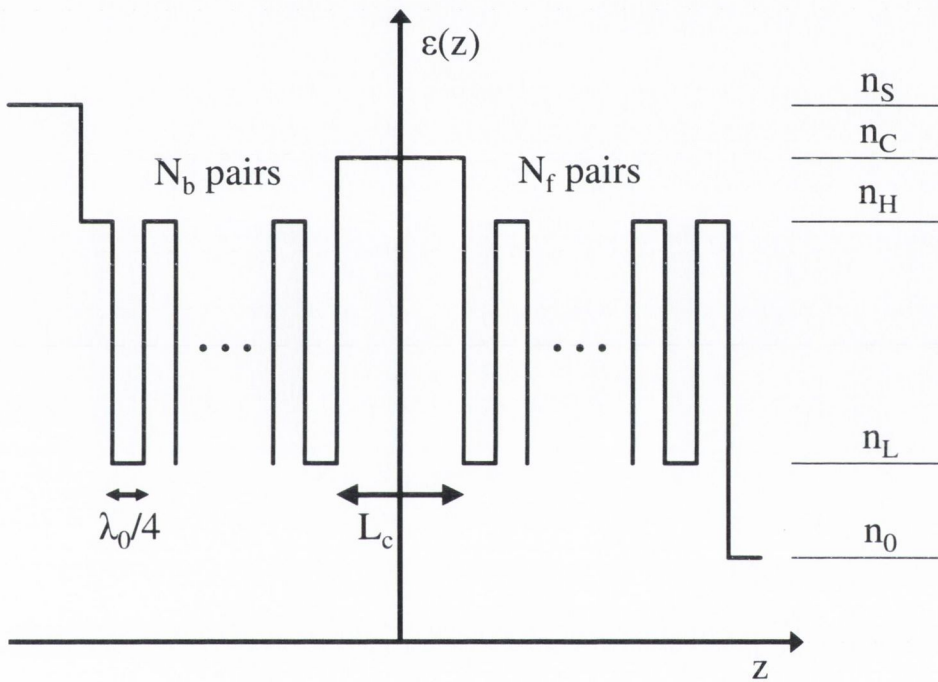
Figure 8: *Dielectric profile of a typical semiconductor microcavity. N_f and N_b are the number of front and back DBR pairs, respectively. The corresponding labels of refractive indices for the different layers are given on the right side of the figure.*

The two indices, that should be denoted n_H and n_L with $n_H > n_L$, and the thickness of the two layers L_H and L_L are chosen in order for the two layers to have the same optical thickness $L_H/n_H = L_L/n_L = \lambda_0/4$. A DBR designed

in such a way presents a wavelength region centered at λ_0 in which the square of the reflection coefficient at normal incidence is very close to one, provided the number of pairs is sufficiently high. In addition, the phase of the reflection coefficient within this region, called the stop band, behaves linearly as a function of the frequency. The real part and the phase of the reflection coefficient of a typical DBR are plotted in Figure (9) for light at normal incidence. The DBR thus behaves as a very good mirror, within a given frequency window. This property is preserved also for different incident angles (for more details see Chapter (2.7)). The phase information was extracted from the TMM using a simple $MATLAB$ sub-program.
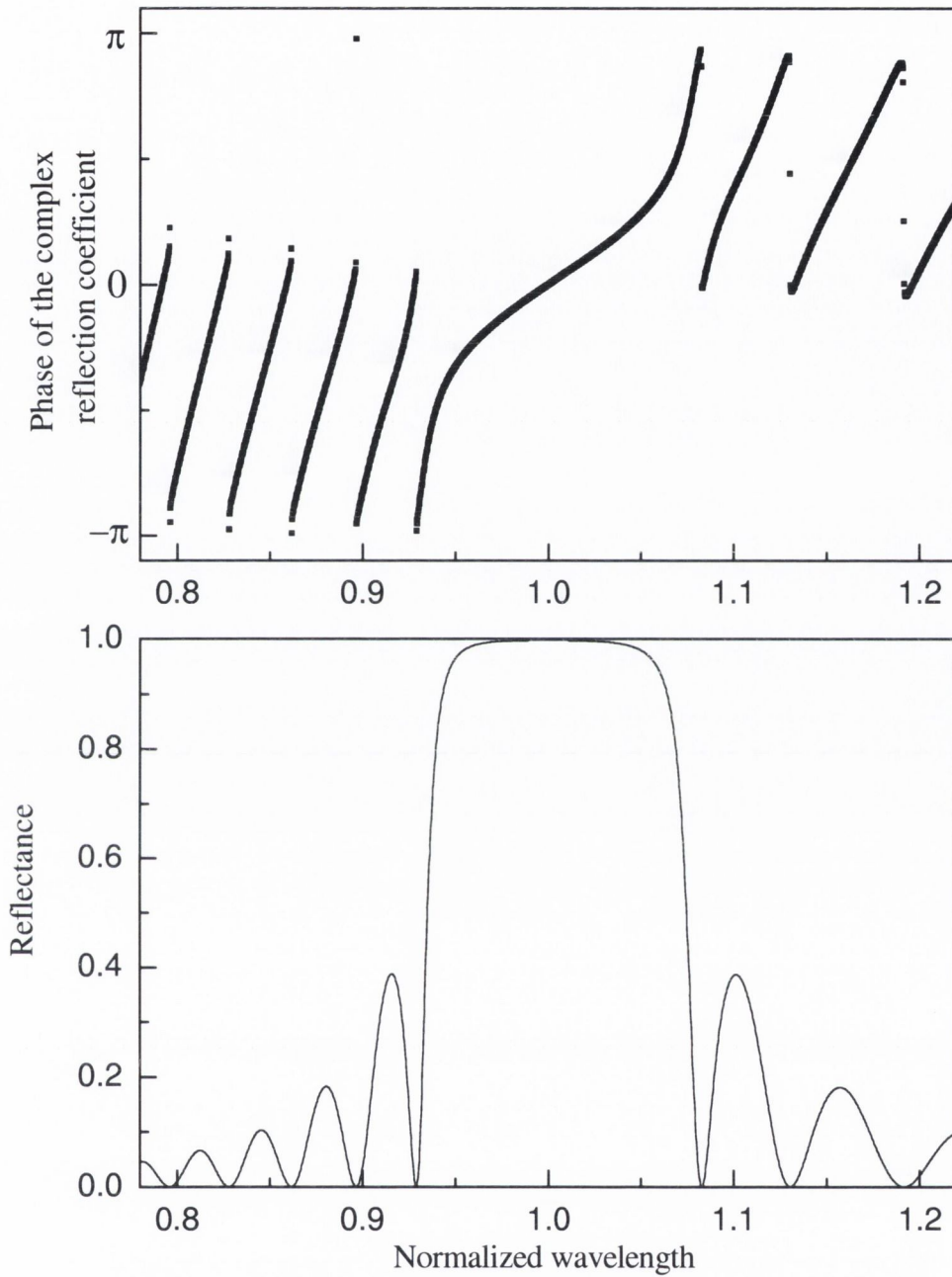
Figure 9: *Phase of the complex reflection coefficient (upper graph) and reflectance (lower graph) of a 35-pair DBR with refractive indices of $n_H=3.6$ and $n_L=3.0$. Stray data points in the upper graph are caused by the limited numerical resolution of the model used.*

The reflection coefficient of a DBR can be calculated using the transfer matrix formalism. Here a useful parametrization of the reflection coefficient $r(\omega)$ at normal incidence will be given (without derivation), which is valid inside the stop band and for a sufficiently high number of pairs of layers. The refractive indices on the left and right side of the mirror are indicated as n_l and n_r, respectively, n_l and n_r can therefore be the refractive indices for either the substrate, the incident medium or the active layer (for a given structure n_l and n_r would correspond to n_S, n_C and n_0). It is assumed that the first layer on the left side of the mirror has the low refractive index n_L and that the index of the left material n_l is larger than n_L. Moreover, it will be assumed that the DBR has an even number of layers $2N$. The reflectance $R = |r(\omega)|^2$ is then approximately constant and given by the value at the center of the stop band $\omega = \omega_m$. The approximate result, obtained by neglecting the quantity $(n_L/n_H)^{2N}$ compared to $(n_H/n_L)^{2N}$, since the first expression is much smaller than the latter by definition, is

$$R = 1 - 4 \frac{n_r}{n_l} \left(\frac{n_L}{n_H} \right)^{2N}, \quad (n_H > n_L). \tag{40}$$

The phase of the complex reflection coefficient has an approximately linear frequency dependence inside the stop band as seen in Figure (9). Within the same approximation introduced for the previous expression, the phase is given by

$$\phi_r(\omega) = \frac{n_l L_{DBR}}{c} (\omega - \omega_m), \tag{41}$$

where L_{DBR} represents an effective thickness given by

$$L_{DBR} = \frac{\lambda}{2} \frac{n_H n_L}{n_l (n_H - n_L)} \quad (n_H > n_L). \tag{42}$$

Here, λ is the chosen optical thickness (the mirror layers have the optical thickness $\lambda/4$). It has to be noted that L_{DBR} does not depend on the number of pairs. The above expressions are only valid for sufficiently large number of pairs (greater than 3 [75]). In the situation where the number of DBR pairs is sufficiently

38

large, L_{DBR} is not considered a real penetration depth for the electromagnetic field but rather an effective optical length that expresses the phase change of the electromagnetic wave at the reflection point. It will be described later how this parameter influences the properties of a Fabry-Pérot resonator. The analytical approximations given by Equation (40), (41) and (42), together with the other considerations that have been made in relation to the DBR structures, can be derived in a straight-forward way from the transfer matrix formalism. Here we will not give such derivations, since we are interested only in the practical aspects related to microcavities, and reference [79] should be consulted for more information. In what follows it will be assumed that the DBR reflectivity can be parametrized using the three expressions above.

A Fabry-Pèrot resonator can be built using two DBRs. The expressions already introduced for the reflection and transmission coefficient, Equation (38) and (39) are still valid, as well as those for the reflectance and transmittance, which are

$$T_{FP} = \frac{|t_{FP}|^2}{\alpha_{12}}, \qquad (43)$$

$$R_{FP} = |r_{FP}|^2. \qquad (44)$$

At this point some comment on the role of the cavity thickness L_C must be made. It will also be pointed out what the difference between a *microcavity* and a macroscopic *Fabry-Pérot* resonator is. When the thickness of the spacer L_C is large with respect to the wavelength λ, the mirror frequency ω_m will approach some frequency ω_N with a sufficient number of DBR pairs, e.g. N large. Since the spacing between successive ω_N values is large with respect to ω_m, several cavity modes will appear, closely spaced, within the mirror stop band. A microcavity on the other hand, is a Fabry-Pérot resonator whose active region has a thickness equal to a small multiple of $\lambda/2$. In such a system, typically only one cavity resonance occurs within the stop band, corresponding to one of the lowest reso-

nances of the spacer. The resulting electromagnetic mode in this case is a narrow isolated peak, as will be shown later.

For the following part of the chapter the interest is focused on the microcavity system. The terms λ-cavity or $\lambda/2$-cavity will be used to denote a microcavity with $L_C = \lambda$ or $L_C = \lambda/2$ respectively, while ω_C will denote the frequency resonance that falls inside the stop band region of the mirrors. The phase of the reflection coefficient of the DBRs at the stop band is zero, as appears from Equation (41). This means that the E-field of the Fabry-Pérot mode will be a plane wave with antinodes at the mirror boundaries. Usually microcavities are designed in order to maximize the amplitude of the field somewhere inside the spacer. The $\lambda/2$-cavity is not suitable in the present case since it presents a node at the center of the spacer. $\lambda/2$-cavities can be built if the other prescription for the mirror design (low spacer index and high index for the first mirror layer)is chosen, since in that case the phase of the reflection coefficient at the mirror boundary is π at resonance [82]. Figure (10) shows the refractive index structure of a λ-cavity and the calculated electric field inside the cavity.
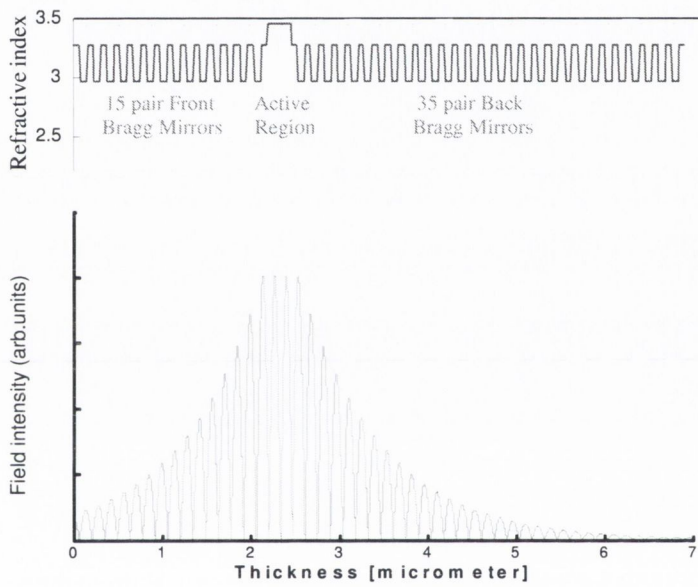
Figure 10: *Refractive index structure and electric field distribution of a 15×35 DBR λ cavity.*

Substituting Equation (40), (41) and (42) into the transmission expression for a Fabry-Pérot resonator and by developing the sine function in the transmission expression (Taylor expansion) around the cavity resonance, a Lorentzian lineshape expression for T_{FP} can be obtained and the corresponding cavity mode linewidth:

$$2\gamma_C = \frac{1-R}{\sqrt{R}} \frac{c}{n_C(L_C + L_{DBR})}. \tag{45}$$

For metallic mirrors, the mode linewidth is generally narrower than for Fabry-Pérot cavities of equal reflectance. This effect is a direct consequence of the frequency dependence of the phase $r(\omega)$. The phase change on a round trip varies more rapidly as a function of frequency compared to a Fabry-Pérot with metallic mirrors of equal reflectance; therefore the resonance condition is satisfied within a narrower frequency window. For normal incidence the condition for constructive interference for a cavity round trip reads:

$$\frac{n_C}{c}[(\omega - \omega_C)L_C + (\omega - \omega_m)L_{DBR}] = N\pi, \tag{46}$$

where N is an integer. In the special case where the mirrors are designed with a resonant frequency ω_m equal to the spacer resonance ω_C, Equation (46) becomes

$$\frac{n_C}{c}(\omega - \omega_C)(L_C + L_{DBR}) = N\pi. \tag{47}$$

In DBRs made of III-V semiconductors, L_{DBR} is about one order of magnitude larger than the microcavity thickness L_C. In this case, and for small mirror-cavity detuning ($\frac{\omega_C}{\omega_m} \approx 1$), the Fabry-Pérot resonance frequency is practically determined by the mirror resonance. This is a very important property that has to be considered when designing a semiconductor microcavity. From now on, a cavity design such that $\omega_C = \omega_m$ at normal incidence will be assumed. From a practical point of view, this choice minimizes the cavity mode linewidth because the cavity mode frequency falls at the center of the stop band region where the mirror reflectance, and consequently the light confinement, is maximum.

3.7 Absorption Enhancement

The following analysis is valid for a plane wave incident on a Fabry-Pérot cavity [84]. The frequency of the electric field is $\omega = kc$, k_z is the wavenumber in z–direction, defined as $k_z = n\omega/c$ with n being the refractive index inside the Fabry-Pérot cavity. The refractive index n is a real number assuming no optical losses in the cavity. Also, ϕ_{r_i} and ϕ_{t_i} are the phase shifts at the front and back mirror respectively. First, no absorption in the cavity is assumed and the corresponding electric field is calculated. The electric field obtained under this assumption will be used to calculate the intensity inside the cavity. Using this calculated electric field the Single–Photon Absorption (SPA) and Two–Photon Absorption (TPA) will finally be calculated. Figure (11) shows a Fabry-Pérot structure with reflection and transmission coefficients for the front and back mirror indicated.

No loss in the mirrors has been assumed. E_{in} is the electric field at normal incidence from the left of the structure. The following relations are given:

$$R_i + T_i = 1 \; , \quad i = 0, 1, 2, \tag{48}$$

$$R_0 = R_1, \tag{49}$$

$$T_0 = T_1 \; , \quad \phi_{t_0} = \phi_{t_1}, \tag{50}$$

$$2\phi_{t_0} + \pi = \phi_{r_0} + \phi_{r_1}. \tag{51}$$

Now the reflected field E_r can be expressed in terms of reflection and transmission coefficients of the Fabry-Pérot structure. The ratio between E_r and E_{in} is given by the following expression:
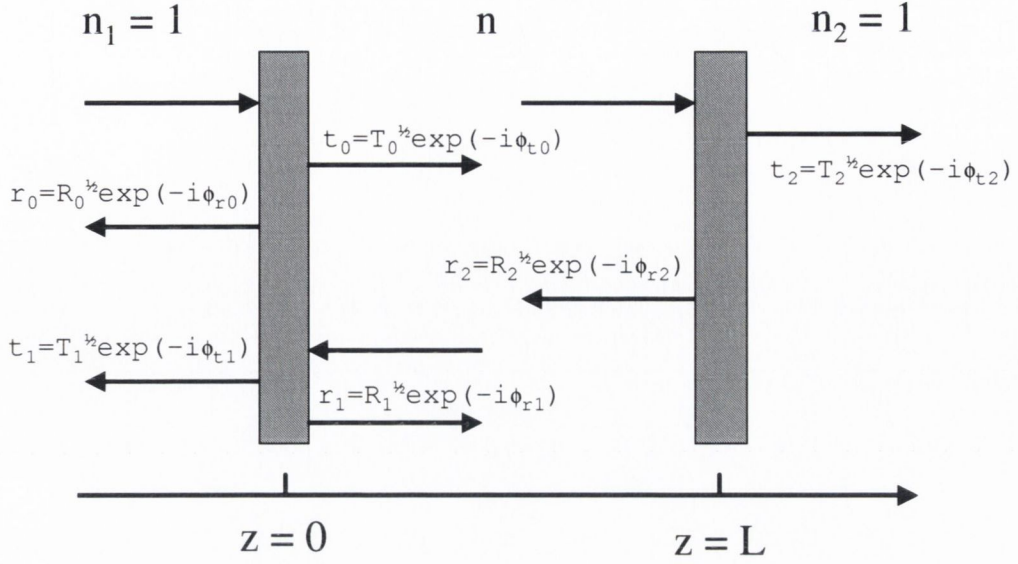
Figure 11: *Schematic of a Fabry-Pérot cavity including relevant reflection and transmission coefficients for all interfaces. The refractive indices for the left and right side of the Fabry-Pérot resonator are chosen to be 1. The refractive index of the spacer layer is n.*

$$\frac{E_r}{E_{in}} = \sqrt{R_0}\, e^{(-i\phi_{r_0})} + \frac{\sqrt{T_0 T_1 R_2}\, exp[-i(\phi_{t_0} + \phi_{t_1} + \phi_{r_2} + 2k_z L)]}{1 - \sqrt{R_1 R_2}\, exp[-i(\phi_{r_1} + \phi_{r_2} + 2k_z L)]}, \quad (52)$$

The reflection and transmission coefficients used for this expression are all indicated in Figure (11). $k_z = n\omega/c$ for normal incidence and n is the refractive index inside the cavity. For the case of no absorption the refractive index n is real. The transmitted electric field E_t in terms of the incident field is then given by:

$$\frac{E_t}{E_{in}} = \frac{\sqrt{T_0 T_2}\, exp[-i(\phi_{t_0} + \phi_{t_2} + k_z L)]}{1 - \sqrt{R_1 R_2}\, exp[-i(\phi_{r_1} + \phi_{r_2} + 2k_z L)]}. \quad (53)$$

After defining the reflected and transmitted fields the electric field inside the cavity is now considered. The electric field inside the Fabry-Pérot cavity can be

44

expressed as

$$\frac{E_c}{E_{in}} = \sqrt{T_0}\, e^{(-i\phi_{t_0})} \frac{exp(-ik_z z) + \sqrt{R_2}\, exp[-i(2k_z L + \phi_{r_2})]exp(ik_z z)}{1 - \sqrt{R_1 R_2}\, exp[-i(\phi_{r_1} + \phi_{r_2} + 2k_z L)]}. \tag{54}$$

Assuming that the refractive indices of the incident medium and exit medium are 1, Equation (44) and (45) can be used to calculate the reflectance and transmittance of the cavity. If the mirrors are lossless it can be shown that the sum of R_{FP} and T_{FP} is equal to 1 (Equation (48)). The transmittance is given by

$$T_{FP} = \frac{T_0 T_2}{\left| 1 - \sqrt{R_1 R_2}\, e^{-i\psi} \right|^2} \equiv T_0 T_2 \Gamma, \tag{55}$$

where $\psi = \phi_{r_1} + \phi_{r_2} + 2k_z L$ is the periodic phase shift in the cavity. The mode wavelength of the cavity is determined by $\psi = 2m\pi$. The factor Γ is defined as follows to simplify the following equations:

$$\Gamma = \frac{1}{1 + R_1 R_2 - 2\sqrt{R_1 R_2}\, cos(\psi)} \tag{56}$$

Slight deviations in ψ due to wavelength changes or changes in the physical thickness of the cavity due to temperature, stress or carrier concentration changes lead to the following approximation for the cavity transmittance

$$T_{FP} \approx \frac{T_0 T_2}{(1 - \sqrt{R_1 R_2})^2 + \sqrt{R_1 R_2}\Delta\psi^2}, \tag{57}$$

which has a Lorentzian lineshape with the full-width half maximum (FWHM) of

$$\Delta\psi_{FWHM} = \frac{2(1 - R)}{\sqrt{R}} \tag{58}$$

where $R = (R_1 R_2)^{1/2}$.

If the total phase shift is only caused by the wavelength deviation $\Delta\lambda$ from the resonance wavelength λ_0, $\Delta\psi$ can be described as

45

$$\Delta\psi \approx \Delta\lambda \frac{\delta\psi}{\delta\lambda}\bigg|_{\lambda_0} = -\Delta\lambda \frac{4\pi}{\lambda_0^2}(n L + L_{r_1} + L_{r_2}), \tag{59}$$

where

$$L_{r_i} = -\frac{\lambda_0^2}{4\pi} \frac{\delta\phi_{r_i}}{\delta\lambda}\bigg|_{\lambda_0}, \tag{60}$$

and $\psi = \phi_{r_1} + \phi_{r_2} + 2k_z L$ at normal incidence. The optical length of the cavity is now defined for the case $D \equiv n L + L_{r_1} + L_{r_2}$, so that the FWHM of the transmission spectrum as a function of wavelength is given by

$$\Delta\lambda_{FWHM} = \frac{(1-R)}{\sqrt{R}} \frac{\lambda_0^2}{2\pi D}. \tag{61}$$

If the mirror losses can be neglected, $R_{FP} \approx 1 - T_{FP}$, the reflection spectrum has the same FWHM as the transmission spectrum. For a Fabry-Pérot cavity with optical length D, the free spectral range (FSR) of the cavity is $\lambda_0^2/2D$. The Finesse of the cavity can then be calculated according to Equation (84) or (69). The intensity inside the cavity is

$$\frac{I_c}{I_{in}} = \left|\frac{E_c}{E_{in}}\right|^2 = T_0\Gamma[1 + R_2 + 2\sqrt{R_2}\cos(2k_z z - 2k_z L - \phi_{r_2})]. \tag{62}$$

For small variations in wavelength, e.g. $\Delta\lambda \approx 4$ nm, the bracket term in Equation (62) is assumed to be constant. Therefore the intensity inside the cavity has the same wavelength variance as the transmission and reflection spectra. As shown in Chapter (1), Equation (1), TPA depends on the intensity square. Using Equation (62) and integrating over the cavity length L leads to

$$\begin{aligned} \varsigma_{TPA} = \ & T_0^2\Gamma^2\bigg[1 + R_2^2 + 4R_2 + \frac{2\,(1+R_2)\sqrt{R_2}\,[sin(2k_z L + \phi_{r_2}) - sin(\phi_{r_2})]}{k_z L} \\ & + \frac{R_2\,[sin(4k_z L + 2\phi_{r_2}) - sin(2\phi_{r_2})]}{2k_z L}\bigg] \end{aligned} \tag{63}$$

46

which is the enhancement factor of TPA relative to the non-cavity case. Single–photon absorption (SPA) will also be enhanced inside a Fabry-Pérot structure.

$$\varsigma_{SPA} = T_0 \Gamma \left[1 + R_2 + \frac{\sqrt{R_2} \left[sin(2k_z L + \phi_{r_2}) - sin(\phi_{r_2}) \right]}{k_z L} \right] \tag{64}$$

As shown earlier a quarter-wavelength Bragg mirror structure has been used and a cavity length which is a multiple of half the resonance wavelength. Those conditions, $2k_z L = 2m\pi$ and $\phi_{r_2} = 0$ or π, allow us to simplify the enhancement factors for SPA and TPA.

$$\varsigma_{TPA} = \frac{T_0^2 (1 + R_2^2 + 4R_2)}{(1 - \sqrt{R_1 R_2})^4}, \tag{65}$$

$$\varsigma_{SPA} = \frac{T_0 (1 + R_2)}{(1 - \sqrt{R_1 R_2})^2}. \tag{66}$$

The final results for the SPA and TPA enhancement factors given here are only valid for the case without absorption and losses in the mirrors for a plane wave model.

For autocorrelation measurements using the microcavity device the TPA is required to be larger than the SPA, which leads to the following lower limit condition for cavity resonators:

$$I_{in} > \frac{\alpha}{\beta} \frac{\varsigma_{SPA}}{\varsigma_{TPA}} = \frac{\alpha}{\beta} \frac{(1 + R_2)(1 - \sqrt{R_1 R_2})^2}{T_0 (1 + R_2^2 + 4R_2)}. \tag{67}$$

Because the SPA and TPA inside the cavity are very weak if the incident power is not very high, a perturbation approach is chosen to deal with the absorption within the cavity. As presented here, the first step is to assume that there is no absorption in the cavity, and then the obtained field is used to calculate the light intensity in the cavity. The calculated light intensity can be used to determine the absorption and TPA-induced photocurrent in the cavity.

3.8 Final Comments

A review on the transfer matrix method (TMM) for distributed Bragg reflectors (DBR) and microcavities has been presented. The optical properties of semiconductor microcavities are useful for enhancing the interaction of the incident light at resonance wavelength with the medium in the active region of the microcavity. In particular the dependence of the reflectivity of a microcavity and the refractive index of the material on the absorption of the cavity can be used as the basis for an optical detector. In the next chapter the design of the semiconductor microcavity for nonlinear optical detection will be discussed in detail.

4 Device Simulation

The models used to assess the microcavity design were described in Chapter (3.6). The exact numerical approach is necessary to include wavelength dependent factors such as the phase and reflectance of the DBR mirrors.

It also facilitates calculations where the cavity is made up of different material layers and allows consideration of the effects of off-axis beams. The numerical calculations were performed using $MATLAB$, $Microcal^{TM}Origin^{TM}$ and $SimWindows$ software on a PC. Room temperature operation and an incident optical intensity low enough that nonlinear saturation or heating does not occur are assumed.

4.1 A Planar Microcavity

The structure primarily considered is a distributed Bragg reflector (DBR), which consists of a series of alternating high and low index quarter wavelength layers. A sketch of a semiconductor microcavity is shown in Figure (12). This cavity is constructed by a pair of DBRs with an active layer inserted between them. The thickness of the active layer is designed to be a multiple of half the absorption wavelength in order to maintain Bragg resonant modes. When sufficient multilayers L_1 and L_2 are stacked as DBRs, their reflectivity can be very high, Figure (13), and the field of the resonant mode is well confined within the active region. Here, it should be noticed that, since this type of cavity is open in the lateral directions and DBRs have dispersive features as a function of the incident angle of the light, there exist not only the resonant cavity modes but also leaky modes and propagation modes. Light in a propagation mode would travel along the active region in a lateral direction in Figure (12). The width of the stop band of the cavity is governed by the refractive index ratio of the multilayers L_1 and L_2, Figure (14), see also Equation (70) on page 58.

The low (high) index material is usually $AlAs$ ($GaAs$) where the refractive index is a function of wavelength, doping concentration and free carrier concentra-
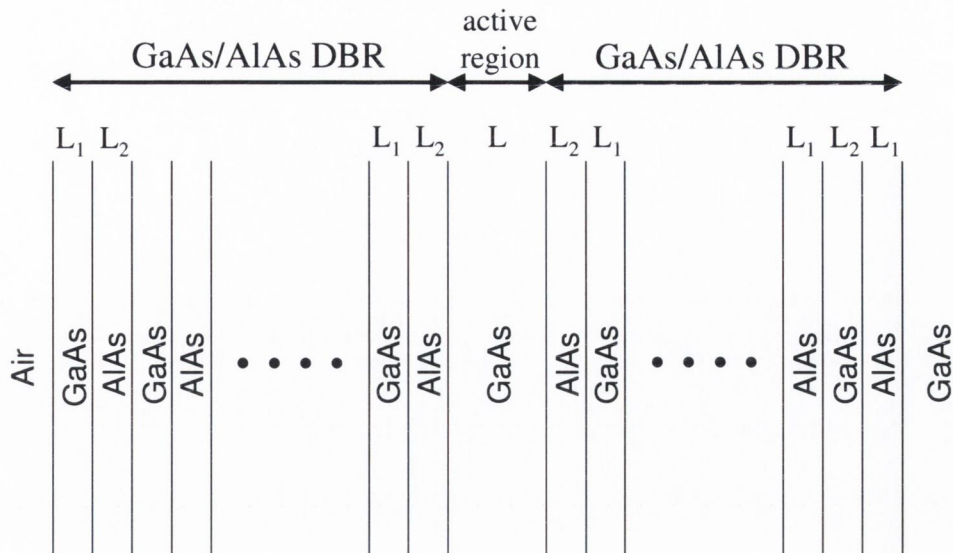
Figure 12: *Schematic representation of a Bragg stack, or microcavity used in the model. The middle layer, also called the active region, has a variable width and acts as an impurity. The incident medium is air and the substrate is GaAs. The DBR layers of thickness L_1 and L_2 consist of GaAs and AlAs respectively.*

tion. For some experiments it can be useful to use $Al_xGa_{1-x}As$ instead of $GaAs$. The material layers are usually grown by Metal-Organic Vapour Phase Epitaxy (MOVPE) or Molecular Beam Epitaxy (MBE). Most of the material properties for $Al_xGa_{1-x}As$ can be found in the literature [85]. Most of the literature and publications however do not give an analytic expression for the wavelength dependency of the refractive index. For an exact calculation of the refractive index of $Al_xGa_{1-x}As$ for any given wavelength λ and index x we can use two different models. The results for the refractive indices of these two models do not vary much but considering the large number of Bragg mirror periods the variation in the calculated overall reflectivity of the Bragg mirrors is not negligible.
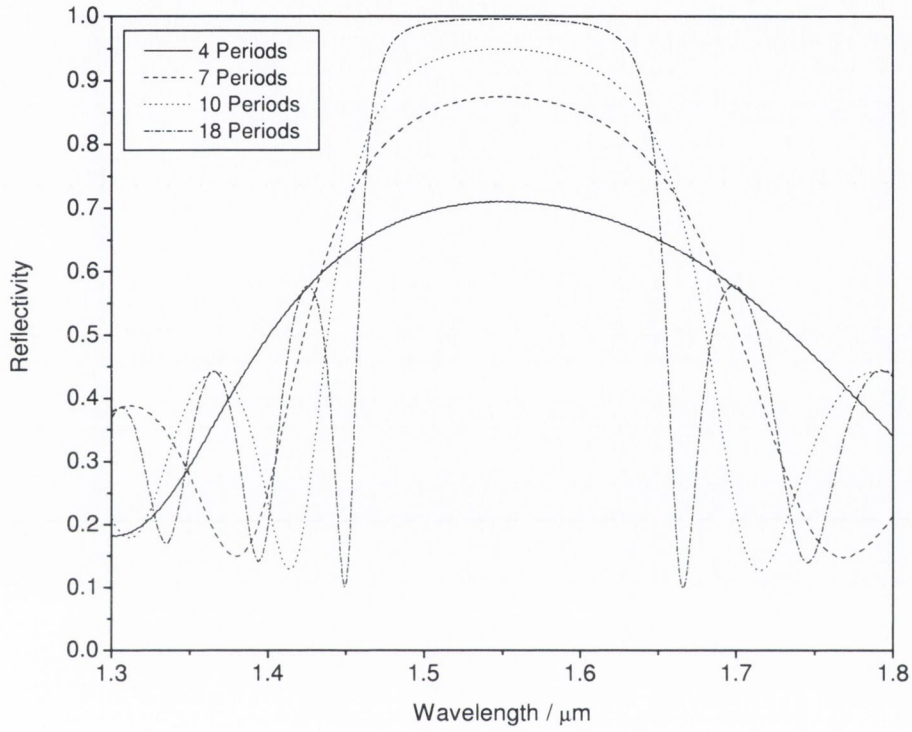
Figure 13: *Calculated amplitude reflectivity spectrum of a Bragg stack mirror on a GaAs substrate with increasing number of layer periods. The graph shows that the maximum reflectivity increases with the number of periods. The ratio of high and low refractive index was 1.17 (n_H=3.375, n_L=2.888) and the residual absorption 1 cm^{-1} in this case. The layer sequence is Air | H L H L ... H L | GaAs.*
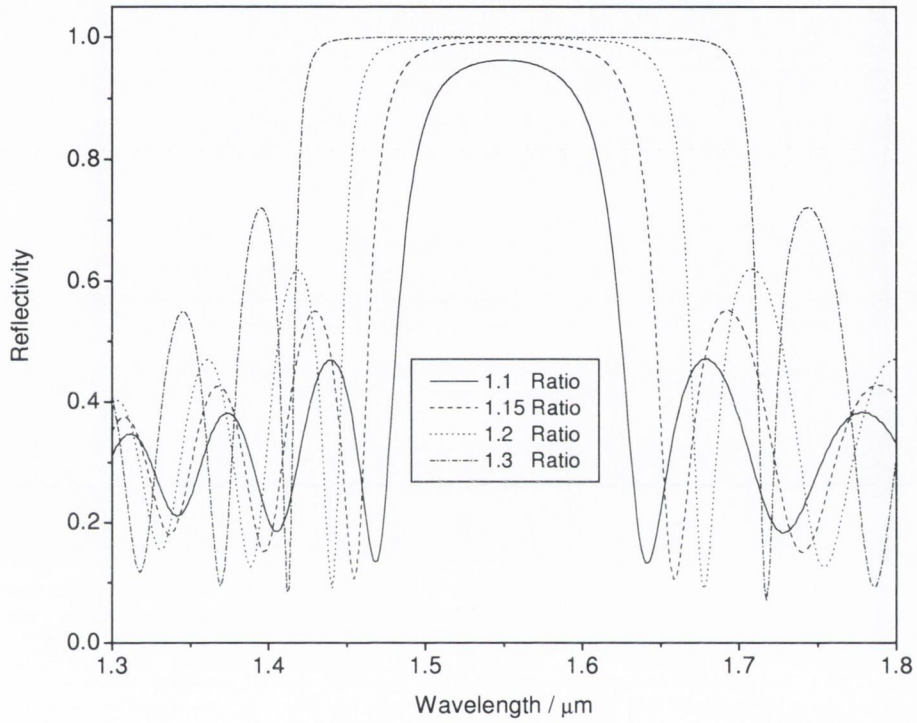
Figure 14: *Reflectivity of Bragg stack on GaAs with increasing refractive index ratio* $r = n_H/n_L$. *The stop band increases with increasing index ratio and for a fixed layer period (in this case 18) the maximum reflectivity also increases with index ratio. The layer sequence and the parameters are the same as in Figure (13).*

4.2 Afromowitz Model

Figure (15) shows the refractive indices for various $Al_xGa_{1-x}As$ alloys as a function of wavelength. The refractive index is a decreasing function of both increasing wavelength and aluminium concentration (only in the considered wavelength regime 800–1700 nm). The values for the different compositions of $Al_xGa_{1-x}As$ at 900 nm and 1550 nm are shown in Table (1) on page 56.
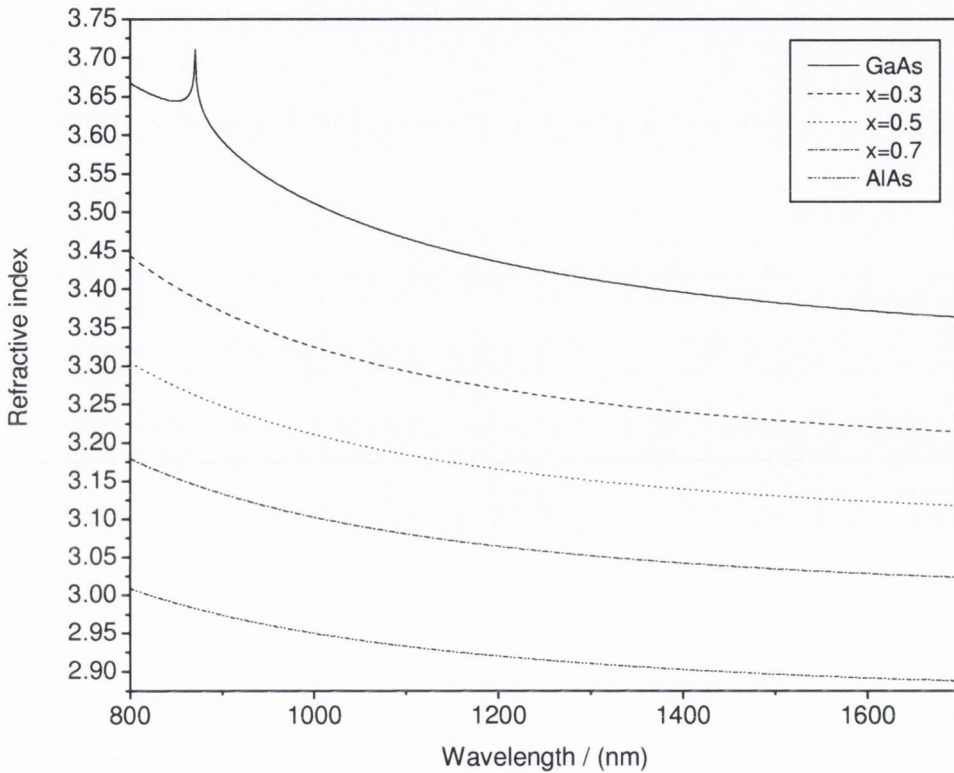
Figure 15: *Refractive indices for $Al_xGa_{1-x}As$ as a function of wavelength. Calculated after a model by A.M.Afromowitz [86]. The peak in the GaAs curve at 870 nm is due to the dispersion at the absorption bandedge. The refractive index decreases with both increasing wavelength and aluminium concentration.*

Accurate experimental refractive index values for the wide composition range of $Al_xGa_{1-x}As$ at energies below the fundamental band gap have not been available. This calls for the use of some sort of an interpolation scheme. The Afromowitz model has previously been successfully applied [87] to $GaAs/AlGaAs$ and

53

$InGaAsP/InP$ lasers. The model however still requires semi-empirically obtainable parameters and includes an approximation of the nonphysical absorption spectrum.

4.3 Gehrsitz Model

The Gehrsitz model is based on newer and therefore more reliable data. As the Afromowitz model it tries to analytically fit the optical properties of $Al_xGa_{1-x}As$ by extrapolating fitting between the measured data points. The resulting refractive indices are slightly higher than the ones given by the Afromowitz model, Figure (15).
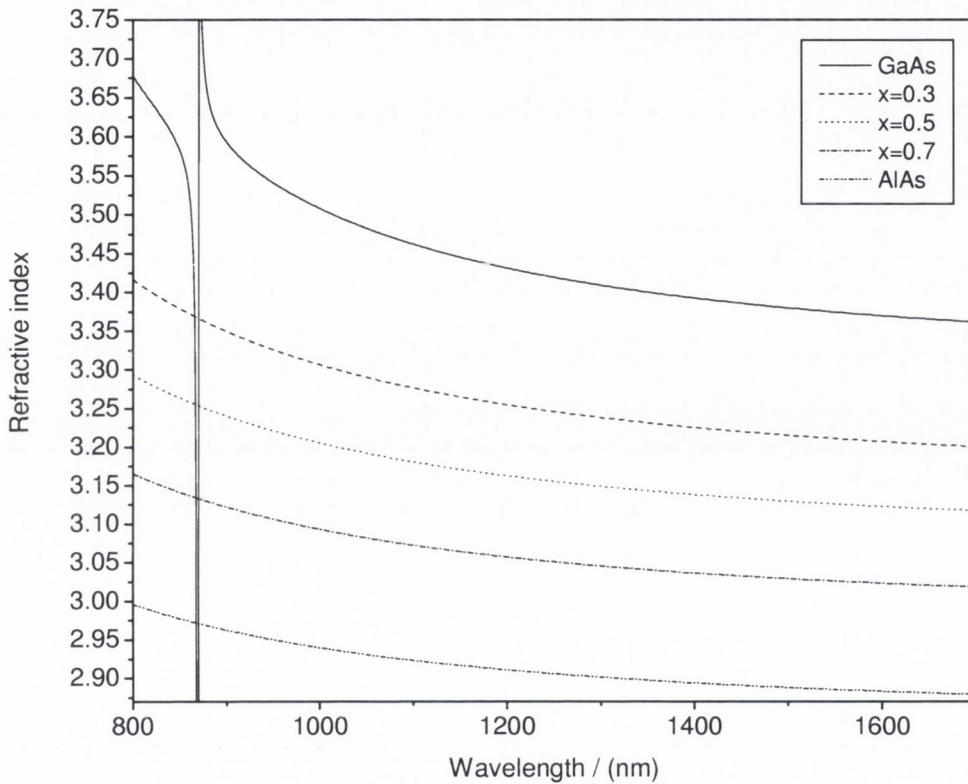
Figure 16: *Refractive index for $Al_xGa_{1-x}As$ as a function of wavelength. Model used by Gehrsitz [88]. The peak in the GaAs curve at 870 nm is due to the dispersion at the absorption band-edge. The shown singularity however is caused by an imaginary result in the calculation. The refractive index values are slightly higher than the values given by the Afromowitz model (Figure (15)).*

Table 1: Refractive indices for different AlGaAs alloys

Afromowitz	———	900 nm	1550 nm
$Al_{0.3}Ga_{0.7}As$	x=0.3	3.3707	—
$Al_{0.5}Ga_{0.5}As$	x=0.5	3.2481	—
AlAs	x=1	2.9739	2.8938
GaAs	x=0	3.5928	3.3769
Gehrsitz	———	900 nm	1550 nm
$Al_{0.3}Ga_{0.7}As$	x=0.3	3.3498	—
$Al_{0.5}Ga_{0.5}As$	x=0.5	3.2405	—
AlAs	x=1	2.9626	2.8852
GaAs	x=0	3.593	3.375

4.4   Finesse

For the calculation of the micro-cavity reflectivity a Transfer Matrix Model (TMM) has been used, Chapter (3). The refractive indices for the $Al_xGa_{1-x}As$ alloys used in the micro–cavity design, are shown in Table (1).

Using the front DBR reflectivity R_1 and the back DBR reflectivity R_2 of the structure it is possible to calculate the overall reflectivity of the cavity

$$R = \sqrt{R_1 \cdot R_1}. \tag{68}$$

The following expression defines the finesse of the microcavity, only dependent on the overall reflectivity.

$$F = \frac{\pi}{2} \cdot \sqrt{\frac{4 \cdot R}{(1 - R)^2}} \tag{69}$$

The calculated values of the finesse for different cavities and different wavelength are given in Table (2).

Table 2: Mirror reflectivity and finesse

900nm Afromow.	FM(15.5)	92.0%
	BM(35.5)	99.1%
	Finesse	**68**
900nm Gehrsitz	FM(15.5)	92.4%
	BM(35.5)	99.2%
	Finesse	**72.2**
1550nm Afromow.	FM(10)	94.7%
	BM(18)	98.5%
	Finesse	**90**
1550nm Gehrsitz	FM(10)	95%
	BM(18)	98.6%
	Finesse	**96.1**

For the design of the samples both models have been used. For the final samples however, the Gehrsitz model corresponds best with the experimental data.

4.5 Dielectric Mirror Spectral Bandwidth

A main feature of dielectric mirrors is the spectral dependence of the reflectivity. A measure of the full width of the high reflectance band (stop band) is given by [82],

$$\frac{\Delta\lambda}{\lambda} = \frac{4}{\pi} sin^{-1} \left(\frac{n_H/n_L - 1}{n_H/n_L + 1} \right) \qquad (70)$$

where $\Delta\lambda$ is the range of wavelengths over which the reflectance increases invariably with an increasing number of periods, Figure (14). $AlAs/GaAs$ DBRs possess the highest index ratio of any lattice matched semiconductor of 1.2 which leads to a bandwidth of $\Delta\lambda = 180$ nm at $\lambda = 1.55 \, \mu m$. The bandwidth is independent of the layer number p, although a flat high reflectance band is only achieved for sufficiently high p, greater than 3. It is obvious that maximizing the index ratio is an important factor in reducing the number of layers to be grown. One possibility to reduce the number of front Bragg layers would be modification of the front DBR by oxidizing the $AlAs$ layers after growth to produce an insulator Al_xO_y layer which has also a very low refractive index of 1.8 [89]. The resulting mirror can provide a very wide stop band and high reflectance with about 4 periods. Low threshold [90] and high efficiency [91] vertical cavity lasers have been produced with this technique with improved mode confinement. Problems however arising for the use of this technique with VCSELs due to the insulating layer in terms of pumping would not affect the use in TPA microcavities. The contacts for measuring the photocurrent in an TPA microcavity layout would have to be placed next to the active region. This could be achieved by etching of the grown DBRs and contacting the active layer.

4.6 Microcavity Resonance

Figure (17) shows the plot of the microcavity reflectance for a typical λ-cavity and normal incidence. The high reflectance window around $\omega = \omega_C$ originates from the stop bands of the two Bragg mirrors. The cavity mode appears as a

very narrow peak at the center of this region. Outside the stop band, a rather pronounced peak structure appears. This structure arises from the interplay between the oscillations in the reflectance of the two mirrors outside the stop bands (Figure (14)). It can be given various physical interpretations. In particular, the minima in reflectivity outside the stop band can be interpreted as confined modes other than the main mode, arising from peaks in the DBR reflectivity outside the stop band. These modes present a linewidth larger than the linewidth of the main cavity mode, because the mirror reflectivity is much smaller than at the stop band center. These cavity modes exist for all DBR microcavities. They are called *leaky modes*, because the electromagnetic field can leak outside the structure more efficiently at the corresponding frequencies. Leaky modes are a very important feature of microcavities and play a crucial role in the design of microcavity light emitting devices. They are very efficient channels for emission into the substrate, where the light is absorbed.
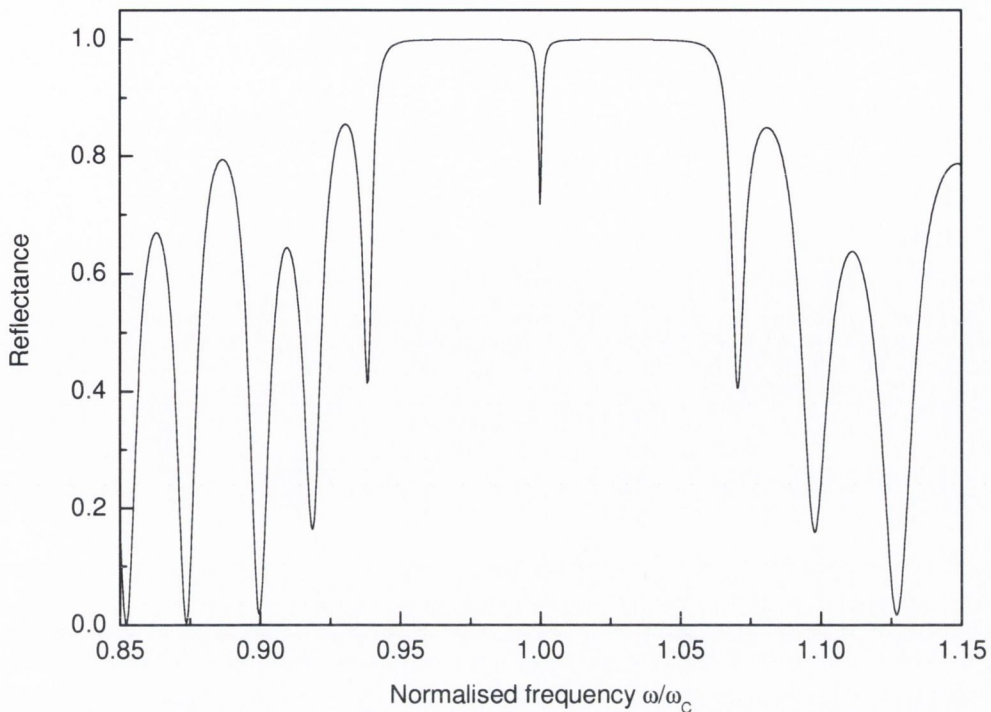
Figure 17: *The reflectance of a λ-microcavity with DBRs as a function of the normalized frequency. The indices are $n_C = n_H = n_r = 3.38$, $n_L = 2.88$ and $n_l = 1$, while the number of pairs is 10 for the left DBR and 18 for the right DBR. The spacer thickness is $L_C \simeq 459$ nm. The frequency resonance peak appears clearly at the center of the stop band.*

It is not possible to make DBR mirrors that have wavelength and incident angle independent reflectivity. This section will discuss the main limitations of Bragg mirrors such as the finite reflection angle and the mirror penetration depth.

4.7 Penetration Depth in Bragg Mirrors

The mirror penetration depth into a DBR gives an indication of how far the electric field extends from the active region into the stack of Bragg layers. Due to the distributed nature of a DBR, these mirrors exhibit phase dispersion and a finite delay upon reflection. The dispersion is responsible for the pulse broadening and pulse distortion [84, 92], whereas the reflection delay adds to the laser cavity

round-trip time. The sum of the physical cavity length and the mirror penetration depth gives the effective cavity length. Here we consider two definitions of the penetration depth: the definition by reflection delay (phase penetration depth L_τ) and by energy storage (energy penetration depth L_e). The used model is an exact analytic expression for both definitions. The functional dependence of L_τ and L_e on the number of layers is shown in Figure (18). Also included is the loss (dissipative) penetration length L_d. Typical reflectivity values for the Bragg mirrors used are close to 98%. Because the cavity mirror losses are proportional to $ln(R) \sim 1 - R$ any small variation of R produces large changes in loss.
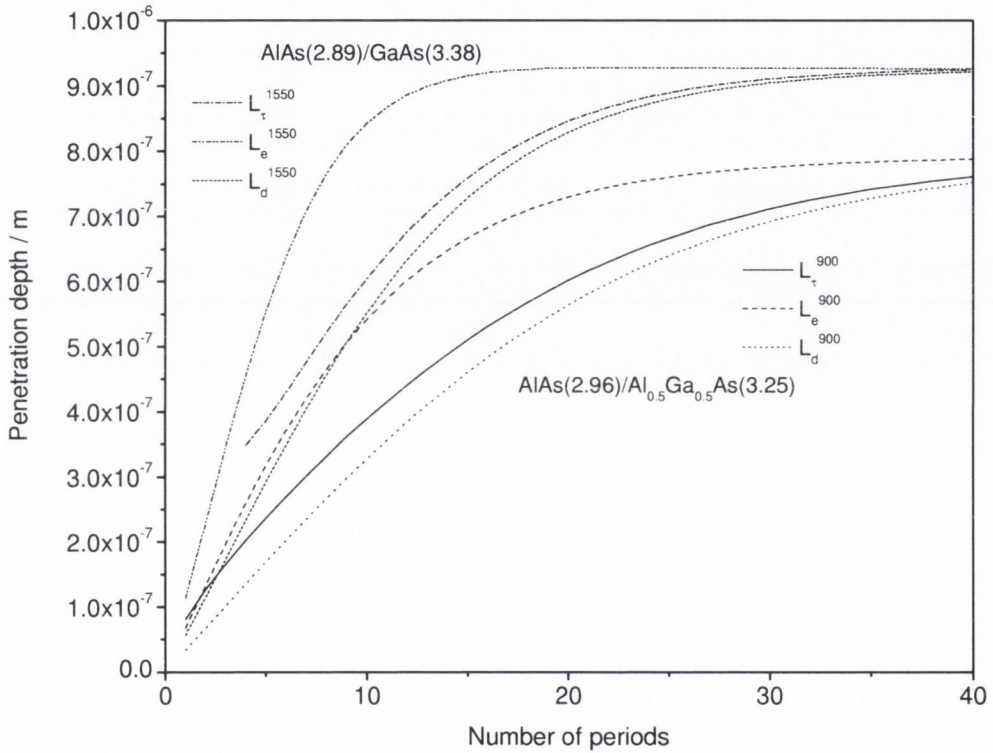
Figure 18: *The comparison between the penetration depths L_τ, L_e and L_d for two quarter-wave mirrors: $AlAs - Al_{0.5}Ga_{0.5}As$ and $AlAs - GaAs$. The refractive indices of the materials are calculated using a Model by Gehrsitz and are given in parentheses. The exit medium is GaAs and the incident medium is $Al_{0.3}Ga_{0.7}As$ and GaAs, respectively [93].*

61

L_τ and L_e can be analytically expressed as [93]:

$$L_\tau = \frac{c\tau}{2n},$$ (71)

where τ is the normalised reflection delay, given by [93]

$$\tau = \frac{2\lambda_0}{c} \frac{q}{1-p} \frac{(1-a^2p^{m-1})(1-p^m)}{(1-q^2a^2p^{2m-2})}.$$ (72)

Here the factor q is the ratio of the refractive indices at the interface between the incident medium and the first Bragg layer. The factor a is the ratio of the refractive indices at the interface between the last Bragg layer and the substrate medium, p is the ratio of the refractive indices of the two materials that build up the DBR structure. The number of sections in the quarter-wave stack is m. The energy penetration depth is given by

$$L_e = \frac{\lambda_0}{4n}\Lambda,$$ (73)

where Λ is the normalized energy penetration depth, given by [93]

$$\Lambda = \frac{q}{1-p} \frac{(1+a^2p^{m-1})(1-p^m)}{(1+q^2a^2p^{2m-2})}.$$ (74)

By taking the ratio, it can be shown that for finite m, L_e is always larger than L_τ.
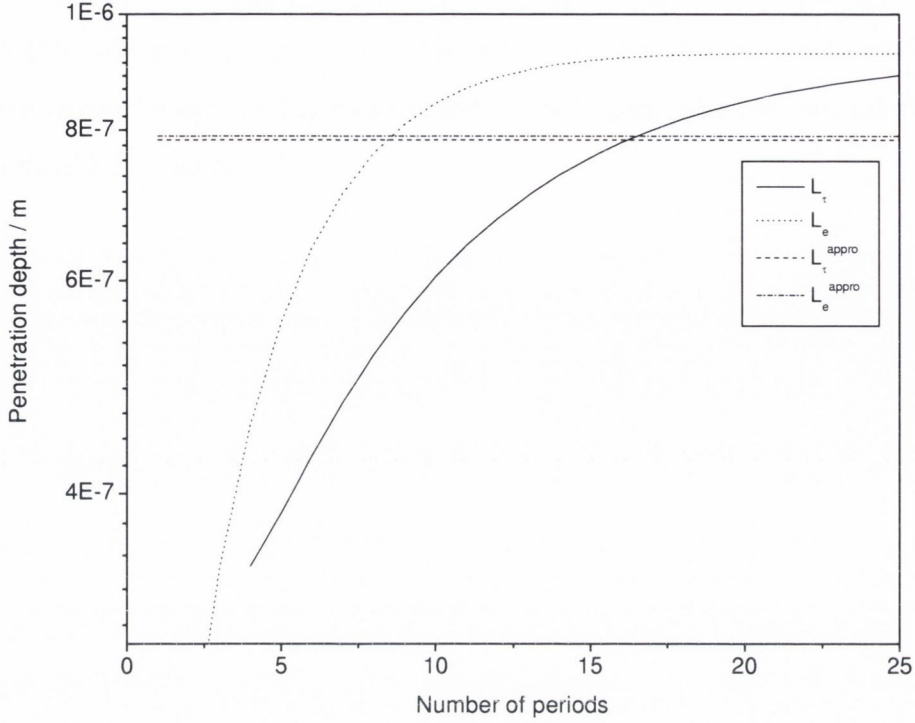
Figure 19: *The comparison between the penetration depths L_τ and L_e and the small material index difference approximation for the same AlAs-GaAs mirror as in Fig 18. For large number of periods the small material index difference approximation and the exact model value are reasonably close.*

For very small material index differences, however, it is possible to simplify the expressions for L_τ and L_e.

$$L_\tau = \frac{tanh(\kappa \cdot l)}{2 \cdot \kappa} \tag{75}$$

$$L_\tau = L_d \tag{76}$$

$$L_e = \frac{tanh(2 \cdot \kappa \cdot l)}{2 \cdot \kappa} \tag{77}$$

Taking the penetration depths for the front Bragg mirror and back Bragg mirror and adding these to the physical cavity length gives for the 1.55 μm micro-cavity an effective cavity length of 1.9 μm. The 1.55 μm micro-cavity is a 4λ cavity. The effective cavity length for the 890 nm device is 1.5μm. The 890 nm micro-cavity is therefore a 5λ cavity.
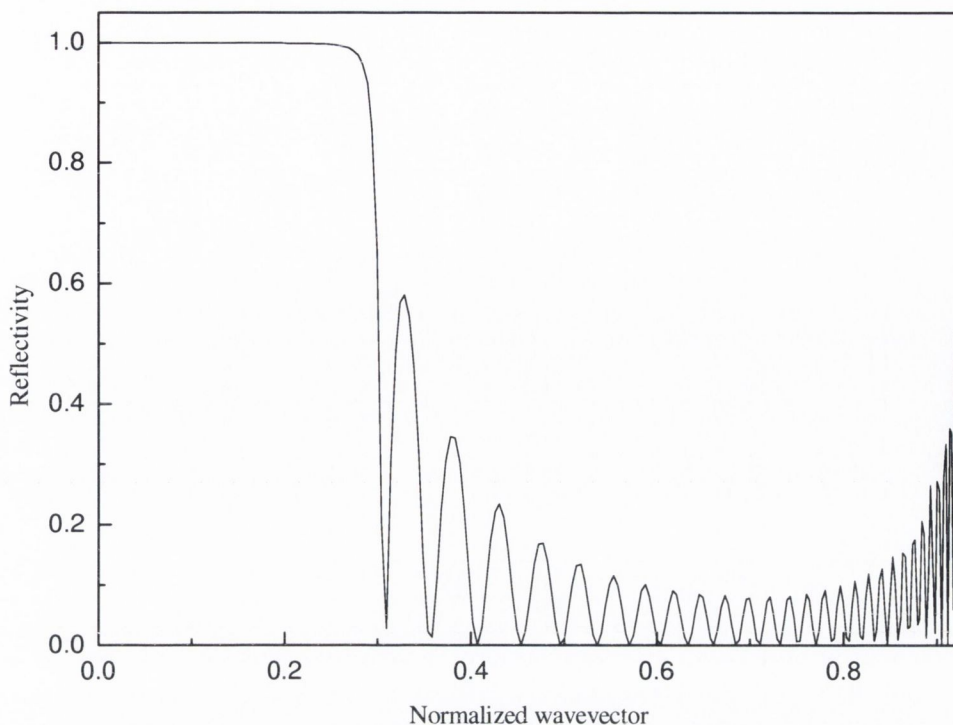
Figure 20: *The reflectance of a DBR at mirror resonance as a function of the normalised wave-vector (TE only). The refractive index of the incident material is 3.3 and the DBR consists of 35 periods, n_H=3.3 and n_L=2.8.*

4.8 Finite Reflection Angle

Within a given frequency window the DBR has a very high reflectivity coefficient. This property is preserved also for different incident angles. To show this, in Figure (20) the reflectance of a DBR for its central frequency $\omega_m = \nu\pi/\lambda$ and TE polarization as a function of the normalized in-plane wave vector $\vec{k}_\parallel/k_0$ is plotted, where $k_0 = \omega_m/\nu$ and ν is the velocity of the light in the medium of the incident wave.

The reflectance outside the stop band shows a highly oscillatory behaviour. The reflectance is characterized by a number of peaks corresponding to the number of layer pairs in the DBR. These peaks correspond to side resonances due to

65

the multiple interference in the structure. These resonances are fundamental to the physics of any semiconductor microcavity device. Figure (21) shows the reflectivity of a DBR as a function of wavelength for different incident angles.
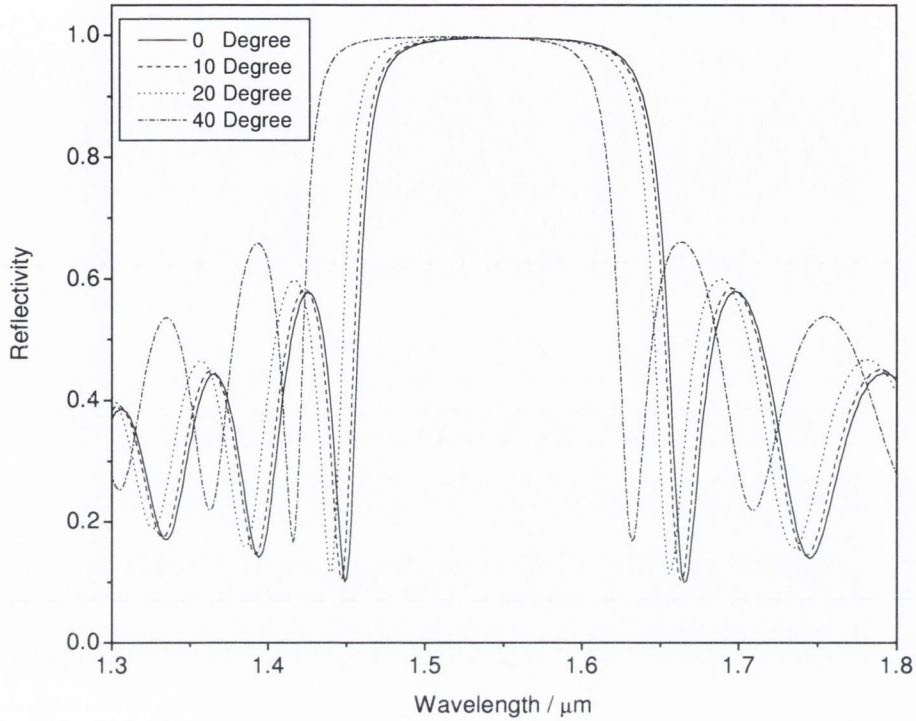
Figure 21: *Reflectivity of Bragg stack mirror on GaAs with increasing incident angle (normal incident = 0 degree). The stop band shifts to lower wavelength with increasing incident angle while the maximum reflectivity stays constant. A fixed layer period is 18 and the index ratio is 1.17. The layer sequence and used parameters are the same as in Figure (13)*

The transmitted angle of the plane wave when it enters a film of optical thickness $n_{eff}L$ from an incident medium of refractive index n_0 is given by Snell's law [79]

$$\theta_t = sin^{-1}\left(\frac{n_0 \, sin(\theta_i)}{n_{eff}}\right) \qquad (78)$$

66
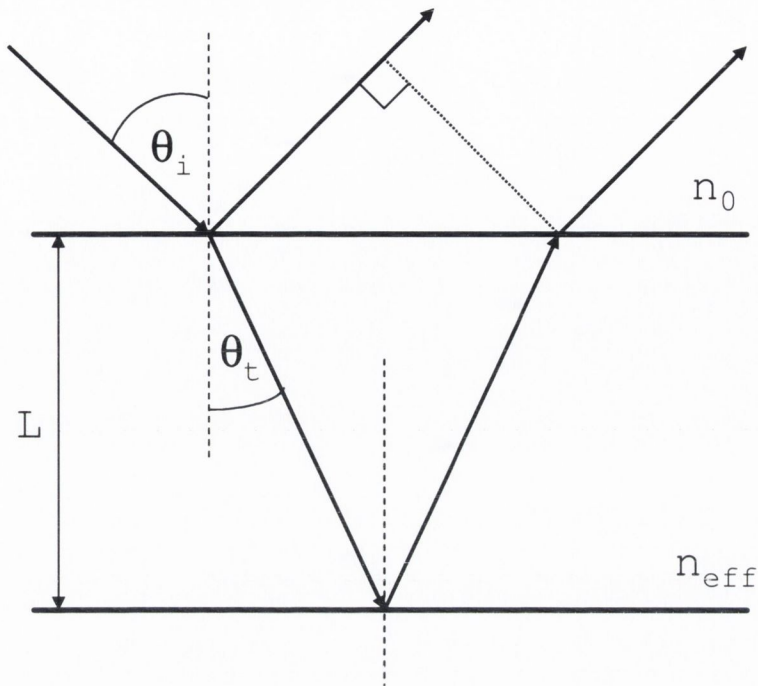
Figure 22: *Interference between two light waves reflected from the upper and lower surfaces of a thin film with thickness L. The path differences and phase shifts at the surfaces cause some wavelengths of light to interfere constructively and others to interfere destructively. According to the change of the incident angle θ_i the interference conditions changes.*

where θ_i and θ_t are the incident and transmitted angles as shown in Figure (22).

The optical path length inside the film is $2n\,L/cos(\theta_t)$ for a double pass. However, the distance after which the wave coincides with itself, corresponding to a phase change of $2m\pi$, is shortened to $2\,n\,L\,cos(\theta_t)$. As a result, the effect of tilting the incident beam is a stop band shift to shorter wavelength.

4.9 Microcavity Mode

As discussed previously, a planar microcavity can modify the single-photon and two-photon absorption rates by confining and enhancing the electric field within the active region. Ujihara has given a formula for the mode volume of a fundamental planar microcavity mode [94]. The mode volume and the mode radius are respectively given by the following expressions:

$$V = \frac{\pi \lambda L^2}{1 - R} \quad , \quad r = \sqrt{\frac{\lambda L}{1 - R}} \tag{79}$$

Here the cavity length L is assumed to be an integer multiple of half a wavelength λ. This formula shows that the mode volume is proportional to the square of the cavity length for constant mirror reflectivity. For the microcavity device resonant at 1550 nm, with an effective cavity length L of 4λ, Equation (79) would give a mode volume of $5.82 \times 10^{-15} \; m^2$ and a mode radius of 17.3×10^{-6} m.

4.10 Final TPA Microcavity Design

As outlined previously a TMM approach has been used to assess the TPA microcavity design. The calculations have been carried out using $MATLAB$ software on a PC. The main assumption made when modelling concern the values of refractive index for different materials and different wavelengths. For the design of the microcavities the refractive indices given by the Afromowitz model were used. A detailed review of the optimisation process of resonant cavity enhanced photonic devices may be found in references [56, 95].

The final layer structures for the 890 nm and 1550 nm device are shown in Table (3) and (4), respectively. The change of refractive index with doping is taken into account calculating the DBR layer thickness, detailed data on doping induced refractive index changes is taken from the following references [85, 96].

Table 3: Layer Structure for 890 nm TPA microcavity (QT1516)

Layer No	Material	Repeat	Thickness(nm)	Doping(cm^{-3})	Dopant
6	AlAs	15	74.8	3E+18	Carbon
5	$Al_{0.5}Ga_{0.5}As$	15	67.7	3E+18	Carbon
4	$Ga_{0.7}Al_{0.3}As$		270.0		None
3	$Al_{0.5}Ga_{0.5}As$	35	67.7	3E+18	Silicon
2	AlAs	35	74.8	1E+18	Silicon
1	GaAs	1	61.5	1E+18	Silicon

Table 4: Layer Structure for 1550 nm TPA microcavity (QT1643)

Layer No	Material	Repeat	Thickness(nm)	Doping(cm^{-3})	Dopant
7	GaAs		116.7	2E+19	Carbon
6	AlAs		134.3	3E+18	Carbon
5	GaAs	9	115.7	3E+18	Carbon
4	AlAs	9	134.3	3E+18	Carbon
3	GaAs		458.9		None
2	AlAs	18	134.3	1E+18	Silicon
1	GaAs	18	115.7	1E+18	Silicon

To conclude this section a number of points are outlined relating to some of the assumptions that have been made in the calculations above. The first issue concerns the change of the refractive index with carrier density. The average power incident on the device is usually too small for this effect to have a major influence. The second issue is the question of the residual single photon absorption due to the Franz-Keldysch effect and impurities in the active layer. This effect is fully included in the program used to calculate the TPA-induced photocurrent. Third, issues also to be considered are thermal effects, absorption in the Bragg mirrors and lateral diffusion of carriers. These effects include difficult computations and have not been attempted here. Only for the absorption in the Bragg mirrors

a small analysis has been presented in this chapter. The first two issues are complications that for simplicity have not been included in the description but are included in the $MATLAB$ program used for the simulations in the following chapters and would be necessary in a full treatment of the optical properties of the TPA microcavity.
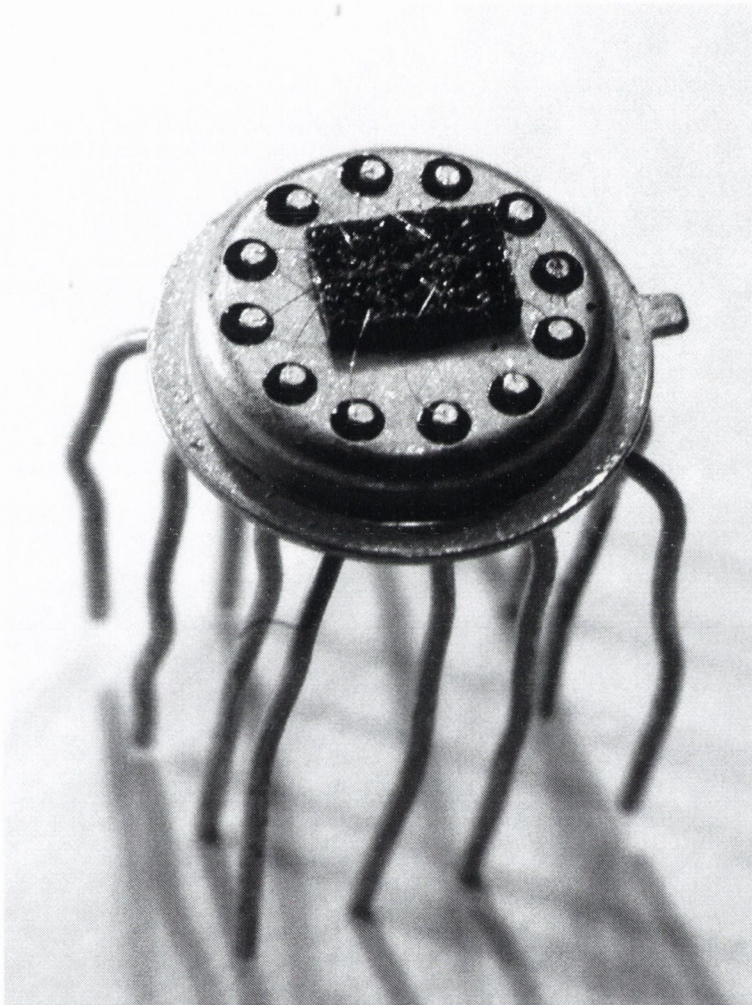
Figure 23: *Picture of TPA microcavity device including sample mount and contacts. On each sample mount 11 device are connected via gold wires to the outer ring of contacts.*

5 Measurements at 890 nm

5.1 Introduction

The novel concept of TPA in microcavity devices is presented in this chapter using a proof-of-concept device.

5.2 Device

The proof-of-concept device with a cavity resonance at 890 nm is basically a *AlGaAs* PIN microcavity photodetector, grown on a (001) *GaAs* substrate. Reflectivity measurements are shown in Figure (24).
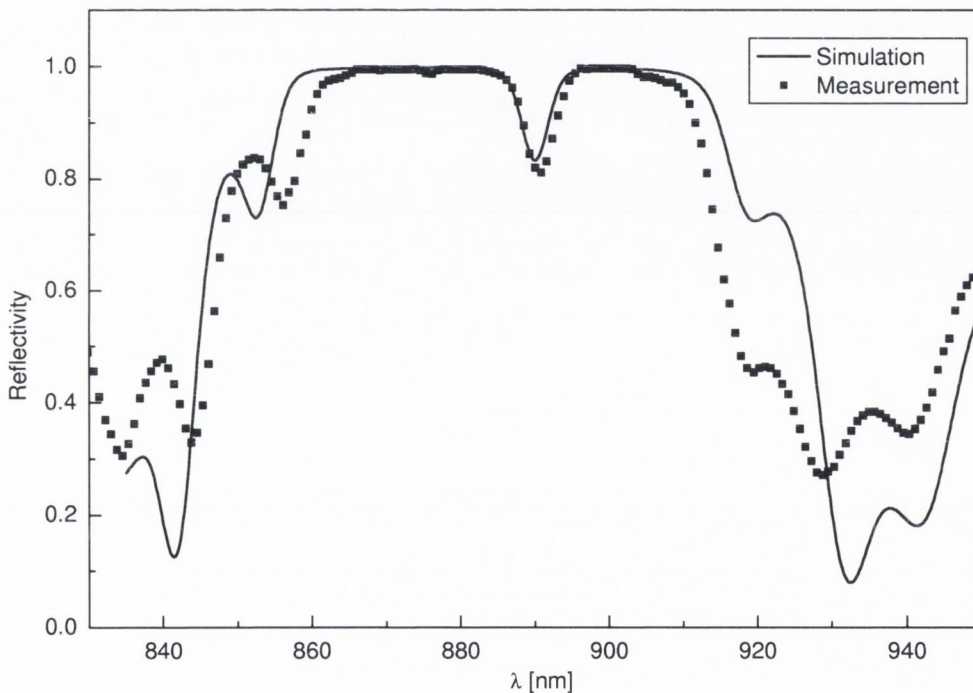
Figure 24: *Reflectivity simulation and measurement for wafer QT1516R, resonance wavelength at 885 nm, centered in the Bragg stop-band. The microcavity mode has a linewidth of $\approx$ 3 nm. The solid line shows the simulation results for the device obtained using the TMM.*

Simulations using TMM are in good agreement with the experimental measure-

ments. The layer refractive indices are taken from the Gehrsitz model and produce the best fit to the measured data. The differences can be easily explained by small fluctuations of the layer thickness (see Section (6.1.2) for explanation). The device has a 0.27 μm $Ga_{0.7}Al_{0.3}As$ active region embedded between two $Ga_{0.5}Al_{0.5}As/AlAs$ Bragg mirrors. The front mirror is p-doped (C–$10^{18}cm^{-3}$) and consists of 15.5 pairs while the back mirror is n-doped (Si–$10^{18}cm^{-3}$) and contains of 35.5 pairs designed for maximum reflectivity at 890 nm. The bandgap of the active region material $Ga_{0.7}Al_{0.3}As$ is 1.85 eV (670 nm). In case of wafer $QT1516R$ the designed overall reflectivity R of the cavity was $R = 0.973$. To calculate the overall reflectivity R, the following equation was used

$$R = \sqrt{R_1 \cdot R_2} \tag{80}$$

where R_1 and R_2 are the front (back) mirror reflectivity respectively. The devices studied were 400 μm, 200 μm, 100 μm and 50 μm diameter vertical structures.

5.3   Experimental Set-up

As a light source a tunable Tsunami Ti-Sapphire laser was used, delivering 1.6 ps pulses at 82 MHz repetition rate. A standard lock-in technique was applied to measure the photocurrent of the device. The load resistance was changed from 200 Ω to 500 kΩ to improve the measurement sensitivity if required. Alignment was made by forward biasing the photodiode which then acts as an LED emitting at 700 nm. This method allowed for a quick pre-focusing of the laser spot on the sample. The spot size was then adjusted by moving the microscope objective mounted on a xyz-mount. The laser spot size before the objective was 3.5 mm, and the beam was TE polarized. A ×10 0.25NA objective was used to focus the laser beam onto the device and the laser spot size (1/e) was assessed to be ∼7 μm. Once the TPA signal was detected the setup was optimized by adjusting the Ti-Sapphire laser wavelength to get a maximum TPA response, at the wavelength corresponding to the cavity resonance wavelength.

5.4   Device Characterization

The expected nonlinear quadratic response of the device can be seen in Figure (25). The photocurrent measurement was performed as a function of the incident power close to the cavity resonance. A standard Lock-In technique was used to measure the photocurrent and the load resistor was changed from 200 Ω to 500 kΩ for better sensitivity at lower optical powers. Also shown are the simulation results, where a TPA coefficient of β=0.013 cm/MW was assumed and a linear absorption of 0.1 cm^{-1}.
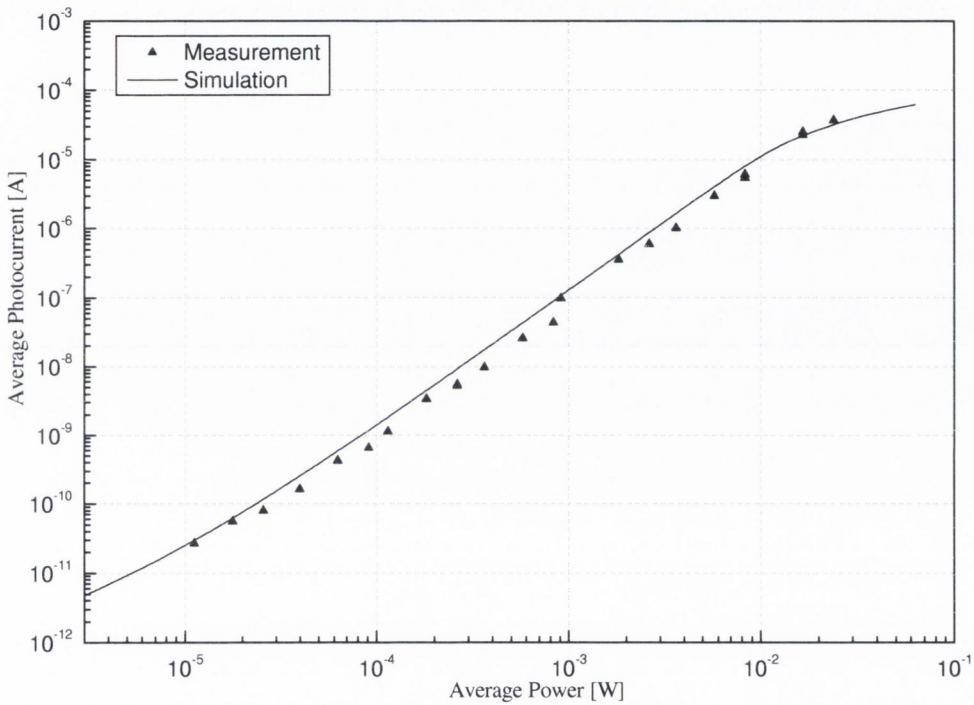
Figure 25: *Photo-current vs. intensity at 886 nm. Full line gives simulation result for $\beta = 0.013$ cm/MW and $\alpha = 0.1$ cm^{-1}. The structure of the device is described in Chapter (4.10). The experimental results as well as the simulation show a quadratic dependence of the TPA photocurrent vs. average incident power over almost 2 orders of magnitude.*

Then, for a given incident average intensity of 14 mW, a wavelength dependent photocurrent measurement around the resonance was performed, as shown in

Figure (26). An experimental enhancement of four orders of magnitude is reached. The photocurrent in Figure (26) is normalized to the TPA photo-current which would be measured for an active region of the same material and dimensions but with antireflecting mirrors instead of Bragg reflectors. The measured result is close to the simulation results.
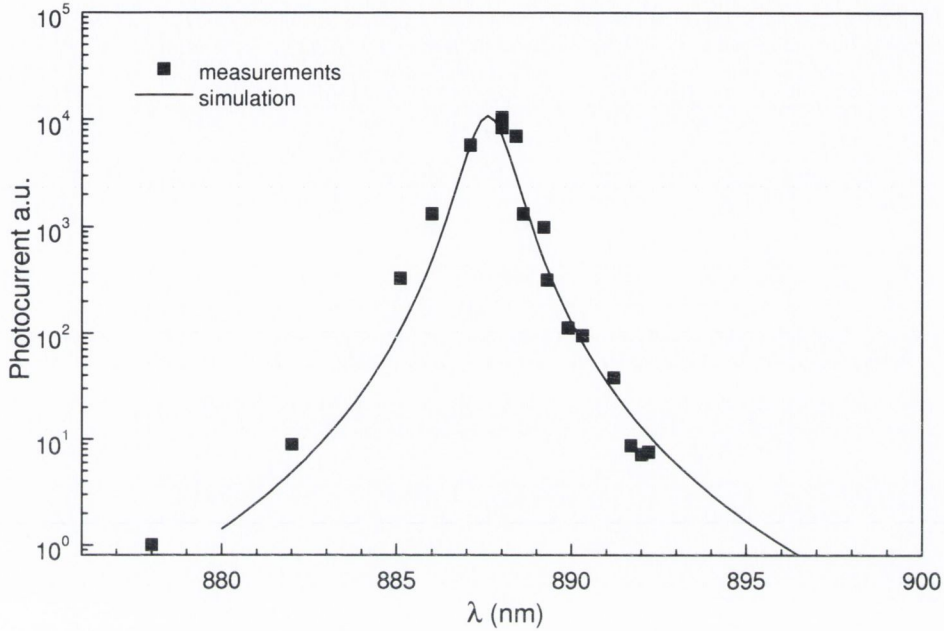
Figure 26: *Photo-current enhancement within the TPA micro-cavity device, measurements and simulation shown.*

In the model, the optical electric field incoming from the back side of the device is taken to be zero, while the emerging field is varied. Thus the incident electric field on the front surface of the device is varied, and this allows us to plot the photocurrent response versus the incoming intensity. This model approach has been used to study TPA in Bragg reflectors [97]. In the case of TPA it is possible to reduce the problem to the linear case by a self-consistent calculation of the intensity distribution of the standing waves in the structure, and deduce the equivalent linear absorption inside the cavity $\alpha(z) = \beta I(z)$. For the simulation shown in Figure (25) and (26), the device is divided into a number of layers

to allow for an accurate calculation of the saturation behaviour, in terms of determining the dynamic range. Typically the size of each layer in the TPA region is taken to be around 10 nm.

It is essential to take into account the TPA refractive index change. The following two contributions are included in the model. The first contribution comes from the non-linear refractive index n_2 [98]. The second contribution considered comes from the generation of carriers [99]. The model is a steady state model, therefore the temporal carrier index change can not be taken into account. This problem can be overcome by averaging the carrier density (N) seen by the pulse, i.e. N/2. In the TMM described earlier the k vector is then simply replaced by

$$ k = \frac{2\pi n}{\lambda} - i\frac{\beta I}{2} - i\frac{\alpha}{2}, \tag{81} $$

where

$$ n = n_0 + n_2 I + \sigma_n \frac{N}{2}. \tag{82} $$

The refractive index change per carrier density pair for this case is $|\sigma_n| = 4.2 \times 10^{-27} \ m^{-3}$, $|n_2| = 1 \times 10^{-17} \ m^2/W$ [73] and $N = 10^{19} \ cm^{-3}$. Here, the carrier induced refractive index change contribution is higher than the non-linear refractive index contribution.

The photocurrent is calculated by integrating the absorbed intensity inside the depleted region of the TPA microcavity.

$$ J = \int_0^L \frac{\eta_{TPA}\beta I^2(z)}{2E} + \frac{\eta_{SPA}\alpha I(z)}{E} dz \tag{83} $$

Here E is the incident photon energy given in eV, and the η factors account for the TPA and SPA photocurrent conversion efficiency respectively. These factors have been estimated at 11% and 3% respectively for $GaAlAs$ waveguides [100]. These rather low values have been explained by recombination processes but no calculations of the optical mode injection, confinement factors and losses have been made. For the presented results, a photocurrent conversion efficiency of

100% for both TPA and SPA in the undoped region and 0% in the DBRs was assumed.

5.5   Dynamic Measurements

For the PIN diodes from wafer $QT1516R$ a reverse breakdown voltage of 7 V was measured. The device was connected to a fast sampling scope and the photocurrent response to an 82 MHz, 1.2 ps pulse-train at 884 nm was measured. The average incident power was 110 mW. A 50 Ω resistor was used for higher sensitivity. Applying a high reverse voltage (3 V) reduces the time taken to sweep out the photo-carriers from the active region and improves the dynamic range of the device. It could be shown that the response time of the micro-cavity device can thus be reduced and the bandwidth enhanced, Figure (27). The full width half maximum duration of the response pulse is 1.2 ps and the corresponding response time (10% $\rightarrow$ 90% final peak value) for the biased TPA micro-cavity is 0.84 ns which gives a bandwidth of the device of 420 MHz.
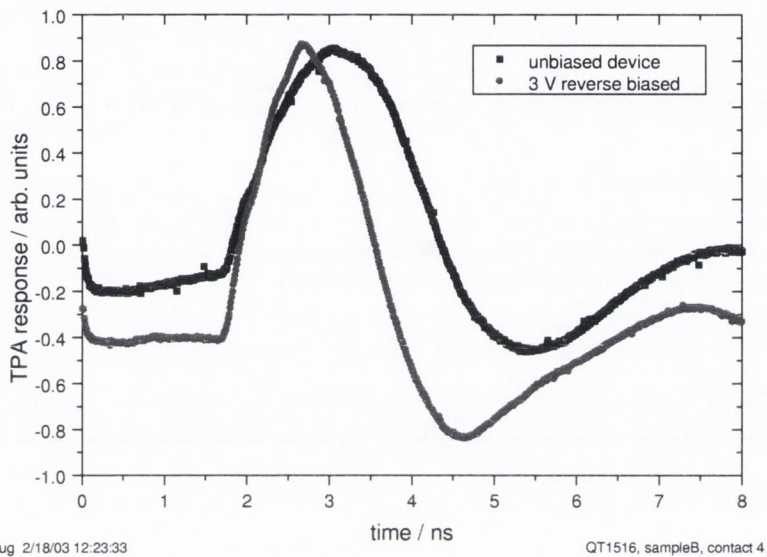
Figure 27: *Time-response of an unbiased and 3 V reverse biased device to a 1.2 ps pulse, the response-time for the biased TPA micro-cavity device is 0.84 ns (bandwidth: 420 MHz). The signal oscillation following the pulse response seems to be fundamental to the experimental setup since impedance mismatching and signal back reflection in the connection cables could not be avoided.*

6 Measurements at 1.55 μm

6.1 Introduction

One of the aims of this work is to investigate the potential of a TPA microcavity device as a practical device for optical telecommunication systems. For this purpose the resonance wavelength of the microcavity has to be at the telecommunication wavelength of 1.55 μm.

The first TPA microcavity structure in Chapter (5) used a DBR back mirror, an active layer and a DBR front mirror. The cavity resonance was at 890 nm. This basic structure layout was adapted for the design of the TPA microcavity device operating at 1.55 μm.

6.1.1 Device

A schematic of the device is shown in Figure (28). The layer structure of the device is given in Table (4). The structure was grown using MOVPE on an n^+-doped $GaAs$ substrate.

An 18 period DBR with alternating $AlAs/GaAs$ quarter wave layers was chosen to provide a back reflectance of 0.985 at 1.55 μm. Doping of the mirror layers was n-type, using a $Silicon$ (Si) concentration of $1 \times 10^{18} cm^{-3}$. On top of the back mirror an active layer of intrinsic $GaAs$ was placed, 458.9 nm thick corresponding to λ/n. A 10 period DBR with alternating $AlAs/GaAs$ quarter wave layers completed the cavity. The upper most $GaAs$ layer of the front DBR was p^{++}-doped, using a $Carbon$ (C) concentration of 2×10^{19} cm^{-3}. This was done for better contact to the contact electrode. The rest of the layers of the front DBR were p-type, using C to $3 \times 10^{18} cm^{-3}$. Using the transfer matrix model described in Chapter (3) the reflectance of the front Bragg mirror was calculated to be 0.95 at 1.55 μm.

The cavity was contacted on the highly p-doped $GaAs$ top layer of the front DBR and the n-doped $GaAs$ substrate. The simulated reflectivity spectrum of the device is shown in Figure (29).
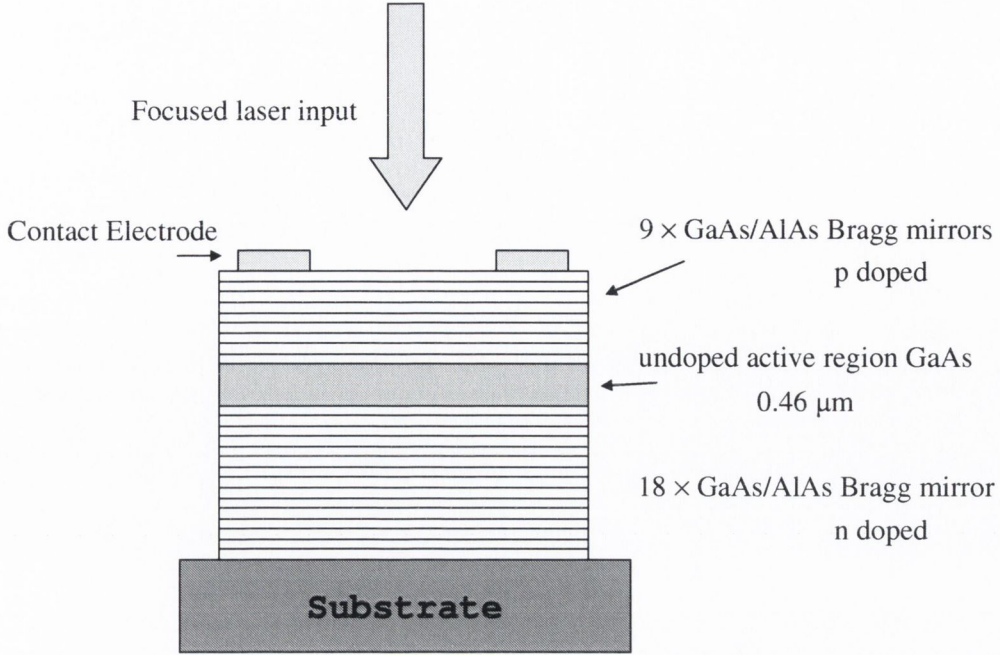
Figure 28: *Schematic of the TPA microcavity operating at 1.55 μm. The top contact, shown in cross-section is circular. The back contact is connected to the GaAs substrate. A variation of circular apertures were available, 400, 200, 100, 75, 50 and 25 μm.*

The cavity resonance is at 1.55 μm, centered in the Bragg stop band. The simulated microcavity mode has a linewidth of 2.15 nm as shown in Figure (30). Because of the wavelength dependence of the phase shift of the reflectivity of a DBR several definitions of the finesse can be used:

$$F = \frac{\text{Free spectral range}}{FWHM} = \frac{\lambda}{m\Delta\lambda} \qquad (84)$$

where m is the fringe order $\left(m = \frac{2 \times \text{cavity length}}{\lambda} \right)$. The FWHM mentioned here is the microcavity mode linewith. This definition of the finesse is consistent with Equation (69). See Chapter (3.7) for explanation. The Finesse can also be defined according to a local free spectral range or effective cavity length. Both are strictly equivalent [101].
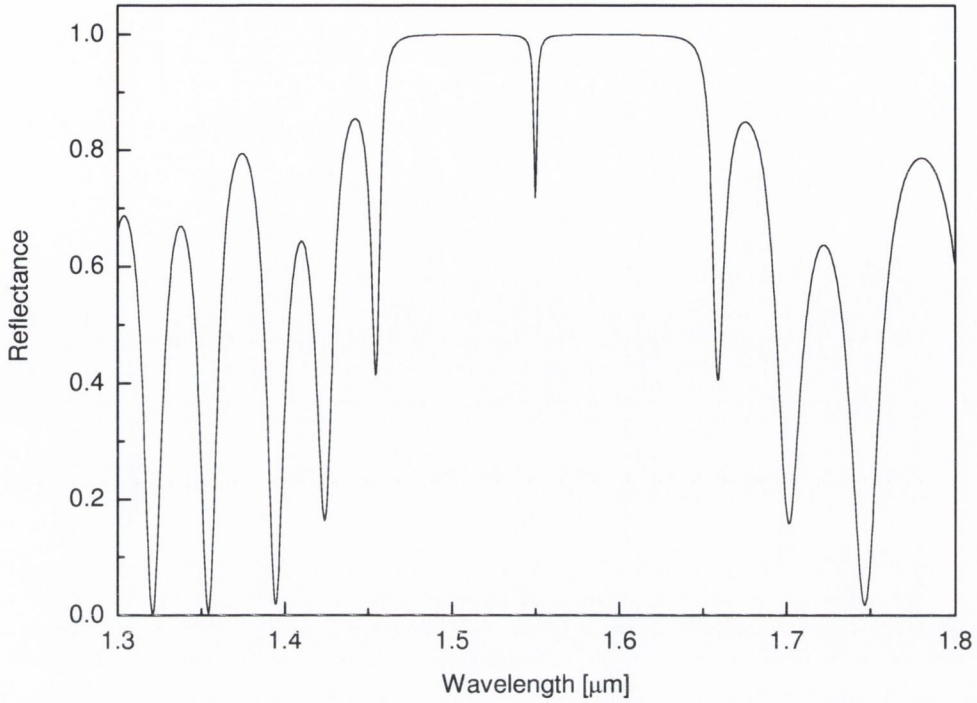
Figure 29: *Calculated reflectivity spectrum of an 10 × 18 pairs distributed Bragg mirror Fabry-Pérot microcavity. The active region thickness L_C is 458.9 nm. The incident medium is air and the substrate material is GaAs.*

$$F_{eff} = \frac{\text{Local free spectral range}}{FWHM} = \frac{\lambda}{m_{eff}\Delta\lambda} \qquad (85)$$

with $m_{eff} = m + m_0$. In the high reflectivity limit, m_0 can be described as

$$m_0 = \frac{n_L}{(n_H - n_L)}. \qquad (86)$$

For the 1.55 μm TPA microcavity, $n_H = 3.375$, $n_L = 2.885$ and $m_0 = 5.89$. A λ sized cavity is a second order cavity (m=2), with λ= 1.55 μm and $\Delta\lambda$= 4nm, this gives a finesse of 193. This analysis does not consider the penetration depth into the DBRs. Including the penetration depth into the DBR, the fringe order m for the 1.55 μm TPA microcavity is close to 4. This will give a finesse of 96.5,
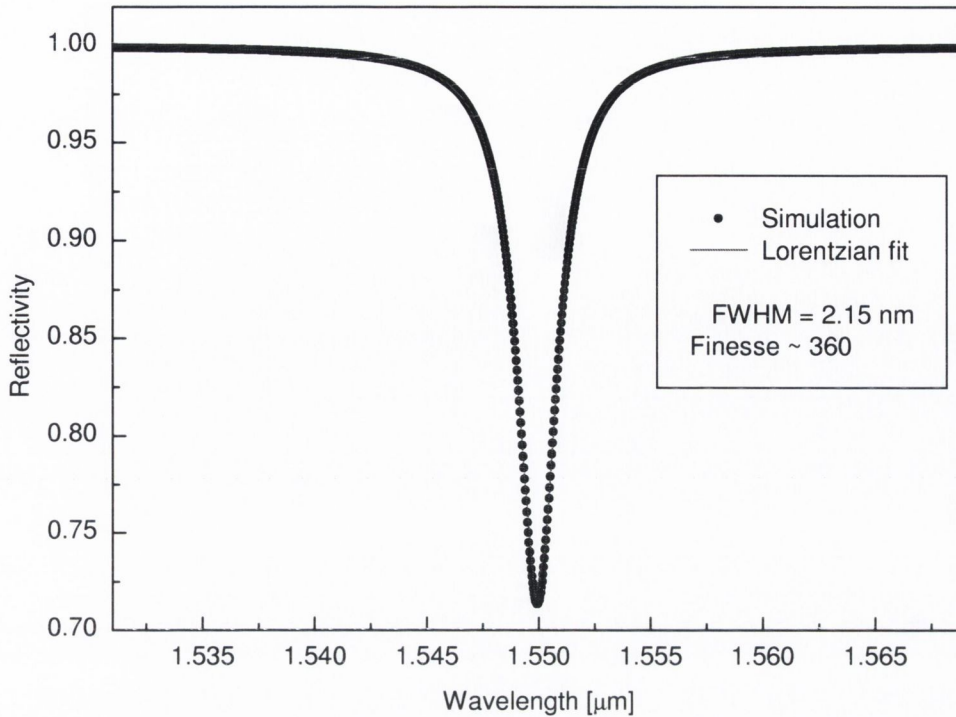
Figure 30: *Details of a Fabry-Pérot mode. The solid line is a Lorentzian fit with a full width half maximum of 2.15 nm. The cavity reflectivity at resonance can be very low for symmetric microcavities.*

which corresponds to the theoretical value given in Table (2). Although such finesses are much lower than for VCSELs and microwave cavities, they are more than adequate to reach the high enhancement in the semiconductor microcavity for two-photon absorption.

6.1.2 Device Characterization

This section presents a number of experimental results on the measurements of the TPA microcavity devices from wafer $QT1643A$. The design centre wavelength was $1.55\ \mu m$. It was intended to operate the microcavity device at $1.55\ \mu m$, but due to minor layer thickness variations during the growth process the actual microcavity resonances were located at slightly lower wavelengths. Reflectivity measurements

82

of the wafer $QT1643A$ at normal incidence are shown in Figure (31). The wafer was produced by Sheffield University.
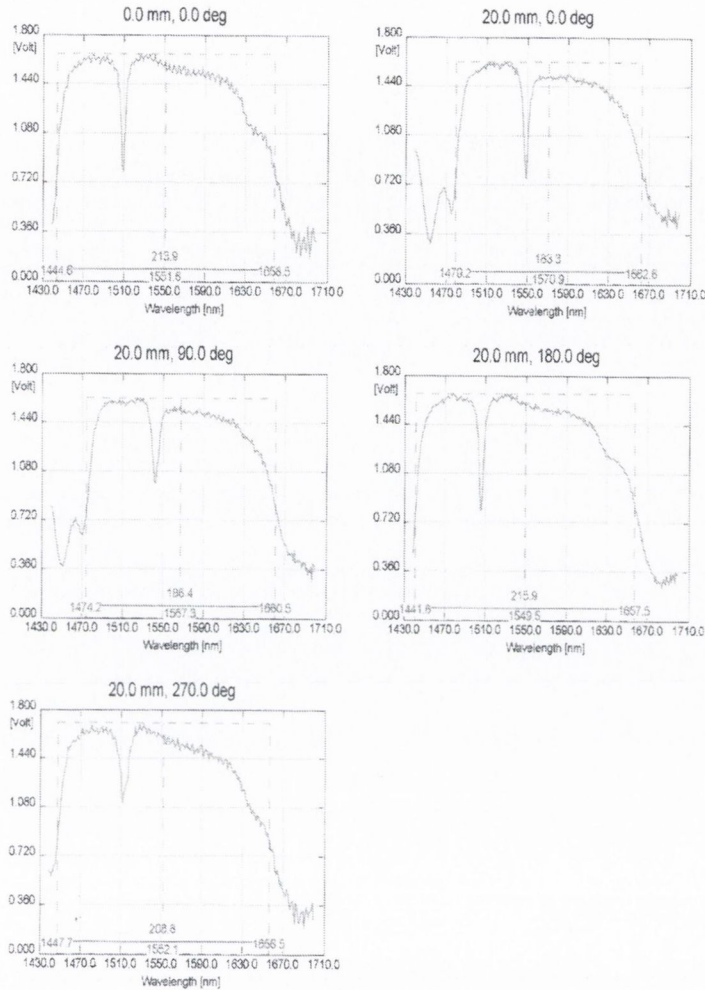
Figure 31: *Reflectance profiles for wafer QT1643A.*

The design parameters given in the previous sections obviously have a certain degree of uncertainty associated with them. The absorption in the active region is a function of the material quality and therefore also depends on the amount of impurities. The samples used within the work of this thesis have shown a slightly shifted emission spectrum compared to a pure $GaAs$ emission spectrum. This might indicate the presence of about 5% of Al in the active region. Non-

uniformity is a characteristic of epitaxial growth and occurs because of slight variations in the flux of materials in the growth chamber. The uniformity is a function of each chamber and with calibration processes a typical lateral variation in growth thickness of about 1% over a 2 inch wafer can be achieved. For all samples used in this project the tolerance in layer thickness was specified as 10 %. The most significant effect of this layer thickness variation is on the wavelength resonance of the microcavity determined by the individual thickness of the DBRs. A 1-10% variation in the thickness of the DBR layers has little effect on its characteristics because the layers are so thick and the stop band is reasonably large. However, a 1% variation in the thickness of the active region, L_c, or a change in refractive index due to additional Al concentration shifts the wavelength of the cavity resonance by 1% of the design wavelength. The effects of growth non-uniformity can be seen clearly in Figure (31). The Figure shows reflectivity graphs of different parts of wafer $QT1643A$. The position on the wafer is represented by two coordinates, the angle gives the direction on the wafer with the point of rotation at the center and 0^0 pointing along the (100) growth axis. The second number gives the distance from the center of the wafer in mm. On this wafer there is a shift of the microcavity resonance position of about 35 nm which represents a variation of almost 20% across 2 inches of wafer.

To provide laser light at around 1.55 μm an optical parametric oscillator (OPO) was used. The OPO was pumped by an 82 MHz modelocked Tsunami Ti–Sapphire laser. The OPO delivered 2 ps pulses at the same repetition rate as the Ti–Sapphire laser. By changing the cavity length of the OPO the output wavelength can be scanned from 1460–1580 nm. The basic experimental setup is shown in Figure (32).

The output beam of the OPO is passed through two variable neutral density filters and then focused onto the TPA device. For focusing the beam a ×20 microscope objective was used. The diameter of the collimated beam from the laser source
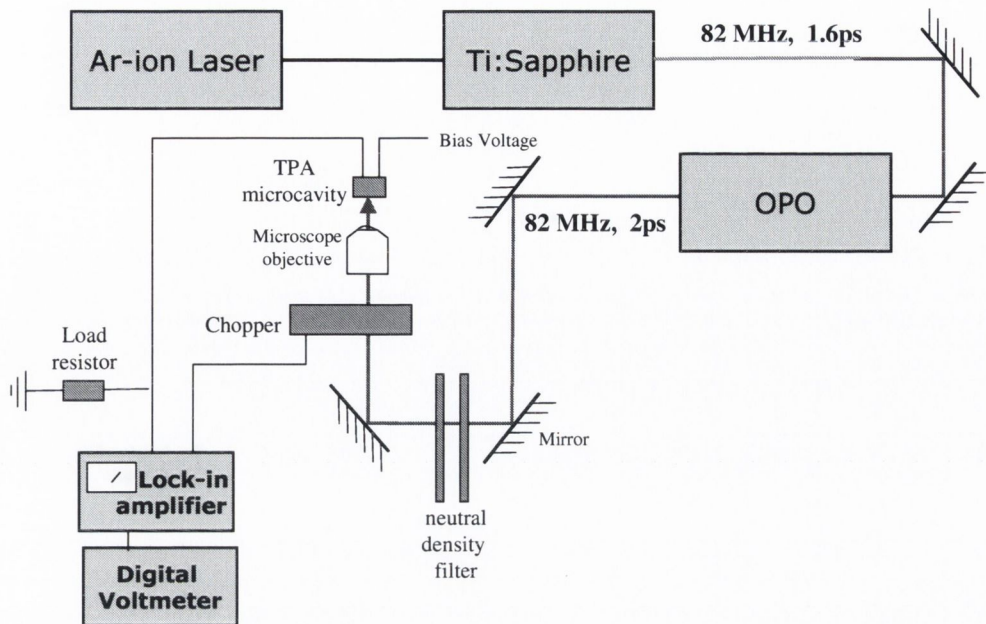
Figure 32: *Experimental setup used to characterise TPA devices.*

was 3.5 mm. Using the ×20 microscope objective the beam diameter at the focal spot was 5 μm. The TPA microcavity device was mounted on a xyz-stage to optimize the position of the device with respect to the focused light beam. A standard lock-in technique was used to measure the TPA-induced photocurrent of the device. The measured photocurrent was then recorded using a computer. Measurements of the spectral response of the TPA microcavity were made using the experimental setup presented in Figure (32). The TPA-induced photocurrent was measured while the wavelength of the OPO was varied across the cavity resonance. It is important that the average incident light power stays the same for different wavelengths. This was achieved by using neutral density filters. The spectral response of the TPA-induced photocurrent is shown in Figure (33) for a given incident average intensity of 0.1 mW.

Due to the nature of the microcavity design the cavity resonance response is dependent on the incident wavelength, with a cavity resonance of 1521 nm and a measured cavity linewidth of 5 nm (FWHM). Compared to the off-resonance
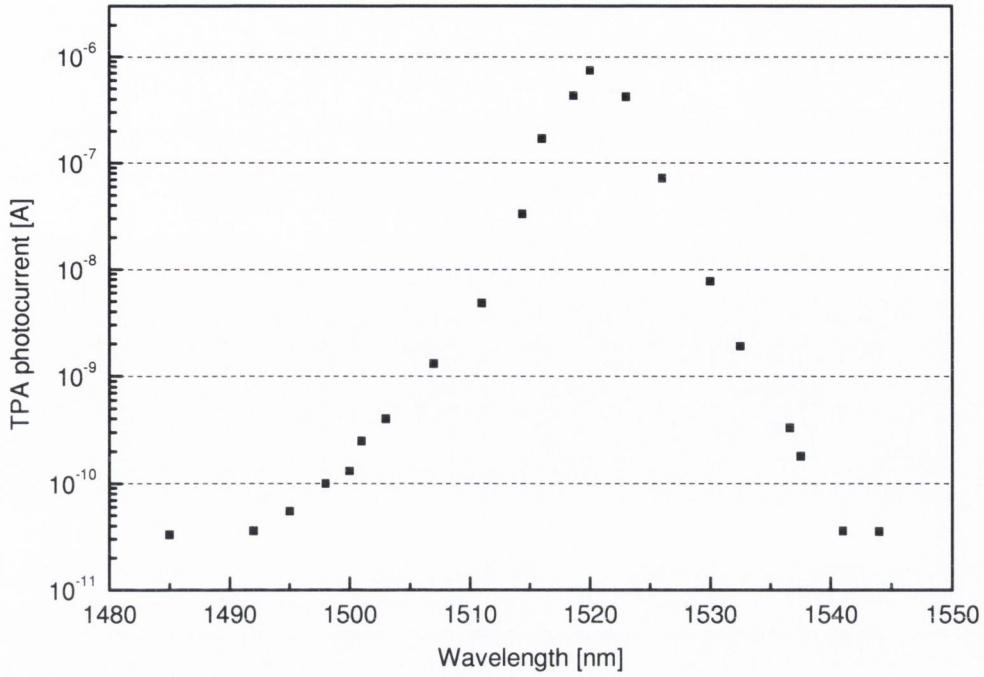
Figure 33: *Microcavity resonance. The TPA-induced photocurrent is measured as a function of wavelength of the incident light.*

TPA photocurrent response the created photocurrent at microcavity resonance varies by over four orders of magnitude. A similar comparison can be made by comparing the TPA induced photocurrent in a bulk semiconductor of the same material and dimensions as the active region embedded in the microcavity. Considering the surfaces of such a device to be antireflection coated the TPA–induced photocurrent using the same incident power would be four orders of magnitude smaller than achievable with the microcavity device on resonance. Assuming that condition

$$\frac{\alpha}{\beta} \leq I \leq \frac{1}{\beta L} \tag{87}$$

is satisfied, Equation (14) then becomes [102]

$$J = \frac{e A}{2 h \nu} \beta I_0^2 L \tag{88}$$

86

where A is the illuminated area on the semiconductor, L the length of the semi-conductor and β the TPA coefficient. In the experiment the spotsize at beam waist on the device was $6.7 \times 10^{-11} \, m^2$ for $\lambda = 1520 \, nm$. The TPA coefficient for $GaAs$ is $\beta = 0.03 \, \frac{cm}{MW}$ [103] and the average intensity was 0.1 mW, which corresponds to a peak power of 0.6 W. Assuming there is no reflection on the air-semiconductor interface and 100% of the incident light enters the 500 nm thick $GaAs$ slab, the created photocurrent would be $J = 7.8 \times 10^{-11} \, A$. Therefore, the photocurrent obtained at resonance of the TPA microcavity is four orders of magnitude larger than the value just calculated.

The next measurement was done with the same device from wafer QT1643A by measuring the photocurrent as a function of incident optical power close to the cavity resonance. As clearly shown in Figure (34) there is a square dependence of the photocurrent on the incident optical power, confirming the TPA response of the device. The incident optical power was varied by using neutral density filters in the beam path, as shown in Figure (32). The average power intensity was monitored by using a power meter with an integrating sphere for detection. In Figure (34) simulation results are also shown, where the TPA coefficient $\beta = 0.03$ cm/MW and a linear absorption of $\alpha = 0.01 \, cm^{-1}$ were assumed. This residual linear absorption is dominant at low intensities. For high intensities a saturation effect can be observed. As predicted earlier (Chapter (2)) the non-linear device response is found to range from 3×10^{-5} W to 1×10^{-2} W average power, for $\alpha = 0.01 \, cm^{-1}$. Within this dynamic range the TPA device can be used for autocorrelation and demultiplexing applications.

6.1.3 Dynamic Measurements

Microcavity enhanced TPA photodetectors should also find use in optical time division multiplexing (OTDM) systems. A key issue for demultiplexing is the device response determining the time interval required between sampling two
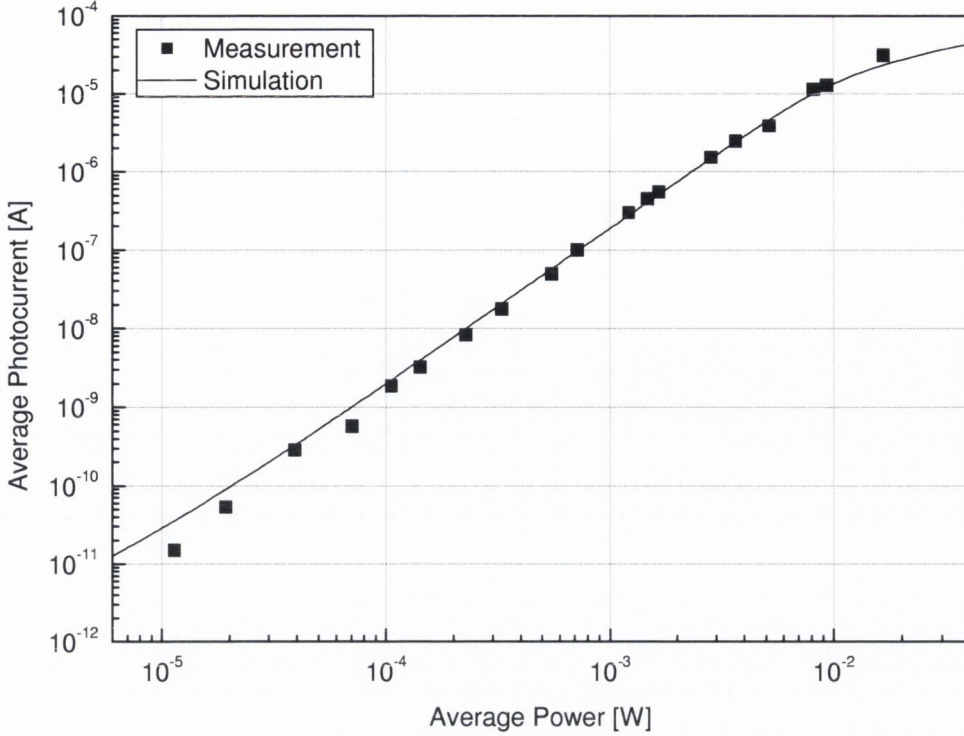
Figure 34: *Photocurrent as a function of incident optical power at 1550 nm. Full line gives simulation result for $\beta = 0.03$ cm/MW and $\alpha = 0.001$ cm^{-1}. The results show a quadratic dependence of the TPA photocurrent vs. average incident power.*

data bits. The electrical TPA microcavity device response was measured using a sampling-scope to detect the TPA generated photocurrent as a function of time. A schematic of the setup is shown in Figure (35).

Figure (36) shows the measured electrical response for an unbiased device, with an incident average power of 8.5 mW, at 1.5 μm and 2.0 ps pulsewidth. The aperture of the device was 25 μm. By measuring the decay time between 90% and 10% of the peak value an approximate bandwidth of 720 MHz can be extracted. Figure (37) compares the two electrical responses for an unbiased and a biased device. The reverse bias voltage applied is 7.5 V. Here a narrowing of the response peak can be observed. The change mainly happens due to a steeper fall of the trailing edge of the response peak. The time delay of 0.5 ns for the 90% to
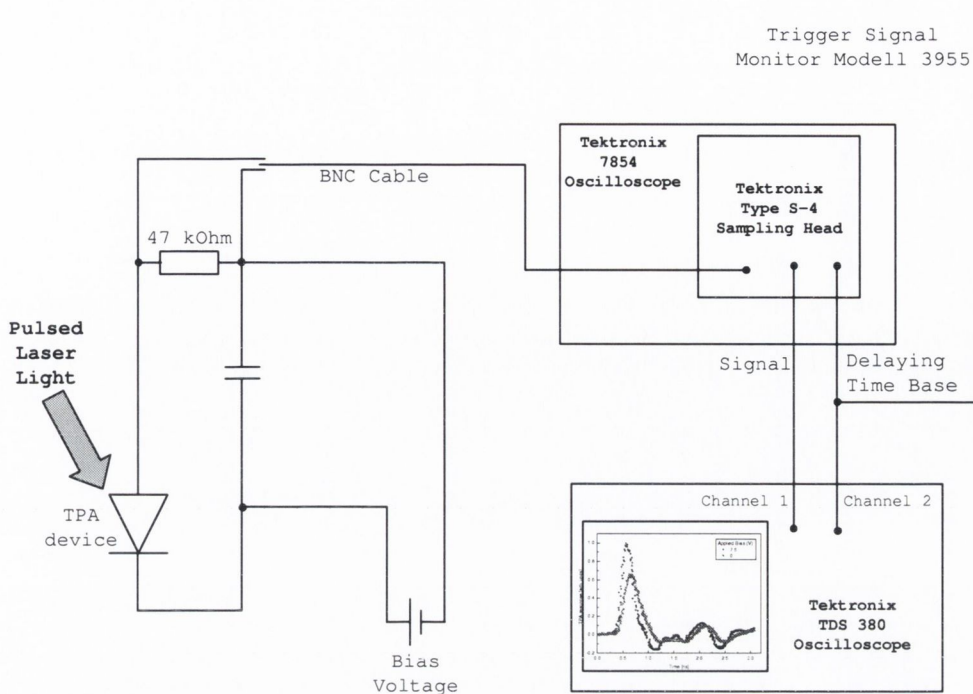
Figure 35: *Schematic of the setup used for the dynamic measurements.*

10% response decay on the trailing edge of the peak corresponds to a bandwidth of 2 GHz. Reverse bias leads to a widening of the depletion region layer which reduces the depletion capacitance associated with the p-i-n junction in the device. Since the device capacitance limits the response time of the device it is expected that devices with even smaller aperture give a higher bandwidth. The limit for the aperture size obviously is the diffraction limit of the light used. These devices have also not been impedance matched and optimized for electrical response and therefore significantly higher bandwidths can be expected by using high speed packaging for the devices.
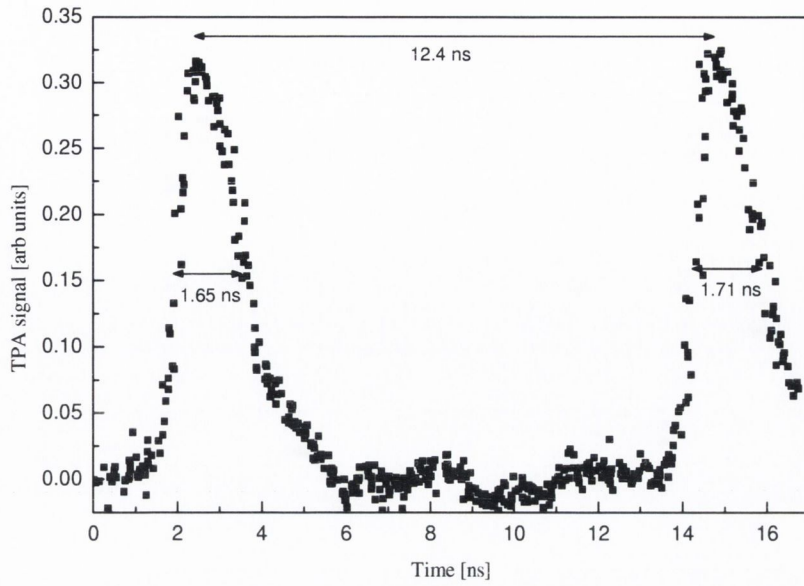
Figure 36: *Time response of an unbiased device to a 2.0 ps pulse, the bandwidth for the unbiased TPA microcavity device is ≈ 720 MHz. The device aperture is 100 μm.*
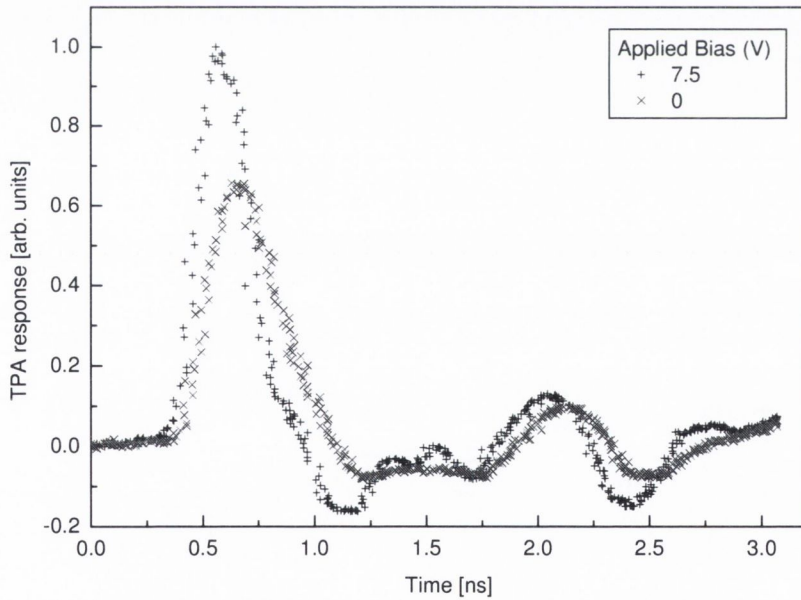
Figure 37: *Time response of an unbiased and 7.5 V reverse biased device to a 2.0 ps pulse, the bandwidth for the biased TPA microcavity device is 2 GHz. Here both devices have an aperture of 50 μm.*

6.2 Autocorrelation

6.2.1 Introduction

As a result of the non-linearity of the TPA process [104, 105, 106], the designed TPA microcavity device can be used as a photodetector in an autocorrelator for measuring the temporal pulse width of 1.5 μm optical pulses. For the autocorrelation measurement, a standard Michelson interferometer is used. In autocorrelation, the light signal under investigation is split into two beams. A delay line is used to vary the time between the two beams. The two light beams are then re-combined in space and time and are incident on the detector [107]. Apart from low cost and stability, one requirement for a pulse detector in optical communication systems is very high sensitivity. In optical communication systems the optical power at the receiver end is usually very low and the percentage of launched optical power available for pulse monitoring is generally quite small. Hence the optimization of detectors in terms of sensitivity is crucial. This section will present measurements and results to determine the sensitivity of a TPA microcavity photodetector [108]. Section (6.2.2) will present a short theoretical background on autocorrelation measurements. In Section (6.2.3) the measurement of the sensitivity of the proposed autocorrelation detector is described and compared to other detectors. Section (6.2.4) deals with polarization issues of the autocorrelation setup. A conclusion is presented in Section (6.2.5)

6.2.2 Theory

If the light intensity in each arm of the Michelson interferometer is equal, then the signal recorded by the photodetector, as a function of time is proportional to $\int |E_t^2|^2 dt$, where $E_t = E(t) + E(t - \tau)$ is the electric field of the light entering the photodetector. If the measurement is performed with interferometric accuracy, then the second harmonic recording is proportional to

$$
\begin{aligned}
I &= \int |\{E_0(t)e^{i(\omega t + \varphi)}) + E_0(t - \tau)e^{i(\omega(t-\tau) + \varphi(t-\tau))}\}^2|^2 dt \\
&= \int \{2E_0^4 + 4E_0^2(t)E_0^2(t - \tau) \\
&\quad + 4E_0(t)E_0(t - \tau)[E_0^2(t) + E_0^2(t - \tau)] \, cos[\omega\tau + \varphi(t) - \varphi(t - \tau)] \\
&\quad + 2E_0^2(t)E_0^2(t - \tau) \, cos2[\omega\tau + \varphi(t) - \varphi(t - \tau)]\} dt
\end{aligned}
\tag{89}
$$

where E_0 is the amplitude of the electric field and ω and φ are respectively the frequency and phase of the electric field. In real applications the measurement is not performed with interferometric accuracy and the interference fringes are averaged out. This is either due to low resolution or high scanning speed, or both. In Equation (89) the third and fourth term vanish if the bandwidth of the experiment is lower than the period of the *cos*-terms and the analytic expression for the recorded intensity is reduced to

$$
I = \int \{2E_0^4 + 4E_0^2(t)E_0^2(t - \tau)\} dt = 2\int I_0^2 dt + 4\int I_0(t)I_0(t - \tau) dt
\tag{90}
$$

Normalising Equation 90 yields the intensity autocorrelation of the pulse

$$
I_{norm} = 1 + \frac{2\int I_0(t)I_0(t - \tau) dt}{|\int I_0^2 dt|}
\tag{91}
$$

where I_0 is the pulse light intensity. The function given in Equation (91) has a peak to background ratio of 3:1. However, if the losses in the delay arm are

greater than in the fixed arm of the Michelson interferometer the contrast ratio will be reduced. Also, if the beams emerge from the arms with slightly different polarisation due to polarisation effects on the mirrors the peak-to-background value will be smaller. Implementation of the polarisation issue are discussed in Section (6.2.4).

Since the autocorrelation function is a symmetrical function, it does not provide any information about the symmetry of the light pulse it represents, to obtain the actual pulsewidth from the FWHM of the measured function a shape for the pulse must be assumed. Table (3) gives the relationship between pulse width, Δt_p, and the FWHM of the autocorrelation function, Δt_{ac}, for different pulse shapes. In general, interferometric autocorrelation can give information about the spectral distribution of the pulse or the chirp in the system [109], but since the microcavity filters frequencies according to the Lorentzian shaped cavity resonance, the interferometric autocorrelation will yield only information about the cavity spectrum [84].

Function	I(t)	$\Delta t_p / \Delta t_{AC}$
Diffraction Function	$I(t) = \frac{\sin^2 t / \Delta t_p}{(t / \Delta t_p)}$	0.751
Gaussian	$I(t) = exp\frac{-(4 \ln 2)t^2}{\Delta t_p^2}$	0.707
Hyperbolic Secant	$I(t) = sech^2 \frac{1.76 t}{\Delta t_p}$	0.648
Lorentzian	$I(t) = \frac{1}{1 + (4t^2 / \Delta t_p^2)}$	0.500

Table 3: *Second-order autocorrelation functions for different pulse shape models*

Source: User's Manual; Spectra-Physics-Lasers

Δt_{AC}: FWHM of autocorrelator function of the pulse

Δt_p: FWHM of intensity envelope of the pulse

6.2.3 Sensitivity

In order to investigate the sensitivity of the microcavity detector as a photodetector in an autocorrelation measurement a standard Michelson interferometer configuration has been used. The second harmonic crystal followed by a highly sensitive photodetector used in the conventional schemes was simply replaced by the two-photon absorption microcavity device. The experimental setup for the autocorrelation measurement is shown in Figure (38).
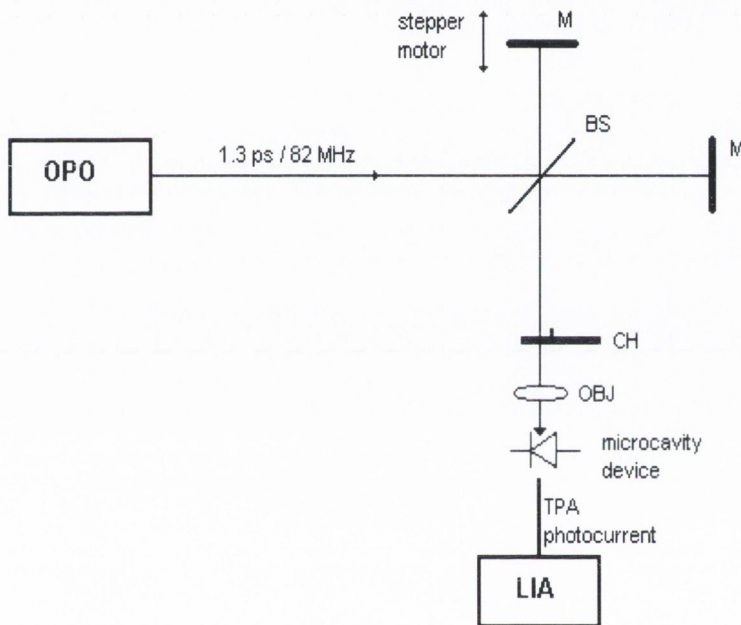
Figure 38: *Experimental setup of autocorrelation setup. BS: beam splitter, CH: chopper, M: mirror, OBJ: objective lens, LIA: lock-in amplifier, OPO: optical parametric oscillator.*

The optical pulses were generated by an optical parametric oscillator (OPO) synchronously pumped by a Ti:Sapphire laser system, at a repetition rate of 81.6 MHz. The temporal pulse shape was assumed to be Gaussian. At a wavelength of 1.5 μm the typical temporal pulsewidth was 1.3 ps. After traversing the two arms of the interferometer the two beams are colinearly focused to a

12 μm-diameter spot on the microcavity device using a $\times 10$ microscope objective (OBJ). The two-photon absorption photocurrent was measured using a lock-in technique. The best sensitivity is achieved when using the shunt resistance, $R_{SHUNT} = 1\ M\Omega$, of the microcavity device as the load resistor. The sensitivity of the TPA microcavity autocorrelator was measured by inserting neutral density filters in the beam path to control the signal-to-noise (SNR) levels. Figure (39) shows the microcavity device photocurrent as a function of delay for an incident average-power of 0.77 μW and peak-power of 3.6 mW. The quadratic response of the TPA photocurrent (versus incident average power) of the devices was verified down to an average power of 1 μW. Given the non-linear response of the photocurrent with incident power it is possible to extrapolate the incident power to a SNR of 1 [110].

The sensitivity of the autocorrelator defined as the product of the peak and average power of the minimum detectable signal (SNR=1) is found to be 9.3 $\times$ 10^{-4} $(mW)^2$ at a bandwidth of 1 Hz. For a given shunt-resistance, R_{SHUNT}, the limit for the detectable photocurrent is governed by the thermal noise

$$I_{th}^2 = \frac{4k\,T B_N}{R_{SHUNT}} \tag{92}$$

where k is the Boltzmann constant, T the temperature and $B_N = 1.6$ Hz the measurement bandwidth. Comparing the theoretical value of the thermal noise, $I_{th} = 0.16$ pA, with the standard deviation of the data in the side arms of the autocorrelation trace in Figure (39), $I_{th} = 0.1$ pA, good agreement was observed. The shunt resistor of the device is measured to be 1 $M\Omega$ and because of the smaller area of the device is less than that achievable with a typical waveguide device. To show the enhancement in sensitivity due to the microcavity, the autocorrelation measurement has also been performed at a wavelength of 1.46 μm, off the stop-band of the microcavity DBRs reflectivity spectrum. The magnitude of photocurrent measured off-band, $I_{TPA} = 220$ pA, is consistent with the theoretical values obtained by assuming TPA in bulk material with the same
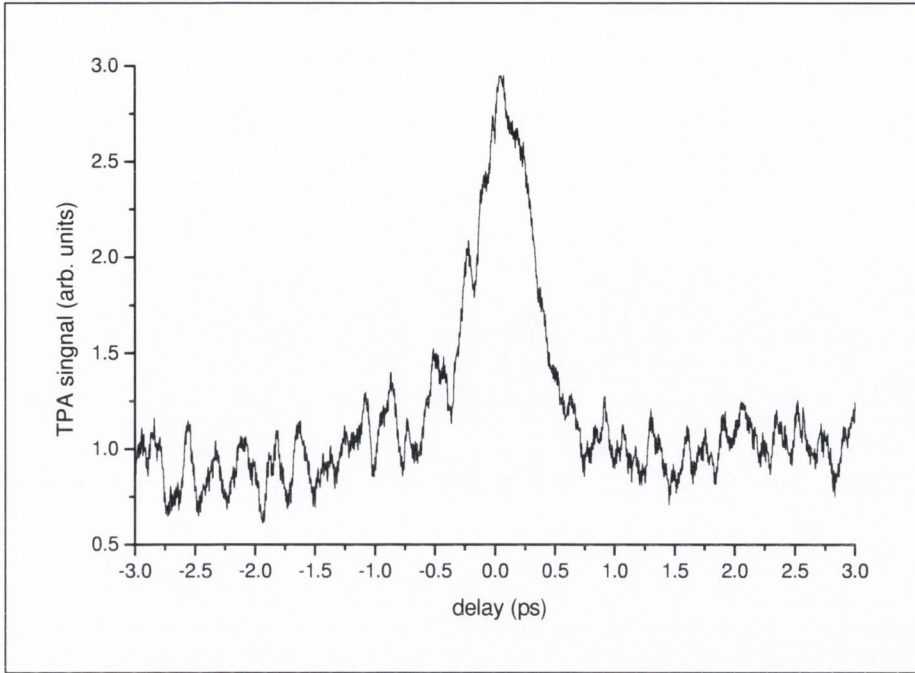
Figure 39: *Intensity autocorrelation of the laser pulse obtained with a Michelson interferometer and a TPA microcavity detector for average incident power of 0.77 μW. the peak to background ratio of the autocorrelation trace is 3:1.*

thickness as the active region of the microcavity device, given a TPA coefficient of $\beta = 3 \times 10^{-10}\,m/W$. A sensitivity of $1.5 \times 10^3\,(mW)^2$ is determined corresponding to an average-power of 330 μW and peak-power of 1.5 W. This sensitivity value is six orders of magnitude lower than achieved at cavity resonance.

6.2.4 Polarisation

Using the slightly different configuration as shown in Figure (40), a polariser was placed in each arm of the Michelson interferometer. In order to calibrate the two polarisers $P1$ and $P2$ before the measurement a third polariser was used and placed between the last beamsplitter (BS2) and the device. This polariser was later removed for the measurement. Looking at the TPA response of the micro-

cavity detector for each arm independently we were able to find the polarisation of each arm and determine the alignment for $P1$ and $P2$ for cross and co-parallel polarisation.
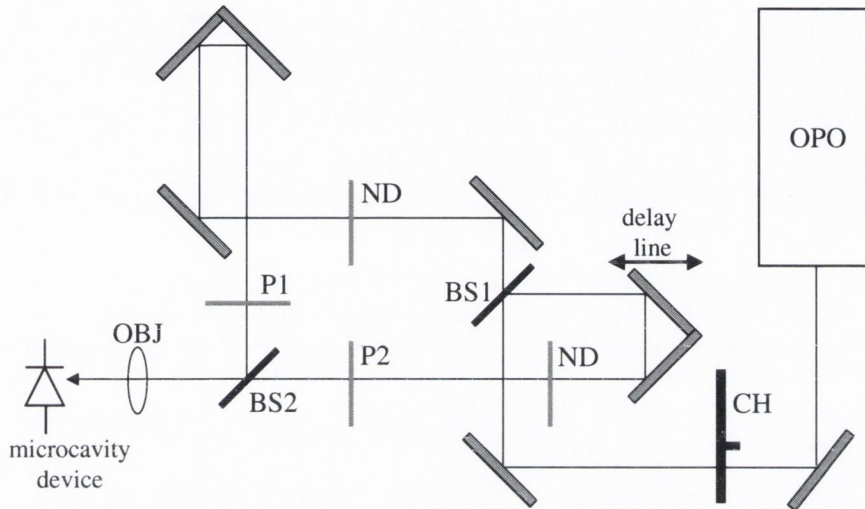
Figure 40: *Experimental setup of polarisation sensitive autocorrelation measurement. BS: beam splitter, CH: chopper, ND: neutral density filter, P: polariser, OBJ: objective lens, OPO: optical parametric oscillator.*

A long focal length lens has been used since the polarisers $P1$ and $P2$ for different polarisation settings introduced a small shift in the beam path. The polarisation of the light in each arm of the Michelson interferometer was changed by rotating the polarisers $P1$ and $P2$ around the optical axis. Due to small misalignment, the rotation of the polarisers resulted in a small angular deviation of the beam after the polariser. Using a 6 cm focal length lens gives a focal spot size larger than the device and beam alignment changes could be neglected in first order approximation. If the attenuation in each arm of the Michelson is equal, ignoring

the chopper and if the interference fringes are average out, the expression of the intensity autocorrelation of the pulse is given by

$$I_{sh} = 1 + \frac{2\int I_0(t)I_0(t-\tau)dt}{|\int I_0^2 dt|} \tag{93}$$

where I_0 is the light pulse intensity. Moreover if the autocorrelation is non-collinear, that is to say if the set-up is corresponding to cross polarisation, the equation is reduced to

$$I_{sh2} = 1 + \frac{\int I_0(t)I_0(t-\tau)dt}{|\int I_0^2 dt|} \tag{94}$$

Consequently it is expected to find different peak-to-background ratios for cross and co-parallel beam polarization. The maximum peak-to-background ratio for equal intensity beams of 3:1 was expected for co-parallel polarisation and the minimum peak-to-background ratio of 2:1 was expected for cross polarisation. The power in each arm was kept constant by using variable neutral density filter. The optical power in each arm was 60 μW, measured in front of the lens. Figure (41) and Figure (42) show the experimental results for cross- and co-parallel polarisation. The average peak-to-background ratio or co-parallel polarization was found to be 2.9 and the corresponding ratio for cross polarisation was 1.8. These experimental results fit the theoretically predicted values very well.
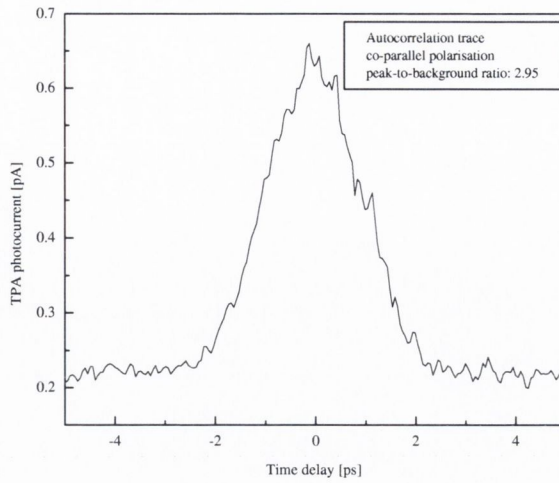
Figure 41: *Intensity autocorrelation trace. Light beams from both arms of the Michelson interferometer incident on the microcavity device are co-parallel polarised. The peak-to-background ratio of the autocorrelation trace is 2.95.*
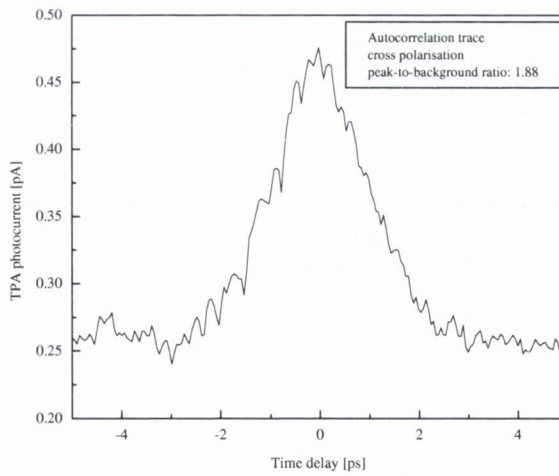
Figure 42: *Intensity autocorrelation trace. Light beams from both arms of the Michelson interferometer incident on the microcavity device are cross polarised. The peak-to-background ratio of the autocorrelation trace is 1.88.*

Figure (43) shows three autocorrelation traces taken for three different beam polarisation ratios. The TPA autocorrelation response of the microcavity detector is sensitive to the relative polarisation of the two incident beams. The co-parallel polarisation response is more efficient than the cross polarisation response. Because of symmetry reasons the device does not show any polarisation dependence for single beam TPA-induced photocurrent responses.
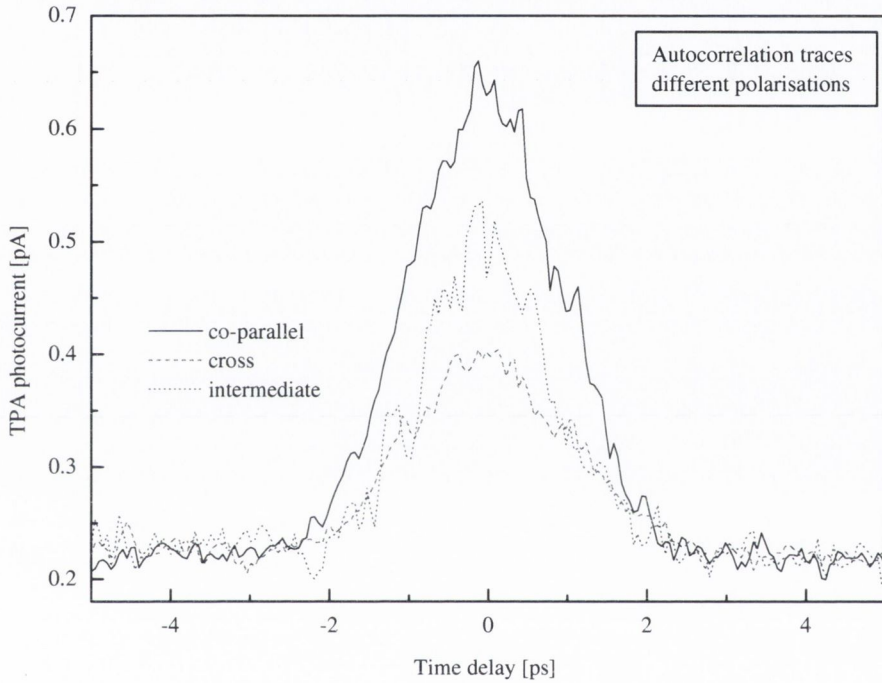
Figure 43: *Intensity autocorrelation traces of three different relative polarisation settings of the two beams incident on the microcavity device.*

The minor discrepancies between experimental data and predicted theoretical result are due to the use of a beam splitter (BS2) to combine the two beams before the microcavity detector. Whereas the polarisation of each arm is nearly linearly polarised after the polarisers $P1$ and $P2$, the polarisation after the beam splitter (BS2) becomes elliptically polarised. Also, assuming a Gaussian light distribution in the beam, small changes of the beam path due to the polarisers $P1$

and $P2$ will influence the absolute power on the microcavity detector depending on polarisation. Those small perturbations could be avoided by using different polarisers and a non-polarising cube beam splitter or adjusting the polarisation using $\frac{\lambda}{4}$ plates and monitoring the polarisation after the beamsplitter.

6.2.5 Conclusion

The sensitivity of the TPA microcavity autocorrelation measurements presented here compare very favourably with conventional autocorrelators based on second harmonic generation techniques which typically have a sensitivity of 1 $(mW)^2$ [111]. The sensitivity value is also higher than those reported using a silicon waveguide TPA autocorrelator at 1.5 μm, 1 $(mW)^2$ [53], and a silicon avalanche photodiode [52]. Compared to commercially available GaAsP photodiodes, Al-GaAs LEDs and GaAs LEDs recently used for TPA autocorrelation at 1.5 μm, the microcavity device is found to be more sensitive by at least a factor of 10 [55] at a bandwidth of 1 Hz. However, waveguide devices and photomultiplier tubes are still more sensitive due to a much longer active region [112]. For an InGaAsP diode a sensitivity of $0.15 \times 10^{-3}(mW)^2$ was stated [55] and for a GaAs photomultiplier tube, with length of 7.4 mm, a peak times average power sensitivity of $1.7 \times 10^{-4}(mW)^2$ at 1.5 μm was reported [113]. The bandwidth of the lock-in technique detection used in both these cases is not known.

For pulse monitoring applications, the polarisation orientation of the incident beams is important for maximum signal response. The highest TPA-induced photocurrent response is achieved for co–parallel beams. In a fiberised setup this can be accomplished by using polarisation control stages.

7 Off-axis Operation and Applications

The method of device simulation and approximations made in arriving at a designed structure have been outlined in Chapter (3) and (4). Device characterisation techniques for a proof-of-concept device working at 890 nm were shown in Chapter (5). In Chapter (6) the TPA microcavity concept was applied to a device working at 1.55 μm and the structure was fully characterised. In this chapter some of the requirements of the TPA microcavity and the trade-offs required for the device to be implemented in a telecommunication system are discussed.

7.1 Off-axis Operation

7.1.1 Introduction

As optical processing systems grow more demanding of modulators and detectors, requiring compact and dense interconnectivity, the susceptibility of such detectors to angular variations and misalignment becomes an important concern. Off-normal incidence or off focus beams may be an undesirable side effect which the system components have to cope with, or they may be an integral part of the way the system works. The effects of convergent beams on interference filters and Fabry-Pérot spectrometers have been extensively researched since the 1950's [114, 115]. Based on the transfer matrix approach, described in Chapter (3) Pidgeon and Smith arrive at an approximation which allows the off-axis behaviour of an etalon to be calculated. This approach, using an effective refractive index, has been used to fit the measurements of the TPA-induced photocurrent for angles up to 40° and this approach will be discussed below. It is a well known phenomenon that tilting a resonant cavity device will change the resonant wavelength, as the resonant conditions in the structure are only strictly satisfied for the normal component of the propagation wavevector [95, 116]. An analytic approximation of the TMM dealing with off axis behaviour of a TPA microcavity will also be presented in this chapter. This chapter looks at how the characteristics of a TPA microcavity designed for normal incidence operation is affected by

off-axis operation. The effects of off-normal incident beams on the microcavity resonance wavelength, the FWHM of the microcavity resonance and on the TPA photocurrent signal will be presented.

In Section (7.1.2) the experimental setup including important design considerations are described. Theoretical considerations for off-axis operations of microcavity structures are discussed in Section (7.1.3), and the results of characterization tests on the microcavities from wafer $QT1643(A)$ are presented in Section (7.1.4). These results are also compared with simulations of the TPA microcavity structure. In Section (7.1.5) a possible application of a tunable resonance wavelength TPA microcavity autocorrelator is presented.

7.1.2 Experimental Set-up

When setting up off-axis measurements it is important to maintain a constant distance from the sample to the focusing lens and keep the spot at the same point on the sample as it is rotated. This is especially important for samples which have low lateral uniformity or are very small, or both. An optimized setup would have the rotation axis of the sample mount, the optical axis and the device all at the same point in space. The microcavities under investigation, from wafer $Q1516R$ and $QT1643(A)$, showed really poor lateral uniformity over the area of the aperture of the device. The recorded photocurrent could therefore easily vary by up to 30% by illumination at different positions within the aperture of the TPA microcavity device. Due to technical difficulties and the low lateral uniformity of the device aperture it was decided to use a simpler setup and reoptimise the microcavity response after every change of incident angle. This was done by lateral realignment of the TPA device prior to every measurement. The laser beam is focused onto the sample, at normal incidence, by either a lens or a microscope objective. The TPA microcavity itself is mounted on a xyz-translation stage to allow for accurate lateral positioning of the single device and also for precise focusing of the incident beam. The xyz-stage again was mounted on a rotation stage. For the reflectivity measurements the light that is reflected by

the TPA microcavity is collected and collimated by a second microscope objective and finally detected by a Germanium photodetector. A Silicon filter in front of the photodetector was used to filter out ambient visible light. For better sensitivity the generated photocurrent from the Germanium photodetector was measured using a standard lock-in amplifier technique. For all other experiments in this chapter the TPA microcavity was mounted exactly the same way and the created TPA photocurrent was measured directly using a standard lock-in amplifier technique. The signal then was either read directly from the lock-in amplifier or by a computer.

The setup allowed the incident angle of the light to be varied on the device from minus to plus 45° with respect to normal incidence. The angle tuning was only performed in the $z - x$ plane and rotational symmetry around the growth axis of the device was assumed since no polarization issues were observed in previous studies, Section (6.2.4). The diameter of the incident beam was about 5 μm. The TPA microcavity device consists of $GaAs/AlAs$ and had a diameter of 100 μm. The $GaAs$ active region of the TPA microcavity was 458.9 nm thick and the mirror reflectivities of the top and bottom DBR were R_t=0.95 and R_b=0.986 respectively. The top mirror consists of 10 pairs of $\lambda_0/4$ $GaAs/AlAs$ layers and the bottom mirror of 18 pairs of $\lambda_0/4$ $GaAs/AlAs$ layers, where λ_0 is the cavity mode wavelength at normal incidence. The cavity resonance full width half maximum (FWHM) was 3.5 nm with a finesse of 96.

As a light source, a Ti-Sapphire pumped optical parametric oscillator (OPO) was used. The system was mode-locked at about 81.6 MHz and produced 2 ps pulses. The wavelength of the OPO is tunable from 1460 nm to 1560 nm. The laser system, under normal operating conditions, delivers about 80 mW of average power. However there is some optical loss in the experimental arrangement. Besides losses in any free space components (lenses, beamsplitters, chopper) the beam had to be coupled into a single mode fiber to ensure a high mode quality. In a single mode fibre only one mode is supported and transmitted due to the dimensions of the fibre core. Coupling a laser beam of poor mode quality into a

single mode fiber yields roughly 6 - 10 dB loss which means the power incident on the sample is considerably reduced. For this reason the high intensities required for the optical measurement were obtained by focusing the beam with a lens or microscope objective. Since a focused beam can be considered a cone of various incident angles, the focused beam response may be different from the case of a plane wave. It was experimentally verified that this did not produce a significant effect in these experiments as will be shown later. The lenses used did not have a numerical aperture (NA) greater than 0.45 and the focusing was not particularly tight in this setup as the diameter of the laser beam did not reach the aperture dimensions of the lens. Focused beam diameters of the order of 5 - 10 μm were used and these were measured with a set of calibrated pinholes by measuring the partial transmission of the beam through them. Minimum beam waist sizes at the focus for a Gaussian beam can also be estimated from the far field beam profile of the collimated beam incident on the lens but this method is not always accurate especially if the beam is not strictly Gaussian. But using a single mode fiber for better mode quality the focused beam diameters both measured and calculated agreed well. The formula used for the calculation of the focused beam diameter is

$$2w_0 = \frac{4\lambda}{\pi} \frac{F}{D}.$$ (95)

$2w_0$ is the beam waist diameter, λ the wavelength of the light, F the focal length of the lens and D the collimated beam diameter of the beam before the lens.

7.1.3 Theory

Figure (44) shows the calculated spectral reflectance of a 1.55 μm microcavity for different incident angles. The model used the mirror reflectivity of the front - and back-Bragg mirror as well as the thickness of the active region. The absorption within the structure was assumed to be zero. One important feature in Figure (44) is the micro-cavity resonance at 1.55 μm. For off-axis operation the resonance

shifts to lower wavelength. The argument here is the same as in chapter (4.8). The corresponding phase shift for an off-axis incident beam of $2m\pi$ shortens the roundtrip path of the light in the structure by $2nL\,cos(\theta_t)$ (Figure (22) on page 67).
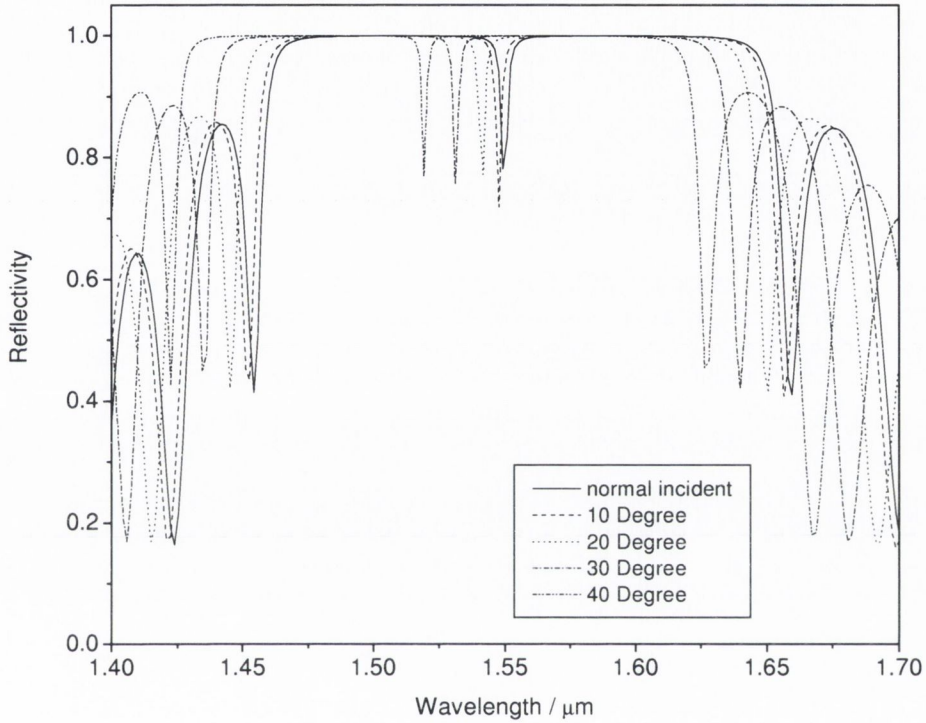
Figure 44: *Reflectivity of 1.55 μm micro-cavity with increasing incident angle. The stop band and the cavity resonance shift to lower wavelength with increasing incident angle. The micro-cavity consists of 10 pairs of Bragg front mirrors and 18 pairs of Bragg back mirrors. ($n_H = 3.374$, $n_L = 2.88$) The active region is GaAs with a thickness of 458.9 nm.*

In Figure (44) for small angles, the depth of the resonance seems to increase before finally dropping with increasing angle. That is only due to the limited number of points considered in the program. If for example the real normal incidence resonance lies between two points of the original data–set, the shift caused by taking a small angle into account moves the resonance position exactly onto a

data point and the new resonance might appear deeper. These changes, caused by the equidistant spacing of the data points, get smaller and finally negligible with increasing angle (the slope of $\sin(\theta)$ varies from a maximum at $\theta = 0^o$, to a minimum at $\theta = 90^o$.)

For the work presented here, only two-dimensional simulations were employed, although the basic device modelling approach is also suitable for three dimensional simulation.

Using the transfer matrix model (TMM) the reflection and transmission spectrum of our microcavity structure were analysed. The total phase shift ψ inside the cavity for one round trip is the important quantity which determines the resonance behaviour of the TPA cavity. The analytic expressions in this section are an approximation to the transfer matrix model for the cavity layout presented in Table (4). The analytic expression is used since it is more convenient to demonstrate than the TMM. This analytic treatment fits the results of the TMM very well for simple cavity structures. For a plane wave incident at angle θ onto the planar microcavity, the TPA inside the cavity can approximately be expressed as

$$A_{TPA} \approx \beta I_{in}^2 \varsigma_{TPA} \mathcal{F}^2 cos^2(\theta), \tag{96}$$

where β is the TPA coefficient, I_{in} is the intensity of the incident plane wave, ς_{TPA} is the TPA enhancement factor (Chapter (3.7)) for the plane wave with normal incidence with the wavelength equal to λ_0, the resonant cavity wavelength at normal incidence, and

$$\mathcal{F} = [1 + 2R(1-R)^{-2}[1 - cos(\psi)]]^{-1}, \tag{97}$$

where $R = (R_t R_b)^{1/2}$, $R_{t,b}$ is the reflectivity of the top/bottom quarter-wavelength Bragg mirror, and ψ is the total phase shift

$$\psi(\lambda, \theta) = \frac{4\pi L_c}{\lambda}\sqrt{n_c^2 - sin^2(\theta)} + \phi_t(\lambda, \theta) + \phi_b(\lambda, \theta), \tag{98}$$

107

where L_c and n_c are the active layer thickness and the active layer refractive index, respectively, λ is the incident wavelength on the device; $\phi_{t,b}$ is the phase shift of the front/back DBR. The factor $\mathcal{F}$ accounts for the resonance situation between the incident wave and the cavity. The equation $\psi(\lambda, 0) = 2m\pi$ determines the cavity mode wavelength at normal incidence, λ_0. It can be seen from Equation (96) that if the resonance conditions are always satisfied as the incident angle increases i.e. $\Delta\psi = 0$, the TPA will drop as $cos^2(\theta)$. As the incident wavelength deviates from λ_0 or the incident angle deviates from the normal incidence, we have the phase shift ψ deviating from $2m\pi$ by

$$\Delta\psi \approx -\frac{4\pi n_c L_c}{\lambda_0^2}\Delta\lambda - \frac{2\pi L_c}{\lambda_0 n_c}sin^2(\theta) + \Delta\phi_t + \Delta\phi_b, \qquad (99)$$

where the refractive index dispersion is neglected since the variation in the refractive index of $AlAs$ and $GaAs$ in the wavelength region considered is very small. The phase shift changes of the front and back DBR can be analytically expressed as

$$\Delta\phi_{t,b} \approx -\frac{4\pi D_{t,b}^{\lambda}}{\lambda_0^2}\Delta\lambda - \frac{2\pi D_{t,b}^{\theta}}{\lambda_0}sin^2(\theta), \qquad (100)$$

where $D_{t,b}^{\theta,\lambda}$ is in units of length and is determined by the DBR structure. In the approximation of the limiting case where the number of DBR mirror pairs goes to infinity $D_{t,b}^{\theta,\lambda}$ can be expressed as:

$$D_t^{\lambda} = D_b^{\lambda} = \frac{n_L \lambda_0}{4(n_H - n_L)}, \qquad (101)$$

$$D_t^{\theta} = D_b^{\theta} = \frac{\lambda_0}{4(n_H^2 - n_L^2)}\left(\frac{n_H}{n_L} + \frac{n_L^2}{n_H^2}\right), \qquad (102)$$

where the refractive index dispersion is also neglected, $n_{H,L}$ is the high/low refractive index of the composition material of the DBRs. Combining Equation (99) and Equation (100) yields

$$\Delta\psi \approx -\frac{4\pi(n_c L_c + D_t^\lambda + D_b^\lambda)}{\lambda_0^2}\Delta\lambda - \frac{2\pi(n_c^{-1}L_c + D_t^\theta + D_b^\theta)}{\lambda_0}sin^2(\theta)$$

$$\equiv -\frac{4\pi D^\lambda}{\lambda_0^2}\Delta\lambda - \frac{2\pi D^\theta}{\lambda_0}sin^2(\theta) \qquad (103)$$

The case $\Delta\psi = 0$ determines the modification of the cavity mode wavelength at the incidence angle of θ. According to Equation (103) the resonance wavelength change can be described as

$$\Delta\lambda = -\frac{D^\theta \lambda_0}{2D^\lambda}sin^2(\theta), \qquad (104)$$

which clearly shows that the modification of the cavity mode wavelength is proportional to $sin^2(\theta)$ and the larger the incidence angle the smaller the resonant wavelength. By rotating the TPA microcavity by an angle θ the resonant wavelength changes according to Equation (104).

For the factor $\mathcal{F}$ in Equation (96) the following approximation can be made by using Equation (104).

$$\mathcal{F} \approx [(1 - R)^2 + R\Delta\psi^2]^{-1}$$

$$= R\{\frac{(1 - R)^2}{R} + [\frac{4\pi D^\lambda}{\lambda_0^2}\Delta\lambda + \frac{2\pi D^\theta}{\lambda_0}sin^2(\theta)]^2\}^{-1}. \qquad (105)$$

It can be seen that $\mathcal{F}$ has a Lorentzian lineshape if $\Delta\lambda$ or $sin^2(\theta)$ is taken as the argument. If the normal incidence is kept but the incident wavelength varies, $\mathcal{F}$ as a function of λ has a FWHM of

$$\lambda_{FWHM} = \frac{1 - R}{\sqrt{R}}\frac{\lambda_0^2}{2\pi D^\lambda}, \qquad (106)$$

which is just the full width half maximum (FWHM) of the cavity reflection or transmission spectrum. The FWHM of the cavity resonance only slightly decreases as the incident angle increases.

109

If the incident wavelength is kept as λ_0 but the incident angle increases, $\mathcal{F}$ as a function of $sin^2(\theta)$ has an FWHM of

$$
\begin{aligned}
[sin^2(\theta)]_{FWHM} &= \frac{1-R}{\sqrt{R}} \frac{\lambda_0}{\pi D^\theta} \\
&= \frac{2D^\lambda}{D^\theta \lambda_0} \lambda_{FWHM}.
\end{aligned}
\tag{107}
$$

This dependence is shown in Figure (45) and (46). Figure (45) shows two different cavity reflection linewidth and Figure (46) shows the corresponding angular response of the cavity according to Equation (107). The TPA response decreases with increasing angle and the FWHM of the angular response of the TPA microcavity device for a constant wavelength λ_0 increases with increasing linewidth of the cavity reflection spectrum. The FWHM of the angular cavity response can be considered as the cavity acceptance angle.
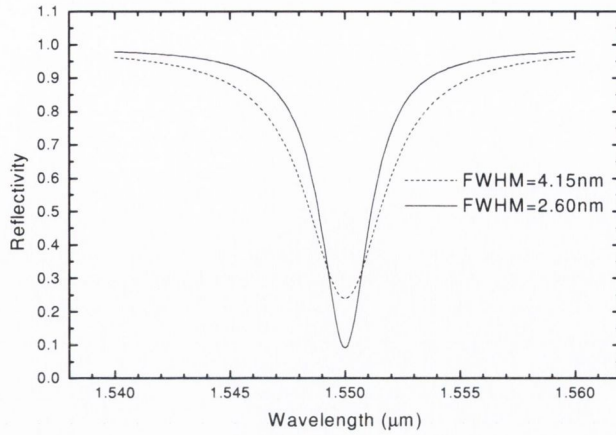
Figure 45: *Simulated reflectivity spectrum detail of a DBR microcavity mode. Simulations are done for two different microcavities, with 10/18 DBRs and 20/25 DBRs. Both simulations are Lorentzian with a FWHM of 2.60 nm and 4.15 nm, respectively.*
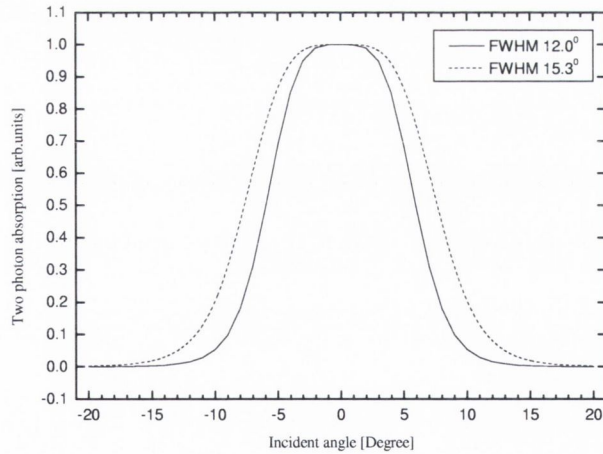
Figure 46: *The TPA microcavity response at a fixed resonance wavelength as a function of angle. The simulated results are for the two different microcavities in Figure (45). The FWHM of the acceptance angles are 12.0° and 15.3° respectively.*

The TPA inside the cavity is dependent on $\mathcal{F}$ squared, e.g. if $\mathcal{F}$ drops to $1/\sqrt{2}\mathcal{F}$, the corresponding width is just 64% of its original FWHM.

7.1.4 Off-axis Measurements

As an initial measurement, a reflectivity spectrum of the TPA device for different incident angles was recorded using the experimental setup described in Section (7.2). The wavelength incident on the microcavity device was scanned from 1460 nm to 1530 nm and the reflected light was collected with a large aperture microscope objective placed close to the sample. The collimated light collected by the microscope objective was incident onto a Germanium photodetector. The generated photocurrent from the Germanium photodetector was measured using a standard lock-in amplifier technique. The electrical signal from the photodetector for different angles is plotted as a function of wavelength in Figure (47). The signals for different angles are vertically spaced for better visibility. The photodetector response curve over this wavelength range is very flat and has therefore not been taken into account.

Initially the resonance wavelength of the TPA microcavity 1512 nm and this wavelength decreases with increasing angle. The reflectivity spectra for angles up to 7.5^o could not been measured due to the experimental layout. The microscope objective lens used to collect the reflected light would have blocked the incident light for angles smaller than 7.5^o. The width of the cavity resonance dip does not change by very much in the reflectivity measurement. This however is only due to a limited resolution of the measurement and changing factors like the fluctuation of the power output of the optical parametric oscillator. This problem might be solved with a computer controlled power monitor of the OPO output power or the use of a beamsplitter and a reference photodiode in the setup. Unfortunately, those options were not available in these experiments.

Figure (48) shows the resonant wavelength of the TPA microcavity as a function of incident angle. Also included in the graph are two theoretical fits using either
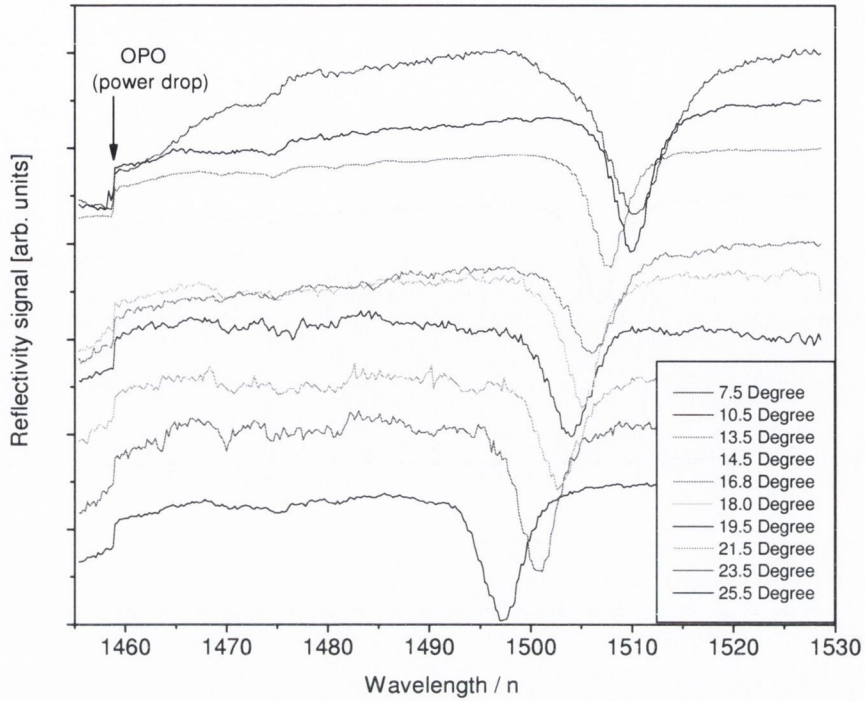
Figure 47: *Measured reflectivity spectra of microcavity for different inci-
dent angles. The spacing between the different plots in y-direction was
introduced for better clarity.*

the TMM or the Fabry-Pérot theory. The approximations made for the simpler
Fabry-Pérot theory are explained below. The resonant wavelength at normal
incidence for this TPA microcavity device was 1.512 μm. By rotating the TPA
microcavity by an angle θ the resonant wavelength changes, in accordance with
Equation (104). A schematic of the used setup is shown in Figure (49).

The experimental data in Figure (48) was taken by finding the maximum TPA
photocurrent response of the device for different incident angles θ by tuning the
OPO output wavelength. Using a variable neutral density filter the average power
incident on the device was kept constant. Small changes of the pulses in terms of
spectral width and time duration due to wavelength tuning have been neglected.
Both theoretical models give a close approximation to the experimental data.
The agreement between Equation (108) and the experimental results is excellent
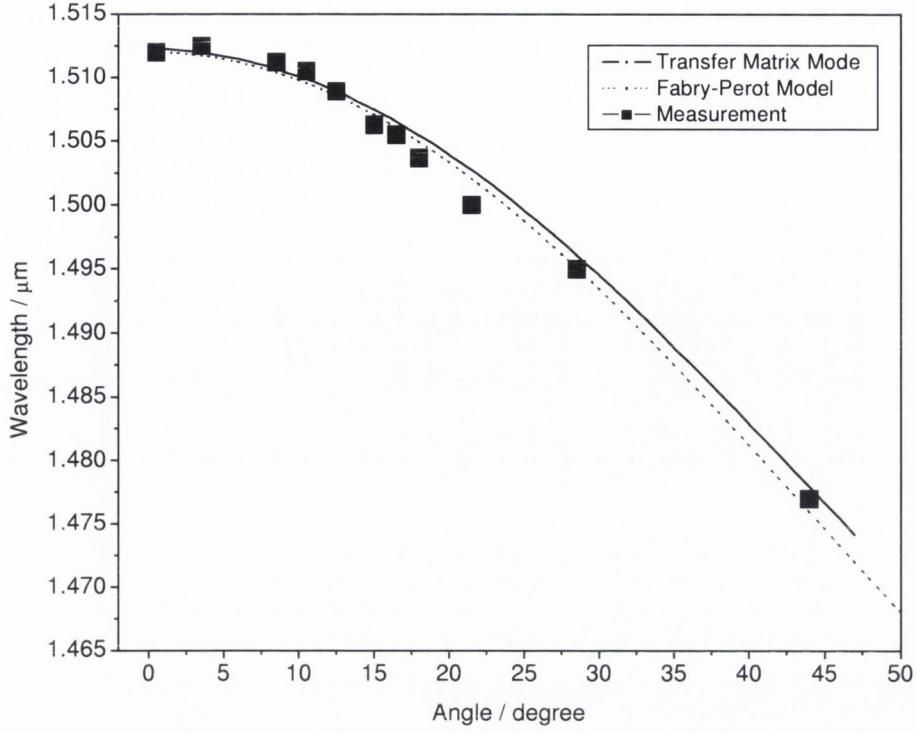
Figure 48: *Angular resolved cavity resonance. Simulation for QT1643A/xii, cavity resonance at normal incident is at 1.512 μm. Fabry-Pèrot-theory plot gives a fit according to equation* $\lambda = \lambda_0 \sqrt{\frac{\prime 1}{\lambda_0} \sqrt{(}} (n_0/n_{eff})^2 sin^2\theta)$. *The cavity simulation data fit is from a Transfer Matrix Model.*

for θ up to 45°.

For the Fabry-Perot fit Equation (108) was used.

$$\lambda = \lambda_0 \sqrt{(1 - (n_0/n_{eff})^2 sin^2\theta)} \qquad (108)$$

Equation (108) is an approximation of the angular dependence of an etalon and is valid for thin micro-cavities and small refractive index ratios within the micro-cavity. n_{eff} is a weighted average between the high and low index values of the mirror structure. This approach is valid when the actual cavity refractive index
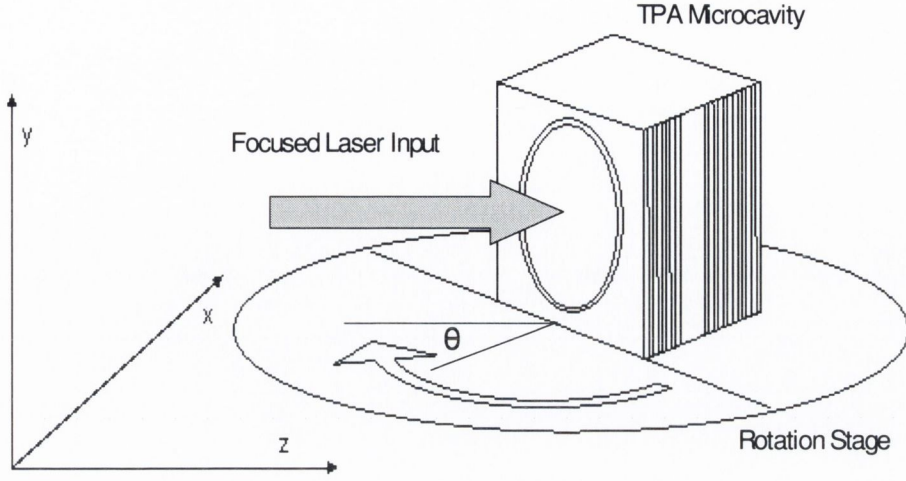
Figure 49: *The schematic drawing of the TPA microcavity with rotation stage.*

is approximately equal to that of one of the mirror layers (in our case: $n_C = n_H$). For such a high index cavity of order m, the effective index is given by [82]

$$n_{eff} = n_H \sqrt{\frac{m - (m-1)n_L/n_H}{(m-1) - (m-1)n_L/n_H + (n_H/n_L)}}. \qquad (109)$$

For a cavity order $m = 4$ and the refractive indices n_L and n_H equal to 2.885 and 3.375 respectively, the effective index for the TPA microcavity operating at 1550 nm is 3.19. As the order of the cavity increases, n_{eff} approaches n_H.

For small angles of incidence (i.e. less than $\sim 30^o$) the following approximation can be used [82]

$$cos(\theta_t) \approx \frac{1}{2}\left(\frac{n_i\theta_i}{n_{eff}}\right)^2 \qquad (110)$$

Here θ_i is given in radians. This approximation implies that high index cavities

115

are less sensitive to angular variations, because of the smaller internal angle.

The angular dependence of a TPA microcavity at a constant wavelength (normal incident operation wavelength) is depicted in Figure (50), for a 200 μm device. The resulting FWHM is $\sim 15.3^o$. The FWHM of the TPA response curve in Figure (50) for varying angle at a fixed wavelength, λ_0 at normal incidence, can be regarded as the acceptance angle of the microcavity. As shown previously in Section (7.1.3) the microcavity acceptance angle is proportional to the FWHM of the resonance linewidth of the cavity. Further discussion of the use of this effect is deferred to Section (7.2).
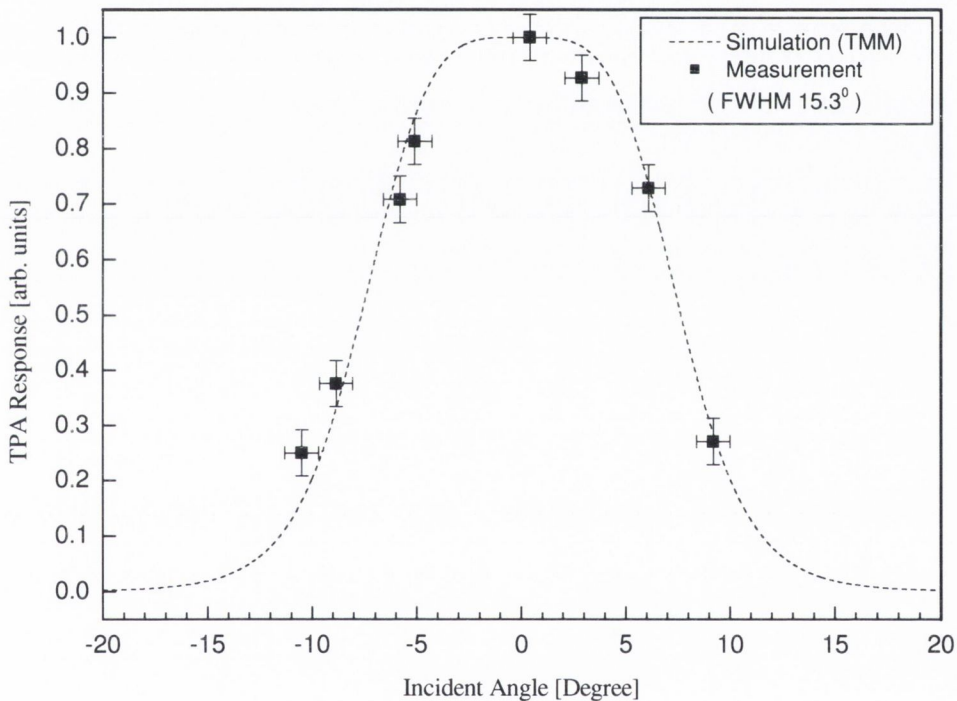
Figure 50: *Simulated and measured results for the TPA response at fixed resonance wavelength as a function of angle. If normally incident, the resonance wavelength is 1512 nm and the FWHM of the reflectivity spectrum is 4.05 nm.*

The experimentally measured Full-Width Half Maximum (FWHM) of the spectral

116

two-photon absorption photocurrent response, shown in Figure (51), does not change much with incident angle. The data fluctuations in Figure (51) do not show any trend and are most likely due to changes in alignment and the OPO output.
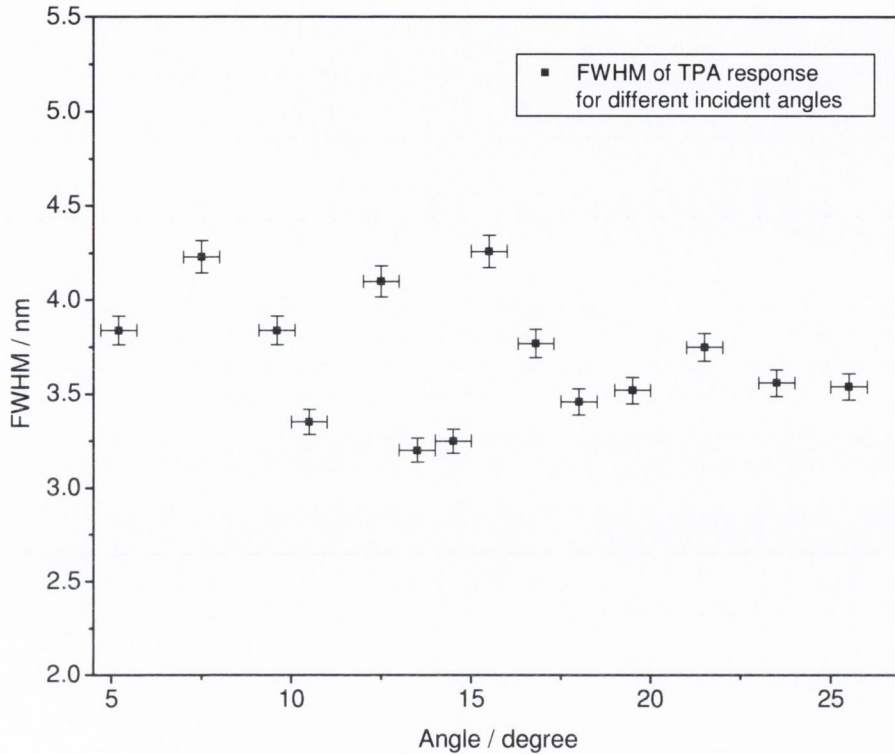
Figure 51: *Variation with angle of the Full-Width Half Maximum (FWHM) of the spectral two-photon absorption photocurrent response. The FWHM was obtained by fitting the spectral TPA photocurrent response with a Gaussian profile. Data is taken from different sets of measurements.*

However, Equation (106) indicates that the FWHM of the cavity resonance decreases slowly with increasing angle. In Figure (52), the theoretical linewidth of the cavity resonance is plotted as a function of incident angle. Since the theoretically predicted changes in the FWHM are very small for angles up to 45° the changes in the cavity resonance linewidth are within the experimental resolution.

This is mainly due to the wide spectrum of the laser pulses from the OPO. The spectral width of the laser light of about 4 nm blurs the actual resonance width of the cavity.
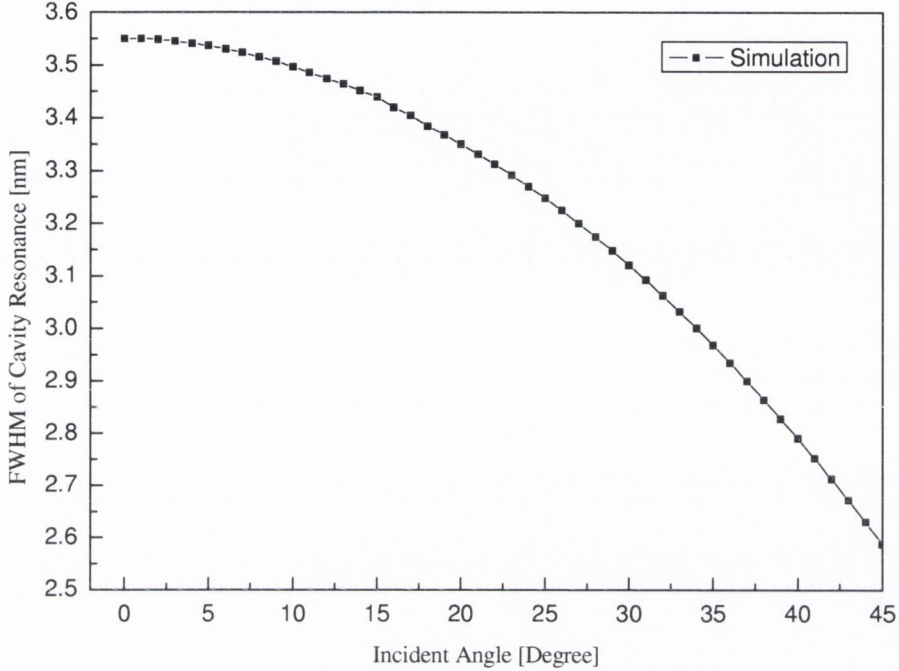
Figure 52: *Simulation results of the cavity resonance versus the incident angle.*

Using the TMM it can be shown that the maximum TPA response at resonance frequency for different incident angles is proportional to $cos^2(\theta)$. The TPA response at the cavity resonance frequency for an incident angle of 45° is half that of the TPA response at normal incident. Figure (53) gives the TPA response at cavity resonance for different incident angles.

The cavity resonance wavelength at normal incidence is 1566 nm for this device. This TPA microcavity was chosen since the tuning range of the OPO is limited in such a way that for lower wavelengths than ~1540 nm the output pulse spectrum of the OPO changes. This again leads to different output intensity and different coupling efficiencies into the single mode fiber. It has to be mentioned that the
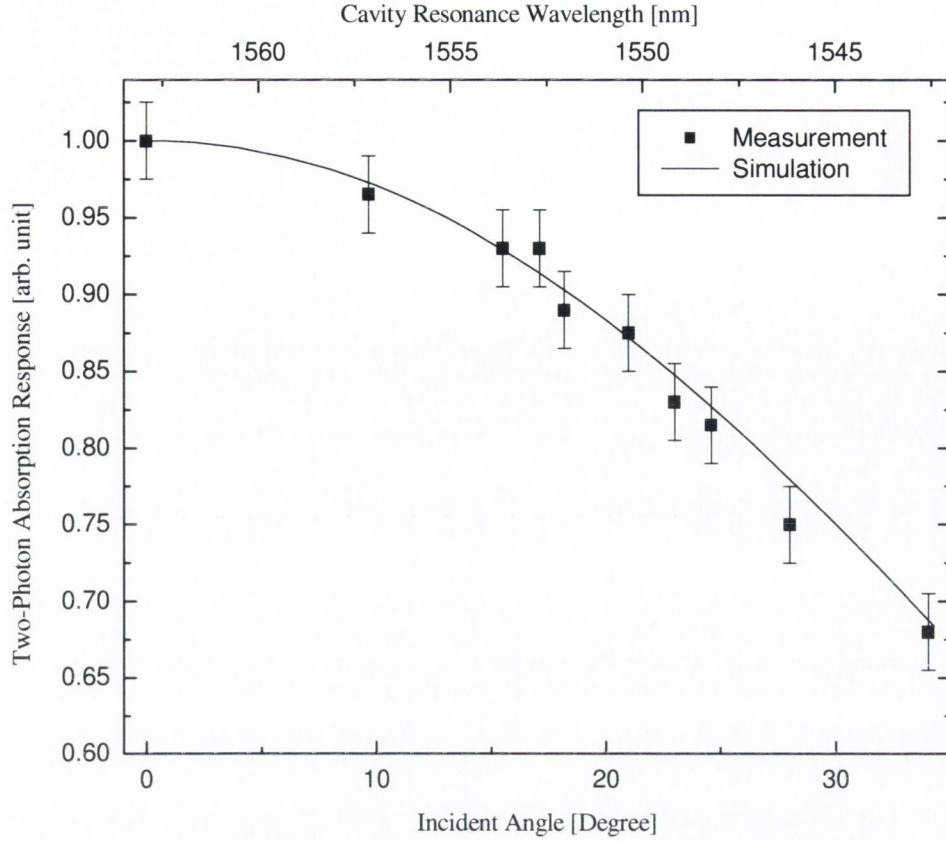
Figure 53: *The peak TPA response as a function of cavity resonance wavelength and incident angle. Cavity resonance at normal incidence is 1566 nm.*

reflectance of the beam from a dielectric surface and therefore also the transmission are a function of angle. The Fresnel equations [107] describe the fraction of the energy reflected or transmitted at a plane surface. It can be shown that for a beam incident in air on a high index medium such as GaAs the difference of the s and p polarization reflectance between 0° and 40° changes slightly, e.g. the s-reflectance increases by 30% and the p-reflectance decreases by 30%. The angular dependence of the reflectivity of a DBR at a constant wavelength however shows very little variation for angles up to 45° [107, 117]. The angle and polarization dependence of the energy coupled into the cavity were therefore neglected.

7.1.5   Tunable Autocorrelator

In the previous sections it has been shown that the presence of the DBR not only enhances the TPA but also allows for the microcavity resonance frequency to be tuned. Using the TPA microcavity as an autocorrelator as described in Chapter (6), it is now possible to change the resonance frequency of the microcavity by simply changing the incident angle of the light on the device. This change in resonance frequency of the autocorrelator can happen within a reasonable range to higher frequencies for a given maximum resonance wavelength at normal incidence. In addition, the fact that the device is thin means there are no phasematching problems compared with SHG crystals. This is due to the fact that only the relative polarization of the two beams on the sample is important (Section (6.2.4)) but not the over-all polarization orientation. Also, the TPA microcavity is optimized for 2 ps pulses. The enhancement of the TPA-induced photocurrent and the improved sensitivity enables the implementation of the TPA microcavity as a practical monitoring element in high-speed optical systems characterized by low peak power pulses [118]. Wavelength registration for each channel in a 160 Gbit/s DWDM system can be obtained by angle tuning the TPA microcavity. The vertical nature of the cavity structure is also superior for optical coupling.

As demonstrated in this chapter the setup allowed for the incident angle to be tuned from minus to plus 45° with respect to normal incidence. A tuning range of 35 nm is achieved by rotating the TPA microcavity over 45°. Angle tuning beyond 45° is possible but the rotation stage used was limited to 45°. A TPA microcavity with a normal incidence resonance at 1565 nm would therefore be able to scan over the entire C-band (1530–1565 nm [3]) for an angular range of 45°. In a 160 Gbit/s system, the 2 ps temporal pulse width will result in approximately 5 nm spectral spacing between channels to prevent crosstalk. Thus the microcavity structure would allow 7 channels to be monitored with the same detector. In a customized setup tuning over 60° would certainly be possible corresponding to a channel selection bandwidth of 55 nm. This would for instance allow for tuning

into the L-band beyond 1570 nm using a single detector. Again with a channel spacing of about 5 nm this would allow for approximately 11 channels with 2 ps pulses at 160 Gbit/s to be monitored. Figure (53) shows the dependence of the peak TPA response at the resonance wavelength on the tuning angle. The TPA response at cavity resonance frequency for an incident angle of 45° is half that of the TPA response at normal incident. This is expected from Equation (96) which indicates that if the resonance condition are always satisfied as the incident angle increases, i.e. $\Delta \psi = 0$, the TPA-induced photocurrent will drop as $cos^2(\theta)$. This drop in signal can easily be compensated for in an automated detection system.

7.1.6 Conclusion

In this section the practicality of a TPA microcavity structure for pulse characterization measurements at a range of wavelength has been demonstrated. This form of pulse monitoring technique lends itself to convenient experimental implementation in DWDM. Since TPA is a non-phasematched process, pulse characterization such as pulse monitoring and temporal measurements can be performed over a wide wavelength range with a single detector by simply exploiting the angular response of the microcavity.

7.2 Depth-of-Focus Scan

7.2.1 Introduction

The last section dealt with the susceptibility of a TPA microcavity detector to angular variations. This chapter concerns the susceptibility of such a detector to lateral misalignment. If the light has to be focused into the microcavity detector, misalignment considerations along the optical axis are important. For the investigation of this effect a setup similar to the conventional Z-scan has been used. In the conventional Z-scan, a Kerr medium is scanned along the z-axis in the back focal region of an external lens, and the far-field on-axis transmittance is monitored as a function of the scan distance z [119, 120]. In this case the Kerr medium can be regarded as a variable focal lens varying with distance z. The nonlinear refractive Kerr coefficient is directly obtained from a simple expression that relates it to the difference between the maximum and minimum normalized transmission. The idea for the depth-of-focus measurement is based on the Z-scan setup. But since there is no transmittance through the TPA microcavity due to the $GaAs$ substrate and packaging of the devices, the TPA-induced photocurrent is recorded as a function of distance z. This gives an indication of the susceptibility of the TPA detector to focus misalignment.

7.2.2 Theory and Analytic Model

Since the OPO output is launched into a single mode fiber before the light is used in a free space setup the following analysis has been done assuming a Gaussian TEM_{00} beam. The irradiance distribution of the Gaussian TEM_{00} beam is given by the following expression:

$$I(r) = I_0 e^{-2r^2/w^2} = \frac{2P}{\pi w^2} e^{-2r^2/w^2} \tag{111}$$

where P is the total optical power of the beam, r is the radius and w is a parameter usually called Gaussian beam radius, it is the radius at which the intensity has

decreased to $1/e^2$ of its peak value. The Gaussian beam radius is given by

$$w(z) = w_0 \left[1 + \left(\frac{\lambda z}{\pi w_0^2} \right)^2 \right]^{1/2} \qquad (112)$$

where z is the distance propagated from the plane where the wavefront is flat. λ is the wavelength of light, w_0 is the radius of the $1/e^2$ contour at a distance $z = 0$. Also defined is the wavefront radius

$$R(z) = z \left[1 + \left(\frac{\pi w_0^2}{\lambda z} \right)^2 \right] \qquad (113)$$

$R(z)$ is the radius of curvature of the beam after propagating a distance z. $R(z)$ is finite at $z = 0$, passes through a minimum at some finite z and rises again toward infinity as z further increased, asymptotically approaching the value of z itself.

The angle of incidence of a light ray on the microcavity is given by:

$$tan(\theta) = \left(\frac{s}{R(z)} \right) \qquad (114)$$

where s is the radial distance perpendicular to z. For calculating the absolute TPA response, a TPA efficiency factor is defined as follows

$$\eta = \left(\frac{eL}{2h \nu} \right) \beta \qquad (115)$$

according to [121]. Here L is the effective active region length (including cavity enhancement effect), e and h are the fundamental electron charge and Planck's constant respectively, ν is the light frequency and β the TPA absorption coefficient.

The FWHM of the microcavity acceptance angle profile has been defined in Equation (107)

$$
\begin{aligned}
[sin^2(\theta)]_{FWHM} &= \frac{1-R}{\sqrt{R}} \frac{\lambda_0}{\pi \, D^\theta} \\
&= \frac{2 \, D^\lambda}{D^\theta \lambda_0} \lambda_{FWHM}.
\end{aligned}
\tag{116}
$$
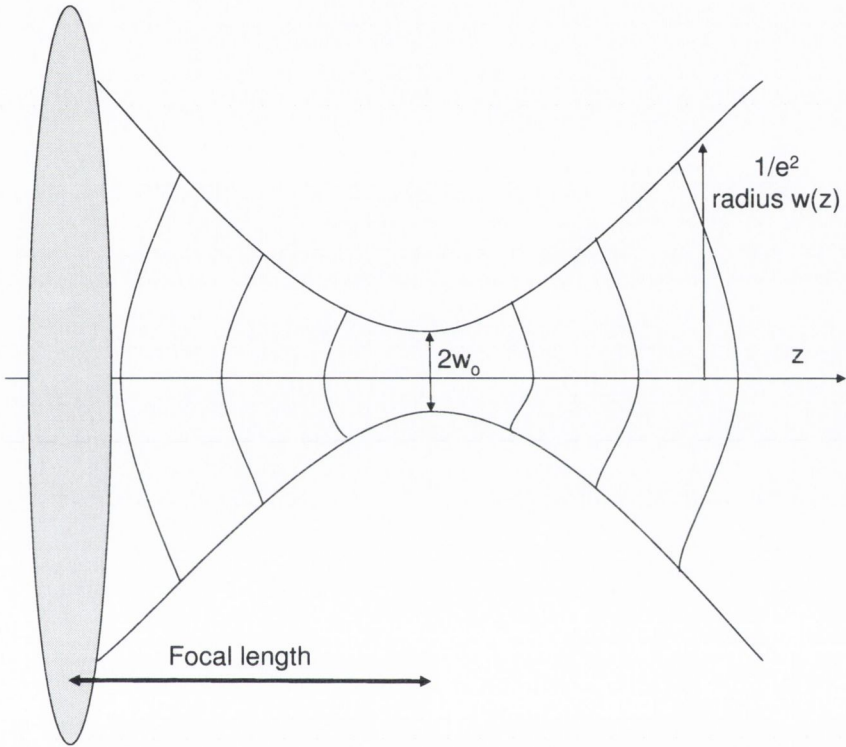
Figure 54: *Schematic of Gaussian beam optics.*

These are the starting expressions for the theoretical model. The general expression for the depth-of-focus scan could also be derived by solving Maxwell's equation for the problem. However, it is more useful and easier for this application to consider an approximate form of the situation which can be derived analytically. It has the advantage of allowing a simple and intuitive physical interpretation of the behaviour of the TPA microcavity response as a function of the z-translation along the depth-of-focus of a lens. Three assumptions are

being made. First, the device is considered to be a thin sample implying that the integrated light intensity is constant for the thickness of the sample. Second, the optical length of the cavity is to be neglected. Third, the mode divergence within the cavity is not taken into account. For the model itself, a *Labview* program was written. This program included Equation (111)-(116) and by choosing z and s as variable parameters the TPA-induced photocurrent response of the microcavity to a Gaussian beam focus could be calculated. The calculations were only done in two dimensions since the problem shows a rotational symmetry around the optical axis (z-axis).

The generated TPA photocurrent is a function of the angle of incidence θ of the ray on the microcavity, the radial distance s from the optical axis and the light intensity I. The intensity profile of the incident light is given by Equation (111). The angle of the incidence parameter is limited by the FWHM of the microcavity acceptance angle profile (Equation (107)). An integration over s, the radial distance, of the product of the intensity profile and TPA photocurrent leads to the total TPA photocurrent generated as a function of z,

$$J(z) = \int_{0}^{\infty} J(\theta(R(z), s)) I^2(w(z), s) \, 2\pi \, s \, ds. \tag{117}$$

7.2.3 Experimental Set-up

The experimental setup employed for the depth-of-focus measurement was similar to that used in Chapter (5). The microcavity device was mounted on a xyz–stage at the focal distance of a microscope objective that produced a 5 μm diameter excitation spot on the device. An OPO providing pulsed emission at $\lambda = 1.55 \, \mu m$ was used as the excitation source. The xyz–stage was mounted on a delay line along the beam axis, perpendicular to the device surface. The depth-of-focus setup used in this work is depicted in Figure (55). Modulating the beam using a chopper allowed lock-in amplification of the detected signal, greatly improving the signal to noise ratio especially for very low light intensities far outside the

focal point of the microscope objective.
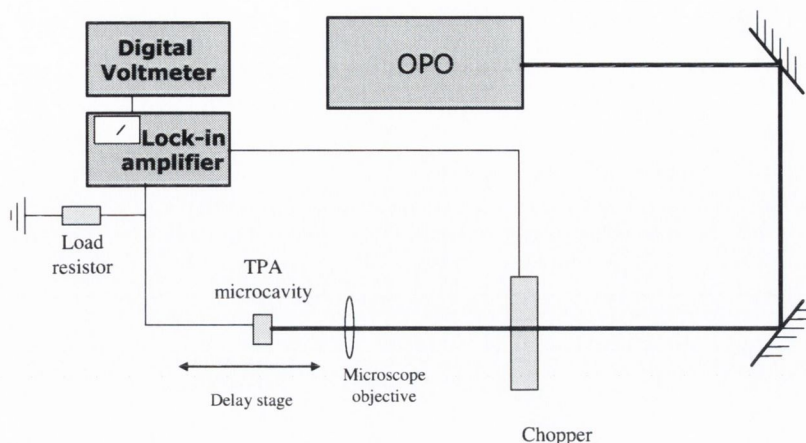
Figure 55: *Schematic of experimental setup for depth-of-focus measurement.*

7.2.4 Depth-of-Focus Measurement

Figure (56) shows the TPA response as a function of z-displacement. A $\times 20$ microscope objective was used to focus the laser beam to a measured spotsize of 5 μm diameter on the sample. The angle of the focused light cone is hereby 10° and therefore smaller than the acceptance angle of the microcavity, which was found to be 15.3^{o} in Section (7.1.4). The TPA-induced photocurrent response in Figure (56) is seen to rise and fall sharply around the focal point at $z = 0$. It may be noticed from the shape of the depth-of-focus scan that the experimental response curve appears to be asymmetric around the focal position $z = 0$. From the calculations outlined earlier in this chapter a theoretical response can be determined. The deviations of the measured data from the simulated TPA

photocurrent response are due to small misalignments of the sample on the delay stage and the given high non-uniformity of the microcavity aperture. A very small offset of the delay-stage axis with respect to the optical axis of the laser beam leads to a small movement of the light spot on the microcavity aperture while scanning the delay stage. These changes are however very small and a better alignment accuracy was not possible with this setup.
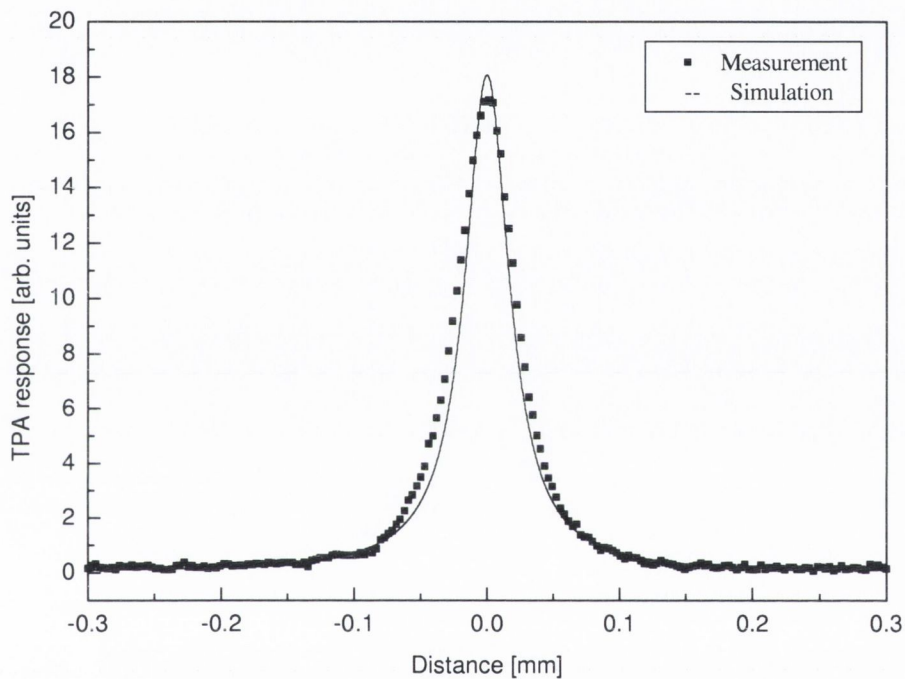
Figure 56: *Depth-of-focus measurement. Solid line shows simulated result obtained from analytical model.*

The FWHM of the depth-of-focus scan response is 45 μm. Keeping in mind that by misalignment of about $FWHM/2$ along the optical axis the TPA-induced photocurrent will drop by half, there is clearly a need for a method of accurately positioning the TPA microcavity at the focal point of the focusing lens for an optimum response.

7.3 Spectral Pulse Slicing

7.3.1 Introduction

The aim of this section is to investigate the potential of a TPA microcavity as a useful and practical device for chirp monitoring in optical systems. One aspect of this goal is to achieve sufficiently good optical performance in terms of spectral resolution to implement the devices in optical telecommunication networks. Device simulations and approximations are made for TPA microcavity devices from wafer $QT1643A$ and expected characteristics are shown. These simulations are compared with measurements taken on a 200 μm diameter TPA device from wafer $QT1643A$.

In any fiberised system the response of the system can cause changes in the shape of the propagating pulse [122], especially a broadening of the pulse accompanied by a progressive change in the frequency of the carrier through the pulse length called *chirping*. The considered chirp is linear and can be studied in the frequency domain rather than the time domain where it becomes apparent that the phase relationship between the harmonic components of the pulse is most important. The phase response as a function of angular frequency can be expressed as a Taylor series and the most important factors emerge as

$$
\begin{aligned}
\text{Group delay} &= -\frac{d\phi}{d\omega} \\
\text{Group delay dispersion} &= -\frac{d^2\phi}{d\omega^2} \\
\text{Third-order dispersion} &= -\frac{d^3\phi}{d\omega^3}
\end{aligned}
\tag{118}
$$

Here ϕ is the phase and ω the angular frequency. The group delay is considered to be unimportant in this case. It represents a delay in the arrival of the pulse but otherwise has no effect on the shape of the pulse spectrum. The group delay dispersion broadens and chirps the pulse. Third-order dispersion is more complicated and causes distortion in the pulse shape but is usually less of a

problem than group delay dispersion and is therefore here neglected.

7.3.2   Experimental Set-up

A schematic of the free space part of the experimental setup for spectral pulse slicing is shown in Figure (57).
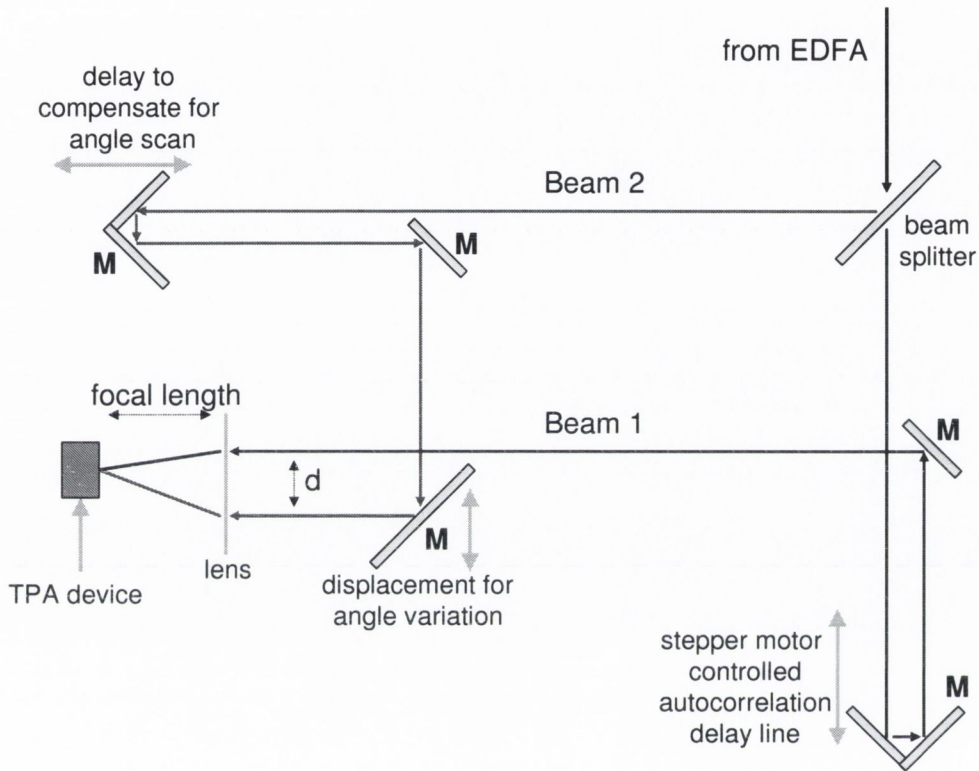
Figure 57: *Experimental arrangement for spectral slicing experiment.*
TPA device is at focal length from lens. M: mirrors

A fiber based ring laser is controlled by the 8 dBm signal output of a 10 GHz signal generator. At a variable pump current, mode-locked 10 MHz 500 fs-800 fs pulses are generated. The optical output of the laser is fiberised and connected to an erbium doped fiber amplifier (EDFA). Using the EDFA the signal is amplified and launched into the free-space setup using a collimating lens mounted on a micro positioning stage. The free-space setup consists of a 50/50 beamsplitter, one stepper motor controlled delay stage in one arm and a manual delay stage in the other arm. The free space setup is basically a Michelson interferometer

129

setup where the laser beam is split into two beams and after one beam has been temporally delayed the beams from both arms of the interferometer are recombined at the detector. Both beams are co-parallel while incident on the lens. The lens is an achromatic doublet lens with a diameter of 50 mm and a focal length of 70 mm. The achromatic doublet lens is used to minimize spherical and chromatic aberration. The TPA microcavity is positioned at the focal point of the lens. The TPA-induced photocurrent is detected using a standard lock-in amplifier technique. Using the manual delay stage in front of the lens the distance d between the two co-parallel beams can be varied. By changing the distance between the two parallel beams incident on the lens it is possible to vary the incident angle of the light on the TPA microcavity. In this experiment the beam coming from the motorized delay stage, referred to as Beam 1, is kept at a constant position at the lens whereas the position of the beam in the other arm, Beam 2, will be varied. The center wavelength of the fiber based ring laser is chosen to be coincidental with the microcavity resonance wavelength for the fixed incident angle of Beam 1. Changing the position of Beam 2 allows for the corresponding angle of incidence on the TPA microcavity to be varied from normal incidence to a maximum angle of 18°.

7.3.3 Theoretical Analysis

In this analysis, the following conditions were assumed: 1) the input pulse is the same as measured with the frequency resolved optical gating (FROG) setup [123, 124]; 2) there is no additional dispersion in the free-space part of the setup; 3) the spectral filter function (microcavity resonance) has a Lorentzian lineshape with a FWHM of 5 nm; 4) polarization issues are neglected and 5) the average power in both arms of the Michelson interferometer are equal. It is also assumed that the pulse is only spectrally filtered and the temporal pulse width stays constant. Using the angle dependence of the microcavity resonance wavelength it is possible to auto-correlate different spectral slices of the spectrum of the pulse under test. Keeping the reference beam at a fixed incident angle the incident

angle of the second beam of the Michelson interferometer can be changed. For different incident angle settings autocorrelation traces were calculated. This results in a series of auto-correlation traces for different spectral components of the pulse under test. The light intensity coupled into the microcavity depends on the intensity at the spectral component of the pulse under test at the filter function wavelength. The FWHM of the filter function averages the spectral response and determines the resolution. Plotting the maximum TPA autocorrelation response as a function of filter function wavelength contains information about the spectral shape of the pulse under test. The simulated TPA response shown in Figure (59) was calculated by using a simple $MATLAB$ program. The data of the frequency domain of the incident pulse has been imported into the program from a FROG measurement. The filter function was considered to be Lorentzian,

$$f = exp\left(-\frac{(\omega - \omega_0)^2}{4\,b}\right) \tag{119}$$

where ω is the frequency, ω_0 is the filter centre frequency and b determines the FWHM of the filter function. The filtering process can be expressed as a convolution of the spectrum of the pulse and the filter function in the frequency domain. The maximum intensity and the centre frequency shift are now dependent on the central frequency offset between the incident pulse and the filter function. For beam 1 the filter centre frequency coincides with the pulse centre frequency (by definition) and the other filter frequency is scanned. The correlation function of the two pulses has been calculated for different filter frequency wavelengths and the maximum response is plotted in Figure (59, dashed line) as a function of wavelength.

7.3.4 Experimental Results

The photocurrent versus wavelength response of the TPA sample from wafer $QT1643A$ is depicted in Figure (58).

The resonance wavelength of the TPA microcavity for normal incidence is 1559 nm.

131
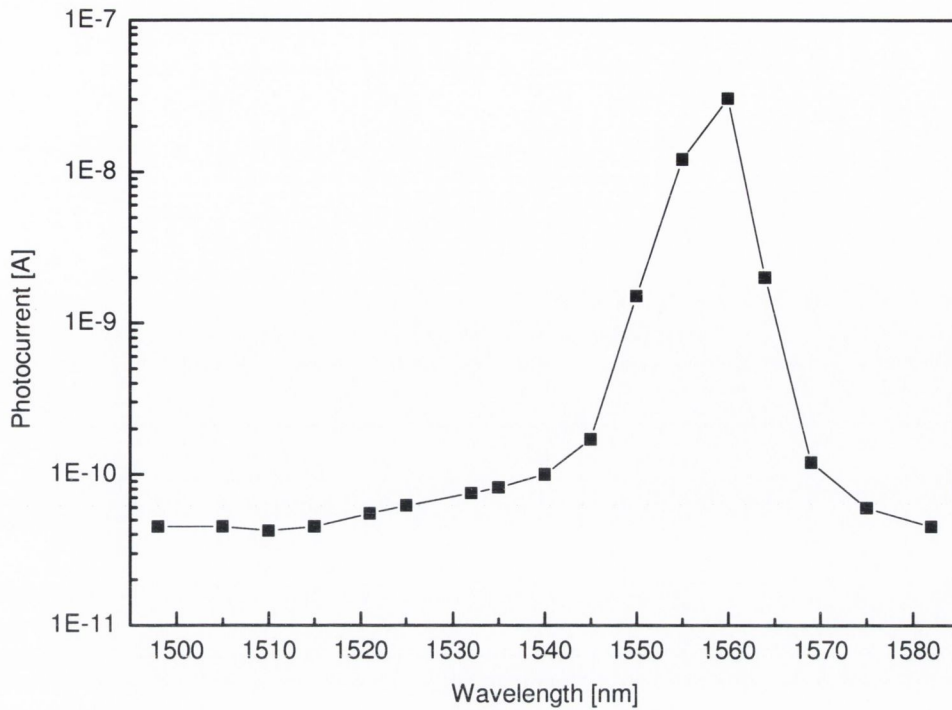
Figure 58: *TPA photocurrent against incident optical wavelength across microcavity resonance. Sample taken from wafer QT*1643*A.*

The FWHM of the photocurrent response is 5 nm. For a filter function with a FWHM of 5 nm the spectrum of the pulse under test had to be considerably broader to have sufficient resolution. A photocurrent measurement against incident optical power close to the cavity resonance was also carried out on the same sample. The results from this showed that there was a square dependence of the photocurrent against incident optical intensity over a dynamic range of almost 40 dB, evidencing the TPA process. The spectrum of the pulses from the fiber ring laser source was between 3 nm and 5.5 nm wide, depending on the pump current applied. Unfortunately the FROG setup for pulse characterization required very high input power (9–11 mW average power at 10 MHz/500 fs). An EDFA was used to amplify the signal. The amplification with the EDFA leads to amplified spontaneous emission and nonlinear effects in the fiber. These effects broadened the pulse spectrum to 10-13 nm. Also, since the FROG is working with SHG, polarization is an issue. The FROG measurement includes a polar-

ization control stage for phase matching, which is not included in the free-space setup. The angle dependent TPA microcavity response to three different pulse spectra was investigated. Figure (59) shows the pulse spectrum, the simulated TPA-detector response and the measured data for three different pulse spectra.

Figure 59: *FROG traces of pulse spectra. Experimental data and simulated results are shown.*

All response traces in Figure (59) are normalized for better comparison. Using the described setup it is possible to access the 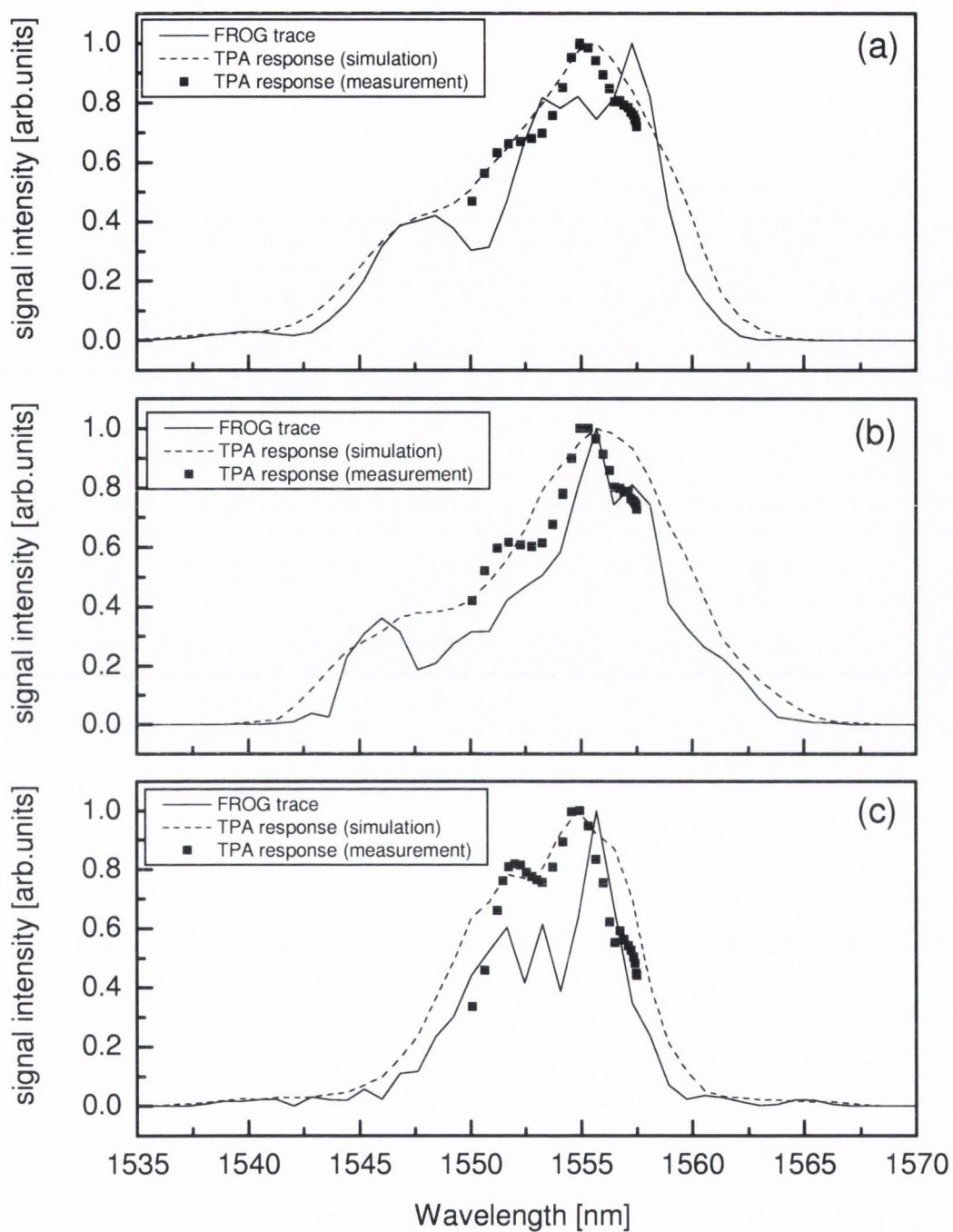spectral range 1550-1557 nm. The limit for this scan range is dictated by the clear aperture of the lens. Wider scanning ranges could be achieved by using a lens with larger diameter. The data points taken are equidistant in beam displacement d. According to Equation (104) the corresponding cavity resonance wavelength has been calculated. For the accessible wavelength range the measured TPA response shows good agreement with the simulation. The signal intensity peak on the short wavelength side in Figure (59c) seems to fit the predicted TPA response very well. Figure (60) shows the corresponding autocorrelation traces for all three pulses taken at the maximum response in Figure (59). Here both beams have the same incident angle on the TPA device. This incident angle of 9.5^o corresponds to a microcavity resonance wavelength of 1555 nm.

The three pulses used have been fully characterized using a commercial FROG setup. For retrieving the spectral and temporal pulse characteristics from the raw data measured with the FROG setup a specific software had to be used. It has been found that the accuracy of this program depends on the input intensity and the signal to background ratio of the raw data. The program also required different parameters for filtering the raw data before pulse reconstruction. The FWHM of the spectrum and pulsewidth were retrieved with the supplied software and are given in Table (5). The temporal FWHM measured with the TPA autocorrelation for the pulses (a) and (b) in Figure (60) are the same. Here the photon cavity lifetime dominates the autocorrelation width since the pulses are too short for useful autocorrelation measurements with the given TPA devices. The FWHM of the TPA autocorrelation trace (c) in (Figure (60)) is slightly larger ($\Delta\tau$= 1.2 ps) since the pulse width of 1.16 ps is comparable to the cavity photon lifetime.
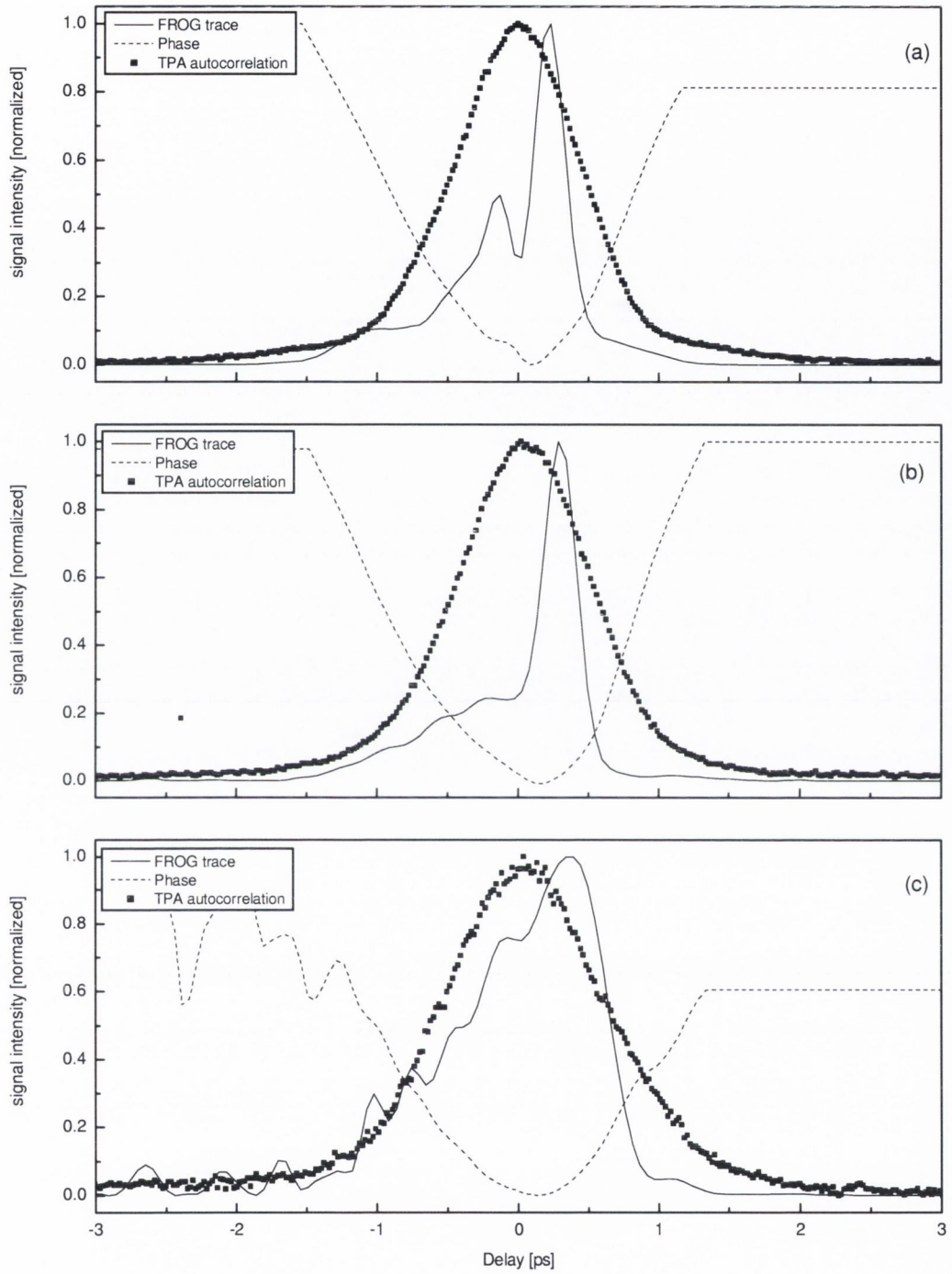
Figure 60: *Temporal FROG trace, Phase information and TPA autocorrelation trace for three pulses.*

Table 5: Temporal and spectral FWHM of pulses under test

Pulse	$\Delta\, ps$	$\Delta\, nm$
(a)	0.31	7.93
(b)	0.28	9.39
(c)	1.16	5.59

7.3.5 Discussion

In the structures initially considered with the spectral slicing approach, only limited pulse characteristic potential was observed. Ultimately it appears that this is due to the fact that the structure considered has a large FWHM resonance. Thus, the structure as designed already averages a significant fraction of the spectrum of the pulse under test and very low resolution is achieved. Also, using the available setup did not allow for independent *insitu* pulse characterization and part of the setup had to be moved from Dublin City University to Trinity College Dublin between measurement and pulse characterization. Since very high optical power had to be used for facilitating the FROG measurement the pulse will significantly change with fiber length and fiber alignment due to group velocity dispersion and self phase modulation. The use of an EDFA introduces amplified spontaneous emission which can be easily detected by the SHG in the FROG setup and shifts the reference background level and makes the determination of a FWHM of the pulse spectrum very unreliable.

It has been shown that the pulse characterization in the temporal and spectral domain is basically possible. In Figure (59) there is good agreement between the simulation results and the measured TPA response. Using microcavities designed

137

to have a narrower cavity resonance should give the desired higher resolution for spectral pulse characterization. The trade-off between spectral width of the cavity resonance and the photon cavity lifetime will probably not allow these devices to be used for autocorrelation measurements to determine the pulsewidth and pulse spectrum using a single device. These initial measurements however promise great potential for the use of TPA microcavities in *Sonogram* setups [125] and chirp monitors.

Knowing the broadening and chirp of a pulse, a series of coatings or a series of different refractive index layers can be designed to have an opposite group delay dispersion. Implementing this structure into the system and passage of the chirped pulse through that structure of refractive index layers then unchirps and shortens the pulse. Those devices are commonly known as dispersion correctors. A resonator, usually a single-cavity structure, placed on top of a reflector induces a delay in the harmonic waves at the resonant frequency compared with those off resonance. A maximum group delay occurs at the central frequency. The first and second derivatives of this group delay with respect to the angular frequency are then the group delay dispersion and third-order dispersion respectively. Adjustment of the parameters of the resonator has an effect on the magnitude and shape of the group delay curve. This type of corrector is more common in the telecommunications region where the pulse spectra are relatively narrow.

The other type of corrector, most common in the ultrafast region where the pulse spectrum is broad, is similar to a DBR stack but where the layers are tapered in thickness through the multilayers. This causes a progressive change in the group delay as the frequency changes and can be arranged to yield the desired second and third derivatives. Due to a limited range of adjustments to those structure layouts, namely thickness and refractive index change, the design is not easy. The materials usually used in the DBR stack are silicon and titanium-oxides.

7.3.6 Summary

The TPA microcavity used in this experiment was designed for 2 ps pulses. The spectral linewidth of the cavity resonance is therefore roughly 4 nm. To conduct spectral slicing of transform limited pico–second pulses, much smaller resolution in terms of resonance linewidth will be needed. This can be achieved by designing a microcavity with a resonance FWHM of about 1 nm. This cavity will then give better spectral slicing resolution but will not be optimized for the corresponding pulsewidth of a transform limited pulse. A microcavity with a spectral FWHM of 1 nm would be optimized in terms of cavity lifetime for 8 ps pulses.

8 Conclusion and Future Work

8.1 Conclusion

Some final remarks to summarise this work are now provided. Several experiments have been conducted to show the suitability of the TPA microcavity concept in optical pulse characterisation and all-optical sampling.

In Chapter (5) and (6) the optical and electrical properties of two TPA microcavitiy structures were investigated. It was found that the TPA photocurrent shows a non–linear quadratic dependence in term of the light intensity. This effect can be used in autocorrelation.

In Chapter (7) several applications of the TPA microcavity structure have been investigated. These include the use of the TPA microcavity in autocorrelation measurements or as a wavelength-selective detector. Since off-resonance wavelengths are rejected by the cavity, the TPA microcavity detectors have both wavelength selectivity and high speed response making them ideal for wavelength division multiplexing applications. However, the use of cavity enhanced structures will always require a trade-off between temporal and spectral resolution of the cavity.

8.2 Future Work

The work in this thesis has built upon previous work that experimentally demonstrated the TPA-induced photocurrent enhancement at 890 nm in semiconductor microcavities. In the work presented here, characteristics and dynamics of TPA microcavities have been outlined. By developing an understanding of the properties and design limitations it is hoped to use the implementation of these characteristics in possible device applications in optical network systems.

In this context, a number of interesting and unexplored avenues have been opened up for future work. The issue of microcavity design is one which is an ongoing process.

Consequently, the importance of understanding bandwidth limitations, such as

carrier diffusion times and charge trapping inside the device, is vital if the future demands that may be placed upon them in terms of optical demultiplexing and sampling are to be met. These demands may include switching rates of up to 40 GHz. Possibilities for optimisation in terms of bandwidth perfomance of the device include the introduction of graded heterojunctions, avoiding large band discontinuities in the design, the use of high speed packaging and the reduction of the device capacitance. There is also a need to demonstrate in a systems context that other materials used for building the reflectors of the cavity can perform as well as the current DBRs. Hybrid mirrors might reduce the capacitance of the device significantly and therefore increase the bandwidth.

8.2.1 Double Resonance Microcavity

For pump and probe experiments or the use of the microcavity as an optical switch between two different wavelengths a double resonance microcavity might prove interesting. Using a quantum well in the active region is one method of creating a double resonance within the stop-band of the microcavity [126, 127, 128, 129].

A different method of creating a double resonance in a microcavity is by choosing different resonance wavelengths for each Bragg mirror. This approach is purely intuitive and requires a long optimisation process. The stop bands of each mirror are separated by choosing different layer thicknesses. The resulting reflectance of the microcavity is then a constructive overlap of both reflectivity spectra. Figure (61) shows the microcavity reflectance, as calculated applying the TMM. The Bragg mirrors used each consist of quarter-wave layer pairs $(\frac{\lambda_0}{4})$. λ_0 for the front and back mirror was 1.43 μm and 1.6 μm respectively. The number of quarter-wave layers in front and back mirror were 25 and 34, respectively. The materials used are GaAs and AlAs. The two peaks are separated by $\sim$ 10nm.
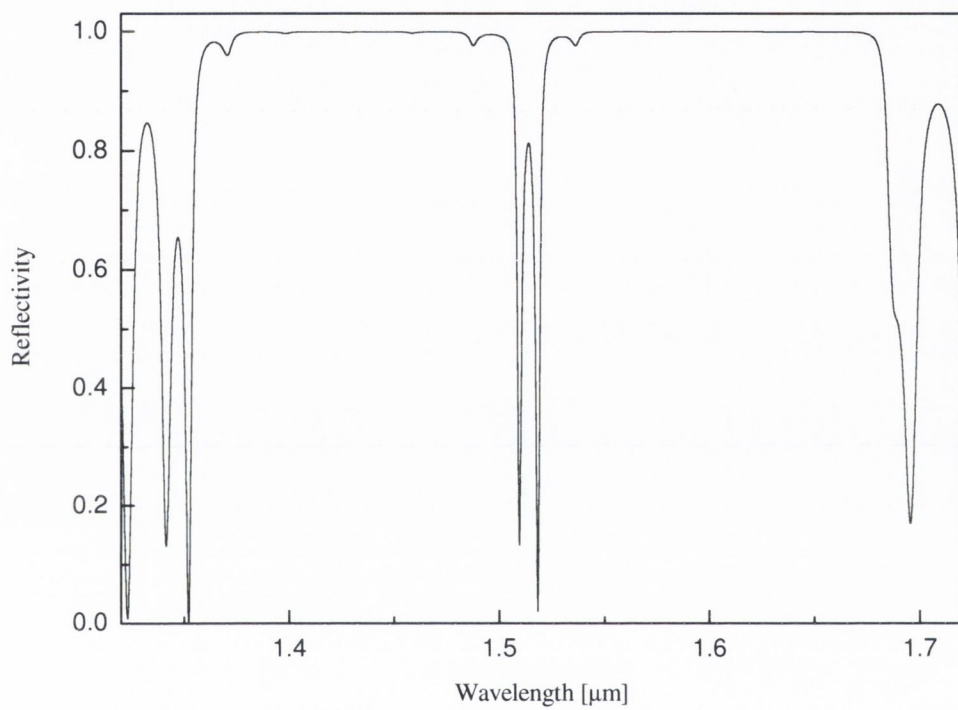
Figure 61: *The reflectivity of a λ-microcavity with two different DBRs. The two cavity modes at the center of the stop band are separated by ≈ 10 nm.*

142

8.2.2 Sampling experiments

Initial experiments in collaboration with the group led by Dr. Liam Barry in Dublin City University demonstrate that sampling of a 160Gb/s data signal should be possible [118]. The experiment shows the minimum temporal resolution of the system to be 2ps with the current cavity design. The experiment also demonstrates the sampling of two pulses separated by 7ps, corresponding to the sampling of a 160Gb/s signal.

References

[1] O.Krauss, "DWDM and optical networks: an introduction to terabit technology", Germany, Publicis, 2002

[2] M.Mellia, E.Leonardi, M.Feletig, R.Gaudino, F.Neri, "Exploiting OTDM technology in WDM networks", Proceedings - IEEE INFOCOM, Vol.3, 2002, pp.1822-1831

[3] D.W.Smith, "Optical network technology", London, Chapman & Hall, 1995

[4] J.G.Zhang, L.K.Chen, W.C.Kwong, "Experimental demonstration of efficient all-optical code-division multiplexing", Electronics Letters, Vol.34, No.19, Sep 17, 1998, pp.1866-1868

[5] A.Zeng, J.Chon, "Ultra-high capacity and high speed DWDM optical devices for telecom and datacom applications", Proceedings of SPIE - The International Society for Optical Engineering, Vol.4581, 2001, pp.13-20

[6] H.G.Weber et al, "High-speed optical signal processing and data transmission", 6th International Conference on Transparent Optical Networks, Vol.1, 2004, pp.177-181

[7] J.Leuthold, B.Mikkelsen, R.E.Behringer, G.Raybon, C.H.Joyner, P.A.Besse, "Novel 3R Regenerator Based on Semiconductor Optical Amplifier Delayed-Interference Configuration", IEEE Photon. Technol.Lett, Vol.13, No.8, August 2001, pp.860-863

[8] P.Perrier, S.Thompson, "Optical cross-connects: The newest element of the optical backbone network", Alcatel Telecommunications Review, No.3, Third Quarter, 2003, pp.195-201

[9] C.Schubert, J.Berger, S.Diez, H.J.Ehrke, R.Ludwig, U.Feiste, C.Schmidt, H.G.Weber, G.Toptchiyski, S.Randel, K.Petermann, "Comparison of interferometric all-optical switches for demultiplexing applications in high-speed

OTDM systems", Journal of Lightwave Technology, Vol.20, No.4, April 2002, pp.618-624

[10] A.K.Kar, "Organic materials for optical switching", Polymers for Advanced Technologies, Vol.11, No.8-12, August 2000, pp.553-559

[11] S.Tatsuura, T.Matsubara, M.Tian, H.Mitsu, I.Iwasa, Y.Sato, M.Furuki, "Ultrafast all-optical switching at 1.55 μm using an organic multilayer device", Appl.Phys.Lett., Vol.85, No.4, Jul 26, 2004, pp.540-542

[12] Physikalisch-Technische Bundesanstalt (PTB), Ultra-fast optical sampling oscilloscopes, www.ptb.de/en/org/4/45/453/oso_e.htm

[13] R.L.Jungerman, G.Lee, O.Buccafusca, Y.Kaneko, N.Itagaki, R.Shioda, "Optical Sampling Reveals Details of Very High Speed Fiber Systems", Agilent Technologies, www.agilent.com

[14] K.E.Zoiros, T.Houbavlis, M.Kalyvas, "Ultra-high speed all-optical shift registers and their applications in OTDM networks", Optical and Quantum Electronics, Vol.36, No.11, 2004, pp.1005-1053

[15] W.S.Vincent, L.H.Katherine, Eytan Modiano, K.A.Rauschenbach, "Architectures and Technologies for High-Speed Optical Data Networks", Journal of Lightwave Technol., Vol.16, No.12, December 1998

[16] D.Kilper, Personal Communication

[17] D.M.Spirit, A.D.Ellis and P.E.Barnsley, "Optical Time Division Multiplexing: systems, networks", IEEE Communications Magazine, Vol.32, No.12, 1994, pp.56-62

[18] G.Steinmeyer, "A review of ultrafast optics and optoelectronics", J.Opt.A: Pure Appl. Opt., Vol.5, 2003, R1-R15

[19] L.Barry, Personal Communication

[20] B.K.Mathason, H.Shi, I.Nitta, G.A.Alphonse, J.Abeles, J.C.Connolly and P.J.Delfyett, "Multiwavelength All-Optical TDM switching using a semiconductor optical amplifier in a loop mirror", IEEE Photonics Technology Letters, Vol.11, No.3, pp.331-333, 1999.

[21] Jeff Hecht, "OTDM promises higher communications speeds using optical processors", Laser Focus World, pp.121-124, November 2003.

[22] Dell'Oro Group 5-Year Forecast, Optical Transport Equipment Market Grows to USD 7.8 Billion by 2008, www.delloro.com/news/2004/opt080400.shtml

[23] S. Kawanishi, "Ultrahigh-Speed Optical Time-Division-Multiplexed Transmission Technology Based on Optical Signal Processing", IEEE Journal of Quantum Electronics, Vol.34, No.11, 1998, pp.2064-2079

[24] B.P.Nelson, N.J.Doran, "Optical sampling oscilloscope using nonlinear fibre loop mirror", Electron.Lett, Vol.27, No.3, January 1991, pp.204-205

[25] http://cp.literature.agilent.com/litweb/pdf/5988-4008EN.pdf

[26] AQ7750, http://www.yokogawa.com/tm/pdf/comm/aq7750/buaq7750e.pdf

[27] S.Diez, R.Ludwig and H.G.Weber, "Gain-Transparent SOA-Switch for High-Bitrate OTDM Add/Drop Multiplexing", IEEE Photonics Technology Letters, Vol.11, No.1, 1999, pp.60-62

[28] K.Deng, R.J.Runser, P.Toliver, P.R.Prucnal, "A highly scalable, rapidly-reconfigurable multicasting-capable, 100Gb/s photonic switched interconnect based upon OTDM technology", IEEE Journal of Lightwave Technology, Vol.18, No.12, 2000, pp.1892-1904

[29] S.Nakamura, Y.Ueno, K.Tajima , J.Sasaki, T.Sugimoto, T.Kato, T.Shimoda, M.Itoh, H.Hatakeyama, T.Tamanuki, T.Sasaki, "Demultiplexing of 168-Gb/s Data Pulses with a Hybrid-Integrated Symmetric Mach-Zehnder All-

Optical Switch", IEEE Photonics Technology Letters, Vol.12, No.4, 2000, pp.425-427

[30] L.P.Barry, P.J.Maguire, T.Krug, H.Folliot, M.Lynch, A.L.Bradley, J.F.Donegan, J.S.Roberts and G.Hill, "Design of micro-cavity semiconductor devices for highly efficient optical switching and sampling applications", IEEE Laser and Electro-Optic Annual Meeting 2002, Conference Proceedings, pp.839-840, Glasgow, 2002.

[31] T.Krug, M.Lynch, A.L.Bradley, J.F.Donegan, L.P.Barry, H.Folliot, J.S.Roberts, G.Hill, "High-sensitivity two-photon absorption microcavity autocorrelator", IEEE Photonics Technology Letters, Vol.16, No.6, 2004, pp.1543-1545

[32] P.J.Maguire, L.P.Barry, T.Krug, M.Lynch, A.L.Bradley, J.F.Donegan, H.Folliot, "Simulation of all optical demultiplexing utilizing TPA in semiconductor devices for high speed OTDM networks", submitted to Photonics Technology Letters

[33] P.J.Maguire, L.P.Barry, T.Krug, M.Lynch, A.L.Bradley, J.F.Donegan, H.Folliot, "Simulation of a High-Speed Demultiplexer based on Two-Photon Absorption in Semiconductor Devices", Optics Communications 249, 2005, pp.415-420

[34] C.C.Lee, Y.Fan, "Two-photon absorption with exciton effect for degenerate valence bands", Phys.Rev.B., Vol.9 No.8, pp.3502-3516, 1974

[35] J.H.Bechtel and W.L.Smith, "Two-photon absorption in semiconductors with picosecond laser pulses", Phys.Rev.B., Vol.13 No.8, pp.3515-3522, 1976

[36] A.Vaidyanathan et al., "Two-photon absorption in several direct-gap crystals", Phys.Rev.B., Vol.21 No.2, pp.743-748, 1980

[37] A.Vaidyanathan et al., "Two-photon absorption in several direct-gap crystals - an appendum", Phys.Rev.B., Vol.22 No.12, pp.6480-6483, 1980

147

[38] H.S.Brandi and C.B. De Araujo, "Multiphoton absorption coefficients in solids: a universal curve", Journ.of Physics C: Sol.State Physics, 16, pp.5929-5936, 1983

[39] B.S.Wherrett, "Scaling rules for multiphoton interband absorption in semiconductors", J.Opt.Soc. America B 1, pp.67-72, 1984

[40] H.N.Spector, "Two-photon absorption in semiconducting quantum well structures", Phys.rev.B.Condens.Matt., Vol.35, No.11, pp.5876, 1987

[41] A.Shimizu, "Excitonic optical nonlinearity of quantum well structures in a static electric field", Phys.Rev.B., Vol.37, No.14, p.8527, 1988

[42] A.Pasquarello and A. Quattropani, "Gauge-invariant two-photon absorption in quantum wells", Phys.Rev.B., Vol.38 No.9, pp.6206-6210, 1988

[43] A.Shimizu, "Optical nonlinearity induced by giant dipole momentum of Wannier excitons", Phys.Rev.Lett., 61(5), p.613, 1988

[44] D.Froehlich, R.Wille, W.Schlapp and G.Weimann, "Two-photon magnetoabsorption in multiple quantum wells", Phys.Rev.Lett., Vol.61, No.16, 1988, p.1878

[45] A.Shimizu, "Two-photon absorption in quantum well structures near half the direct bandgap", Phys.Rev.B., Vol.40, pp.1403-1406, 1989

[46] K.Tai, A.Mysyrowicz, R.J.Fisher, R.E.Slusher, A.Y.Cho, "Two-photon absorption spectroscopy in GaAs quantum wells", Phys.Rev.Lett., Vol.62 No.15, pp.1784-1787, 1989

[47] N.Nithisoontorn, K.Unterrainer, S.Michaelis, M.Sawaki, E.Gomik, "Two-photon absorption in GaAs/AlGaAs multiple quantum wells", Phys.Rev.Lett., Vol.62, pp.3078-3081, 1989

[48] I.M.Catalano, A.Cingolani, M.Lepore, R.Cingolani, K.Ploog, "Polarization dependence of the excitonic two-photon absorption spectra of GaAs/AlGaAs quantum wells", Sol.State Comm., 71(3), p.217, 1989

[49] A.Shimizu and K.Fujii, "Nonlinear optical properties of low-dimensional systems", Sol.State Phys., 24(11), p.846, 1989

[50] I.M.Catalano, A.Cingolani, M.Lepore, R.Cingolani, K.Ploog, "Observation of high index excitonic states in AlGaAs/AlAs ternary alloy quantum wells by two-photon spectroscopy", Phys.Rev.B.Condens.Matt., 41(18), p.12937, 1990

[51] Y.Takagi, "Simple autocorrelator for ultraviolet pulse width measurements based on the nonlinear photoelectric effect", Appl.Optics, Vol.33, No.27, pp.6328-6332, 1994

[52] K.Kikuchi, "Optical sampling system at 1.5 μm using two photon absorption in Si avalanche photodiode", Electron. Lett., Vol.34, No.13, pp.1354-1355, 1998

[53] T.K.Liang, H.K.Tsang, I.E.Day, J.Drake, A.P.Knights, M.Asghari, "Silicon waveguide two-photon absorption detector at 1.5 μm wavelength for autocorrelation measurements", Appl. Phys. Lett., Vol.81, No.7, pp.1323-1325, 2002

[54] B.C.Thomson, "Ultra-sensitive all-optical sampling at 1.5 μm using waveguide two-photon absorption", Electronic Letters, Vol.35, pp.1483-1484, 1999

[55] D.T.Reid, W.Sibbett, J.M.Dudley, L.P.Barry, B.Thomsen, J.D.Harvey, "Commercial semiconductor devices for two photon absorption autocorrelation of ultrashort light pulses", Engineering & Laboratory Notes, Suppl. To Optics & Photonics News, Vol.9, No.5, 1998

[56] H.Folliot, M.Lynch, A.L.Bradley, T.Krug, L.A.Dunbar, J.Hegarty, J.F.Donegan, L.Barry, "Two-photon-induced photoconductivity enhance-

ment in semiconductor microcavities: A theoretical investigation", J.Opt.Soc.Am. B, Vol.19, No.10, 2002

[57] M.Göppert-Mayer,"Über Elementarakte mit zwei Quantensprüngen", Naturwissenschaften, No.17, 932, 1929

[58] M.Göppert-Mayer, "Über Elementarakte mit zwei Quantensprüngen", Annalen der Physik, No.9, pp.273-294, 1931

[59] G.Breit, E.Teller, "Metastability of hydrogen and helium levels", Astrophysik Vol.91, p.215, 1940

[60] H.A.Bethe, E.E.Salpeter, "Quantum Mechanics of One- and Two-Electron Atoms", New York, pp.284-288

[61] M.Niering et al.,"Measurement of the hydrogen 1s-2s transition frequency by phase coherent comparison with a microwave cesium fountain clock" Phys.Rev.Lett., No.84, 2000, pp.5496-5499

[62] W.Denk, J.H.Strickler, W.W.Webb, "Two-photon laser scanning fluorescence microscopy", Science, 248, pp.73-76, 1990

[63] W.Kaiser, C.G.B.Garrett, "Two-photon excitation in $CaF_2 : Eu^{2+}$", Phys.Rev.Lett., No.7, 229, 1961

[64] T.H.Maiman, "Optical and microwave-optical experiments in ruby", Phys.Rev.Lett., Vol.4, 1960, pp.564-566

[65] P.A.Franken, A.E.Hill, C.W.Peters, G.Weinreich, "Generation of optical harmonics", Phys.Rev.Lett., No.7, 1961, pp.118-119

[66] M.D.Levenson, G.L.Eesley, "Polarization selective optical heterodyne detection for dramaticaly improved sensitivity in laser spectroscopy", Appl.Phys., Vol.19, No.1, May 1979, pp.1-17

[67] M.H.Weiler, "Nonparabolicity and exciton effects in two-photon absorption in zincblende semiconductor", Solid State Comm., Vol.39, No.8, 1981, pp.937-940

[68] Z.Zheng, A.M.Weiner, J.H.Marsh and M.M.Karkhanehchi, "Ultrafast optical thresholding based on two-photon absorption GaAs waveguide photodetectors", IEEE Photon.Technol.Lett., Vol.9, No.4, 1997, pp.493-496

[69] M.N.Islam et al., "Nonlinear spectroscopy near half-gap in bulk and quantum well GaAs/AlGaAs waveguides", Jour.Appl.Phys., Vol.71, No.4, 1992, pp.1927-1935

[70] L.V.Keldysh, "Ionization in the field of a strong electromagnetic wave", Sov.Phys.JETP, Vol.20, 1965, pp.1307-1314

[71] H.Folliot, Personal Communication

[72] C.C.Yang, A.Villeneuve, G.I.Stegeman, "Measurements of TPA coefficient and induced nonlinear refractive index in GaAs/AlGaAs multiqunatum well waveguide", Electron. Lett., Vol.29, pp.37-38, 1993

[73] C.C.Yang, A.Villeneuve, G.I.Stegeman, "Anisotropic TPA transitions in GaAs/AlGaAs waveguides", IEEE JQE, Vol.29 No.12, pp.2934-2939, 1993

[74] P.M.W.Skovgaard, R.J.Mullane, D.N.Nikogosyan, "Two-photon conductivity in semiconductor waveguide autocorrelators", Opt.Commun., 153, p.78-82, 1998

[75] Z.Knittl, "Optics of thin films: an optical multilayer theory", London, Wiley-Interscience, 1976

[76] H.E.Liddel, "Computer aided techniques for the design of multilayer filters", Hilger, Bristol, 1981

[77] S.D.Smith, "Design of multilayer filters by considering two effective interfaces", J.Opt.Soc.Am., 48, pp.43-50, 1958

[78] M.V.Klein, T.E.Furtak, "Optics", Chichester-Wiley, New York, 1986

[79] M.Born, E.Wolf, "Principles of optics : electromagnetic theory of propagation, interference and diffraction of light", Pergamon, 6th ed., 1980

[80] E.Hecht, "Optics", Addison-Wesley, Third Edition, 1998, pp.422

[81] F.L.Pedrotti, L.S. Pedrotti, "Introduction to Optics", ed.3, Prentice-Hall, London, 1987

[82] H.A.MacLeod, "Thin Film Optical Filters", (2nd ed.) Adam Hilger, Bristol, England, 1986

[83] H.Benisty, C.Weisbuch, V.M.Agranovich, "Physics and applications of microcavity light emitters", Physica E, Vol.2, No.1-4, July 1998, pp.909-914

[84] W.H.Guo, T.Krug, J.O'Dowd, M.Lynch, A.L.Bradley, J.F.Donegan, "Effect of cavity lifetime on two-photon absorption in high-finesse planar microcavities", submitted to Optics Letters

[85] Sadao Adachi, "Properties of Aluminum Gallium Arsenide", London, INSPEC, IEE, 1993

[86] M.A.Afromowitz, "Refractive index of $Ga_{1-x}Al_xAs$", Solid State Comm. Vol.15, 1974, p.59-63

[87] J.Buus, M.J Adams, "Phase and group indices for double heterostructure lasers", IEE J.Solid-State Electron. Dev.,UK, Vol.3, pp.189-195, 1979

[88] S.Gehrsitz, F.K.Reinhart, C.Gourgon, N.Herres, A.Vonlanthen, H.Sigg, "The refractive index of $Al_xGa_{1-x}As$ below the band gap: accurate determination and empirical modeling", J. of Appl. Physics Vol.87 No.11, 2000, pp.7825-7837

[89] M.H.MacDougal, H.Zhao, P.D.Dapkus, M.Ziari, W.H.Steier, "Wide-bandwidth distributed Bragg reflectors using oxide/GaAs multilayers", Electron.Lett., Vol.30, No.14, July 1994, pp.1147-1149

[90] G.M.Yang, M.H.MacDougal, P.D.Dapkus, "Ultralow threshold current vertical-cavity surface emitting lasers obtained with selective oxidation", Electron. Lett., Vol.31, No.11, pp.886-888, 1995

[91] K.L.Lear, K.D.Choquette, R.P.Scheider, S.P.Kilcoyne, K.M.Geib, "Selectively oxidised vertical cavity surface emitting lasers with 50% power conversion efficiency", Electron. Lett., Vol.31, No.3, pp.208-209, 1995

[92] G.P.Agrawal, "Nonlinear fiber optics", Springer-Verlag GmbH, 2000, p.195

[93] Analytic expression for the penetration depth taken from D.I.Babic IEEE J. of Quantum Electronics Vol.28 No.2, 1992, pp.514-524

[94] K. Ujihara, "Spontaneous Emission and the Concept of Effectice Area in a Very Short Optical Cavity with with Plane-Parallel Dielectric Mirrors", J.Appl.Phys., Jpn, Vol.30, L901, 1991

[95] M.S.Ünlü, S.Strite, "Resonant cavity enhanced photonic devices", J.Appl.Phys., Vol.78, No.2, July 1995, pp.607-639

[96] D.I.Babic et al, "Design and analysis of doubled-fused 1.55 μm vertical cavity lasers", IEEE J.Qunatum Electron., Vol.33, No.8, pp.1369-1383

[97] A.Obeidat, H.Knox, J.Khurgin, "Effects of two-photon absorption in saturable Bragg reflectors used in femtosecond solid state lasers", Optics Express, Vol.1, No.3, 1997, pp.68-73

[98] M.Sheik-Bahae, D.C.Hutchings, D.J.Hagan, E.Van Stryland, "Dispersion of bound electronic nonlinear refractive index", IEEE J.Quantum Electron., Vol.27, pp.1296-1309, 1991

[99] T.G.Ulmer, R.K.Tan, Z.Zhiping, S.E.Ralph, R.P.Kenan, C.M.Verber, A.J.Springthorpe, "Two-photon absorption-induced self-phase modulation in GaAs-AlGaAs waveguides for surface-emitted second-harmonic generation", Optics Lett., Vol.24, No.11, pp.756-758, 1999

[100] P.M.W.Skovgaard, R.J.Mullane, D.N.Nikogosyan, J.G.McInerney, "Two-photon conductivity in semiconductor waveguide autocorrelators", Optics Commun., Vol.153, 1998, pp.78-82

[101] H.Yokoyama, K.Ujihara, "Spontaneous Emission and Laser Oscillation in Microcavities", CRC Press, USA, Florida, 1995

[102] H.Folliot, M.Lynch, A.L.Bradley, T.Krug, L.A.Dunbar, J.F.Donegan, L.P.Barry, "Two-photon-induced photoconductivity enhancement in semiconductor microcavities: A theoretical investigation", J. Opt. Soc. Am. B, Vol.19, No.10, pp.2396-2402, 2002

[103] I.W.Boyd, "Two-photon IR absorption coefficient of GaAs", EMIS Datareview RN=15211, August 1989, pp.190-191

[104] L.P.Barry, B.C.Thomsen, J.M.Dudley, J.D.Harvey, "Autocorrelation and ultrafast optical thresholding at 1.5 μm using a commercial InGaAsP 1.3 μm laser diode", Electron Lett., Vol.34, No.4, pp.358-360, 1998

[105] F.R.Laughton, J.M.Marsh, D.A.Barrow, E.L.Portnoi, "The two-photon absorption semiconductor waveguide autocorrelation", IEEE J. Quantum Electron., Vol.30, No.3, pp.838-845, 1994

[106] K.Kikuchi, "Highly sensitive interferometric autocorrelator using Si avalanche photodiode as two-photon absorber", Electron. Lett, Vol.34, No.1, 1998, pp.123-125

[107] E.Hecht, "Optics", Addison-Wesley, 3rd ed., pp.111-121

[108] T.Krug, M.Lynch, A.L.Bradley, J.F.Donegan, L.P.Barry, J.S.Roberts, G.Hill, "High-sensitivity two-photon absorption microcavity autocorrelator", IEEE Photon. Technol. Lett., Vol.16 No.6, 2004, pp.1543-1545

[109] J-C.M.Diels, J.J.Fontaine, I.C.McMichael, F.Simoni, "Control and measurement of ultrashort pulse shapes (in amplitude and phase) with femtosecond accuracy", Appl.Optics, Vol.24, No.9, pp.1270-1282, 1985

[110] T.Krug, M.Lynch, A.L.Bradley, J.F.Donegan, "Two-photon absorption in microcavities for optical autocorrelation and sampling", Paper CE5-4-Thu, Technical proceedings, CLEO/Europe-EQEC Conference, Munich, Germany, 2003

[111] APE, Autocorrelator PulseScope Manual, p.9, April 2001

[112] H.K.Tsang, L.Y.Chan, J.B.D.Soole, H.P.LeBlanc, M.A.Koza, R.Bhat, "High sensitivity autocorrelation using two-photon absorption in InGaAsP waveguides", Electronic Letters, Vol.31, No.20, pp.1773-1775, 1995

[113] J.M.Roth, T.E.Murphy, C.Xu, "Ultrasensitive and high-dynamic-range two-photon absorption in a GaAs photomultiplier tube", Optics Letters, Vol.27 No.23, pp.2076-2078, 2002

[114] P.H.Lissberger, "Properties of all-dielectric interference filters. I. A new method of calculation", J.Opt.Soc.Am, Vol.49, No.2, pp.121-125, 1959

[115] G.Hernandez, "Analytical description of a Fabry-Perot spectrometer. 3. Off-axis behaviour and interference filters", Appl.Opt. Vol.13, No.11, pp.2654-2661, 1974

[116] Z.Ruikang, Z.Yuan, Z.Wei, X.Yingqiang, D.Yun, H.Yongqing, R.Xiaomin, N.Zhichuan, W.Ranghan, "Angular dependent characteristics of a 1.3 μm GaInNAs/GaAs quantum–well resonant cavity enhanced photodetector", Microwave and Otical Technol.Lett., Vol.34, No.5, September 2002, pp.333-336

[117] B.Kelly, "The asymmetric Fabry-Perot modulator, arrays and applications", Thesis, TCD, August 1996

[118] P.J.Maguire, L.P.Barry, T.Krug, M.Lynch, A.L.Bradley, J.F.Donegan, H.Folliot, "All-optical sampling utilising two-photon absorption in semiconductor microcavity", Electron. Lett., Vol.41, No.8, 2005

155

[119] M.Sheik-Bahae, A.A.Said, T.-H.Wei, D.J.Hagan, E.W.VAn Stryland, "Sensitive measurement of optical non-linearities using a single beam", IEEE J.Quantum Electron., Vol.26, pp.760-769, 1990

[120] C.H.Kwak, Y.L.Lee, S.G.Kim, "Analysis of asymmetric Z-scan measurements for large optical nonlinearities in amorphous As_2S_3 thin film", J.Opt.Soc.Am.B, Vol.16, No.4, April 1999, pp.600-604

[121] H.Folliot, M.Lynch, A.L.Bradley, J.Hegarty, J.F.Donegan, L.P.Barry, J.S.Roberts, G.Hill, "Two-photon absorption photocurrent enhancement in bulk AlGaAs semiconductor microcavities", Appl. Phys. Lett., Vol.80, No.9, pp.1328-1330, 2002

[122] G.P.Agrawal, "Nonlinear fiber optics", Academic Press, 3rd ed., 1995

[123] Frequency Resolved Optical Gating (FROG) set-up based on SHG at Dublin City University

[124] R.Trebino, "Frequency-resolved optical gating: The measurement of ultra-short laser pulses", Kluwer Academic Publishers, Boston, 2002

[125] D.T.Reid, B.C.Thomsen, J.M.Dudley, J.D.Harvey, "Sonogram characterisation of picosecond pulses at 1.5 μm using waveguide two photon absorption", Electron.Lett., Vol.36, No.13, June 2000, pp.1141-1442

[126] P.Meystre, "Velocity-dependent spontaneous emission: The strong coupling regime", Optics Communications, Vol.90, No.1-3, June 1992, pp.41-45

[127] F.Jahnke, M.Kira, S.W.Koch, O.Lyngnes, J.D.Berger, H.M.Gibbs, G.Khitrova, "Excitonic nonlinearities in semiconductor microcavities", Conference on Quantum Electronics and Laser Science (QELS)–Technical Digest Series, Vol.12, 1997, pp.10-11

[128] V.Savona, "Linear Optical Properties of Semiconductor Microcavities with Embedded Quantum Wells", Confined Photon Systems, Springer

[129] C.J.Hood, M.S.Chapman, T.W.Lynn, H.J.Kimble, "Real-Time Cavity QED with Single Atoms", Phys. Rev. Lett. 80, 1998, pp.41574160